DOCTORAL THESIS IN PHYSICS
ICFO BARCELONA 2014

Plasmon, light, and electron beam interactions at the nanoscale

---

ANA ASENJO GARCÍA

Advisor: Javier García de Abajo

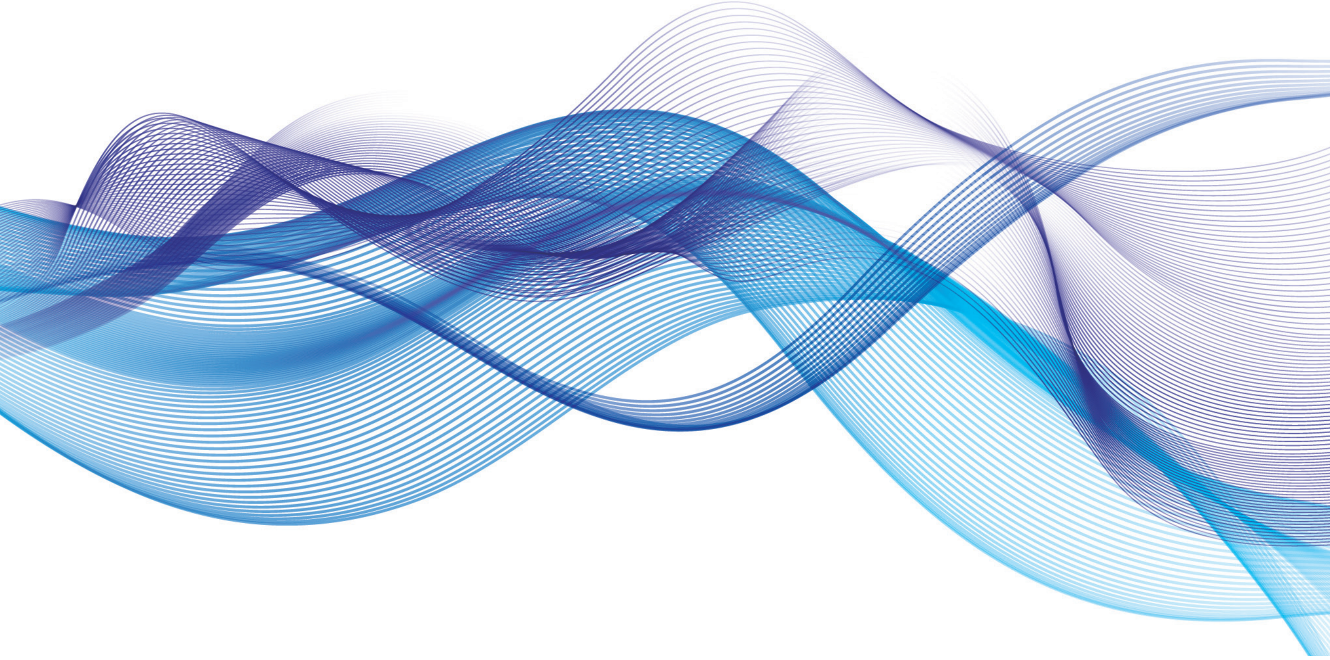

Universidad Complutense de Madrid
Facultad de Física
Departamento de Óptica

Plasmon, Light, and Electron Beam Interactions at the Nanoscale

Doctoral Thesis

Dissertation submitted by
ANA ASENJO GARCÍA
for the degree of Doctor of Philosophy

Supervisor: Prof. Francisco Javier García de Abajo

ICFO - The Institute of Photonic Sciences

Barcelona, June 2014

Universidad Complutense de Madrid
Facultad de Física
Departamento de Óptica

Interacción de plasmones, luz y haces de electrones en la nanoescala

Tesis Doctoral

Memoria presentada por
ANA ASENJO GARCÍA
para optar al grado de Doctor

Director: Prof. Francisco Javier García de Abajo

ICFO - Instituto de Ciencias Fotónicas

Barcelona, Junio de 2014

Esta tesis doctoral se ha realizado en el grupo de Nanofotónica en las siguientes instituciones:

- ICFO - Instituto de Ciencias Fotónicas (2013-2014),
- CSIC - Instituto de Química-Física "Rocasolano" (2011-2013),
- CSIC - Instituto de Óptica "Daza de Valdés" (2010-2011),

gracias a la financiación de una beca predoctoral del programa FPU del Ministerio de Educación (Ref. AP2009-1760).

A mi hermana y mi abuela

A Héctor, Mishi y Yuki

That which I am writing about so tediously,
may be obvious to someone whose mind is less decrepit.

Ludwig Wittgenstein

Acknowledgments

Luckily, during these years I have not been alone, neither in my personal nor my professional life. There is no doubt that without the people that have walked with me on this long (and sometimes winding) road, this thesis would not have been brought to life. I would like to thank all of you in this seemingly tiny in length – but wide in gratefulness – piece of paper.

En primer lugar, he de agradecer a Javier todo el tiempo que ha invertido en mí. Esta tesis no merecería tal nombre sin su esfuerzo y compromiso durante todos estos años. Gracias a su talento y a su amplio rango de intereses he podido trabajar en temas muy diversos, algo que he apreciado muchísimo. Su pasión por la física y su dedicación al trabajo me servirán de inspiración allá donde vaya. Con su ejemplo, él me ha demostrado que afrontar los problemas con optimismo es siempre la mejor opción, tanto en la física como en la vida.

During my time as a student, I had the opportunity to learn from many people. I would like to express my gratitude to all my collaborators. In particular, I am especially grateful to Prof. Laura Na Liu and her group, whose beautiful experiments (also performed by the group of Prof. Baoquan Ding) greatly improve this thesis. It was a real pleasure to work with her, and our discussions helped me understand much better my own work. I would further like to thank Prof. Harald Giessen for hosting me in my visit to Stuttgart. I also greatly benefited from the visit of Prof. Alexander Govorov to ICFO, where he generously spent much time with me discussing several problems. Moreover, I want to thank Prof. Jo Verbeeck and Giulio Guzzinati for inspiring talks about vortex electron beams.

A lo largo de estos años he tenido el placer de trabajar codo con codo con los miembros del grupo de nanofotónica: Alejandro, Xesús, Christin, Viktor, Suko, Johan, Iván, Jose, Joel y Juanma. Además de ser una fuente de diversión, también lo han sido de conocimiento. En concreto, no puedo pasar por alto la gran ayuda que Alejandro me prestó durante mis primeros años, y le doy las gracias por ello. Agradezco también a Jose la lectura crítica de esta tesis. Along these years, we had many visitors in our group and, among them, there was Stéphane-Olivier, which has since then become a friend, and also helped me proofreading this manuscript.

No puedo dejar en el olvido todos los buenos momentos que he pasado con la gente que me ha acompañado en el CSIC, como Emilio, Marco, Marien, Susana y Luis. Así mismo, en mi último año en Castelldefels he estado muy bien acompañada ya que el grupo de Optical Tweezers me adoptó como una más. Muchas gracias a Iñaki, Mónica, Raúl, Pau y Antonio. También en los primeros tiempos aquí pude disfrutar de la presencia de Marta y, aunque ya en Stanford, agradezco a Alberto todas las discusiones que hemos tenido sobre quiralidad a lo largo de estos años. Cuando llegué a ICFO, Riccardo ya estaba en Londres, pero agradezco mucho sus consejos tanto para la vida científica como para el diseño de las figuras de los artículos. It was also a pleasure to attend the meetings of Darrick's group, which I have sincerely enjoyed and from which I have learned a lot. Fuera de ICFO mi vida ha sido mucho mejor al tener la suerte de que Ester sea mi vecina. En ella he encontrado una (buena) amiga y (no tan buena) compañera de gimnasio: gracias por preocuparte tanto por mí (y por Petri).

A lo largo de mi vida, ha habido muchos profesores que han influido en mí. Los primeros fueron Mariano, Lourdes y Carmen. En la universidad, tuve la suerte de encontrar a Luis Garay, a pesar del sufrimiento que eso conlleva. También quisiera dar las gracias a Tatiana Alieva por el tiempo que me dedicó y por ser quien me introdujo en la óptica y en el mundo de la investigación.

A pesar de que quizás la sección de agradecimientos de una tesis doctoral no sea la mejor ocasión para agradecer a mis amigos su amistad, al menos me da la oportunidad de hacerlo. Muchas gracias Usue e Irene, por aguantarme desde tiempos inmemoriales. Gracias también a Marta, Paloma, María y Ángela. I would also like to thank Sohee and Sojin, for being able to maintain a friendship 10.000 km away. Por supuesto, no puedo olvidar a mi *álter ego* coreano Yu Kyoung: qué te voy a decir que no sepas ya.

Finalmente, quiero agradecer a mi familia su apoyo: a mi abuela y a mi tía, por tantos domingos en los que me han alimentado y he disfrutado con ellas; a mis tíos Miguel y Luisa, por ayudarme cuando llegué a Madrid y en todos los años posteriores; a mis padres, porque me dejaron ir y elegir mi camino, aunque la situación no era la mejor, y por ser un ejemplo de trabajo y honradez; a mi hermana, por aguantarme cuando he sido egoísta. No entiendo cómo puedes estar más orgullosa de mí que de ti misma.

Gracias Héctor, por cuidar de Yuki y Mishi mejor que yo, y por todo lo que me has hecho reír.

Sin duda, mirando atrás, veo que he sido muy afortunada.

Contents

List of Figures v

List of Acronyms vii

Abstract 1

Resumen 7

1 Introduction 13
- 1.1 Classical electrodynamics 14
- 1.2 Chirality and circular dichroism 16
- 1.3 Electromagnetic fields in metals 19
- 1.4 Electron beam interactions with metals 25
  - 1.4.1 Electron beams and light fields 30

2 Stimulated light emission and scattering by rotating particles 33
- 2.1 Introduction 34
- 2.2 Physical model and dynamical properties 35
- 2.3 Connection to actual particles 43
- 2.4 Stimulated emission and light amplification 44
- 2.5 Particle heating and acceleration time 45
- 2.6 Conclusions 48

3 Chiral interactions between light and matter 51
- 3.1 Introduction 52
- 3.2 Experimental methods 53
- 3.3 Theory and modeling 55
  - 3.3.1 Dipole-dipole interaction 55
  - 3.3.2 Multiple scattering multipolar calculation 58
- 3.4 Agreement between experimental and theoretical results 59
- 3.5 The role of plasmonic coupling 61
- 3.6 Other systems 63

3.7 Conclusions 64

4 Chiral interactions between electron vortex beams and matter **67**
4.1 Introduction 68
4.2 Generalized expression for the transition probability 69
4.3 Chiral plasmonic cluster 71
4.3.1 Transition from a plane wave to a vortex 73
4.3.2 Transition from a gaussian beam to a vortex 84
4.4 Chiral molecule 86
4.5 Conclusions 90

5 Electron energy-gain spectroscopy **91**
5.1 Introduction 92
5.2 Outline of the theory 93
5.3 Energy-gain spectroscopy 96
5.4 Unified analytical quantum model for EELS, EEGS, and CL 102
5.5 Conclusions 106

Conclusions **109**

Appendices

A Optical torques and forces acting on a small particle **115**

B Polarizability tensor and light extinction cross-section of a chiral molecule **121**

C Electromagnetic Green tensors of clusters and chiral molecules **127**

D Derivation of EELS, EEGS, and CL probabilities **131**

List of publications and contributions to conferences **137**

Bibliography **141**

List of Figures

1.1 Sketch of the optical properties of a chiral structure. 18
1.2 Dispersion relation of a surface plasmon. 22
1.3 Comparison between the extinction cross-section and EELS probability. 29
1.4 Sketch of electron energy loss and gain spectra. 31

2.1 Illuminated rod-like particle rotating around a transversal direction . . 36
2.2 Dynamical properties of a rotating rod illuminated by LCP light 39
2.3 Dynamical properties of a rotating rod for linearly polarized light . . . 42
2.4 Stimulated light emission in rotating particles. 45
2.5 Temperature of a gold sphere and a carbon nanotube as a function of the incident light intensity. 46
2.6 Time needed to accelerate a gold sphere and a carbon nanotube to a rotational velocity $\Omega = 1\,\mathrm{MHz}$ as a function of the light intensity 47

3.1 Schematic illustration of the DNA origami experiment. 54
3.2 Agarose gel image and TEM images of the structures. 56
3.3 Theoretical LCP light extinction cross-section and CD spectra for the left-handed structure. Measured extinction for the clusters. 59
3.4 Measured and calculated CD spectra. 60
3.5 Influence of the size and separation on the CD spectra. 62
3.6 Influence of the incidence direction on the CD. 63

4.1 Multipolar vs dipolar response of a cluster 71
4.2 Sketch of the proposed setup. Energy-loss cross-section spectra. 74
4.3 Dichroism in the spectrally resolved inelastic cross-section. Extrinsic dichroism displayed by the trimer. Normalized dichroism for different electron energies. 77
4.4 Influence of different parameters on the dichroism. 79
4.5 Retarded and non-retarded dichroism. Non-retarded torque. 83
4.6 Dichroism for a focused electron beam. 85

4.7 Universal curves for the partial inelastic cross-section and dichroism of a model point structure characterized by a chiral excitation. 87
4.8 Partial inelastic cross-section and normalized dichroism for an α-helix. 89

5.1 Extinction cross-section and induced electric field intensity of a nanoshell. 97
5.2 Occupation probability of different multiphoton exchange channels. . . 99
5.3 Probability of multiphoton emission and absorption as a function of both the incoming light wavelength and net number of exchanged photons 100
5.4 Electron energy loss and gain spectra for an electron passing close to a silver nanoshell. 101
5.5 Diagrams for all processes involving the creation of one plasmon, up to second order. 105

List of Acronyms

CD	Circular dichroism
CL	Cathodoluminescence
CP	Circularly polarized
EEGS	Electron energy-gain spectroscopy
EELS	Electron energy-loss spectroscopy
FWHM	Full width at half maximum
IR	Infrared
LCP	Left circularly polarized
LSP	Localized surface plasmon
MESME	Multipole elastic scattering of multiple expansions
OAM	Orbital angular momentum
RCP	Right circularly polarized
SPP	Surface plasmon polariton
TEM	Transmission electron microscope
UV	Ultraviolet
3D	Three-dimensional

Abstract

With the exception of gravitational forces, the interaction between light and matter is responsible for almost all physical phenomena that we routinely experience. Electromagnetic fields permeate all our surroundings, and give rise to far-reaching events that range from the cosmic radiation of the early universe to vacuum forces suffered by atoms. In fact, the mysteries of these interactions have fascinated humankind since ancient times, and there is no doubt that light has played a fundamental role in most of the greatest milestones in the history of science, ranging from the invention of both the microscope and the telescope to the theory of relativity. Remarkably, light does not only enable us to actually *see* the world, but also to manipulate it. Electromagnetic fields carry energy and information, and thanks to their control, we are able to perform tasks that are now considered to be mundane, such as browsing the web using a computer powered by a solar cell.

As Richard Feynman pointed out in his acclaimed talk *There is plenty of room at the bottom*, the manipulation of the interplay between light and matter at small scales opens up doors to many exotic phenomena. These interactions vary strongly depending on the characteristic dimensions of matter. Actually, many intriguing behaviors are unveiled when the light wavelength matches the size of a given object. Since the wavelength of visible light is $\sim 400 - 700$ nm, our interest is primarily focused on the study of nanostructured materials. The considerable improvement of fabrication techniques over the last decades has made possible to achieve an impressive degree of miniaturization, resulting in a plethora of nanoparticles that exhibit optical properties that differ strongly from those found in bulk media. Among the many materials that have been considered for controlling and engineering light fields at the nanoscale, metals play a major role. The collective oscillations of their conduction electrons, the so-called plasmonic excitations, are of paramount importance in the field of nanophotonics. Essentially, metallic particles confine light to tiny spaces and produce intense field enhancement. Besides its fundamental interest, plasmonics has strikingly diverse implications in technology. It finds applications in areas such as photovoltaics, biomolecular sensing, and medicine.

The present thesis is devoted to the study of the interactions between plasmon-supporting metallic nanostructures, light, and electron beams.

As well as energy and information, light fields also carry linear and angular momenta. They are thus able to exert forces and torques upon objects. In particular, it has been demonstrated that circularly polarized light – which carries spin angular momentum – can be employed to rotate both macroscopic and nanoscopic bodies. This raises fundamental questions such as how the physical properties of a particle are modified when subject to extreme rotation velocities, or whether it is possible to cool down the rotational degrees of freedom of a microparticle in a cavity.

The first part of this thesis is concentrated on the analysis of the optical response of metallic nanoparticles that are rotating in vacuum and exposed to external illumination. To that purpose, we develop a simple theory inspired in the Drude-Lorentz model, in which we describe a rod-like particle as a harmonic oscillator, with a driving force due to an external circularly-polarized light field, and a damping term that accounts for intrinsic losses. Moreover, Abraham-Lorentz force is also included, in order to allow for radiative damping. From the equation of motion, one is able to derive analytical expressions for the mechanical torque that light exerts on the particle, the absorbed power, and the scattering cross-sections. Interestingly, a rotational Doppler shift arises in the scattered light: the particle produces inelastic scattering at frequencies separated from that of the incoming light by twice the rotation frequency. Actually, this same phenomenon has been observed in rotational Raman scattering, and has also been proposed as an accurate method to estimate the rotational velocities of spinning objects. The parameters of the proposed toy-model can be straightforwardly connected to those of actual particles, such as metallic rods or spheres, through the expression for the dipolar polarizability. Remarkably, due to the inclusion of radiation damping, the resulting polarizability is radiatively correct and, therefore, our description is valid for absorbing as well as non-absorbing nanoparticles.

We further show that the system becomes superradiant under certain conditions. Specifically, if the particle's rotational frequency is higher than that of the external field, and both the light polarization vector and the nanostructure rotate in the same direction, the incoming light is amplified. Although the phenomenon of stimulated emission is customarily treated within a quantum framework, we here demonstrate that it arises as well in this classical system. This superradiance is due to a conversion of the rotational energy into radiation, accompanied by a subsequent decrease of the rotational speed, as is shown by a detailed analysis of the expressions for the mechanical and extinction cross-sections, which become negative.

With the aim of demonstrating the experimental feasibility of achieving high rotational frequencies, we calculate the necessary field intensities required for spinning several kinds of nanoparticles by means of circularly polarized light. Besides, we also compute the equilibrium temperature reached by these structures upon illumination. In particular, the theoretical predictions for small gold spheres and single-walled carbon nanotubes are quite optimistic: the particles reach an equilibrium temperature below that of melting for light intensities that cause them to reach a significantly high spinning rate in a very short time.

As happens with rotating particles, the interaction of circularly polarized light with chiral matter is also non-symmetrical: the absorption and scattering rates of light are slightly different depending on the handedness of the structure. The lack of mirror symmetry, known as chirality, is a pervasive feature of biological molecules, such as proteins, glucids, and nucleic acids. As a matter of fact, it is imperative to determine whether chiral pharmacological compounds are left- or right-handed since their behaviors might be entirely different due to the interaction with these biomolecules. Despite the relevance of adequately sorting different enantiomers according to their chiral nature, this is not an easy job, as they behave identically under structural spectroscopic techniques. Luckily, this property can be revealed by employing circularly polarized light but, nevertheless, produces a very faint effect.

In recent years, there has been a great interest on chiral plasmonic nanostructures. Due to plasmonic coupling, chiral effects might be very much enhanced in comparison to those of biological molecules. In the second part of this work we investigate plasmonic chiral tetramers, which break mirror symmetry due to the spatial arrangement of their components. Despite the theoretical character of this thesis, the study of these structures has been developed in close collaboration with the experimental groups of Prof. Laura Na Liu and Prof. Baoquan Ding, with the aim of providing some insight into their measurements. In particular, we calculate the circular dichroism (this is, the difference between the absorption of left- and right-circularly polarized light) generated by these structures and compare our calculations with experimental results. The clusters are composed of four gold nanospheres that are functionalized with DNA strands and assembled employing a rigid DNA origami template to provide stability. They are synthesized in a water-based solution and they are thus randomly oriented. The DNA-based fabrication method constitutes a novel bottom-up approach for the generation of nanostructures, with several advantages with respect to more traditional top-down techniques such as lithography. It is, in fact, a mass-production method of chiral clusters with nanometer accuracy due to the site-specific binding of nucleic acids.

In order to compute the light absorption cross-section of the structures, we employ two different procedures. First, we model the spheres as point dipoles with a frequency-dependent polarizability and study their optical response in a self-consistent and semi-analytical manner. We then compare this tutorial approach with a completely numerical calculation that includes their full multipolar responses. This latter method is more accurate and is, therefore, subsequently applied to interpret the experimental results. We take into account the random orientation of the clusters by performing an average over light incidence directions. The agreement between the experimental and numerical results is very satisfactory. There are, however, some minor discrepancies in the magnitude of the signal. The primary reason for this small disparity is the experimental uncertainty about the clusters' concentration in the solution. Besides, it can also be due to the high sensitivity of the dichroism to slight variations on the sphere diameters and separations, which can be reasonably expected to arise in the experiment, but are not incorporated into the simulations. The dichroism spectra show a characteristic pattern, whose sign is reversed for the clusters of opposite handedness. As a control experiment, a trimer is also synthesized and, as expected, displays null dichroism due to the lack of chirality. In fact, four is the minimum number of achiral particles needed to constitute a chiral cluster. To further analyze the role of plasmonic coupling, we demonstrate that the dichroism reduces considerably when the spheres' diameters decrease or the separation between them increases, since the near-field interaction is critical to the chiral response.

One legitimate question is whether chiral matter displays dichroism when interacting with light that carries orbital angular momentum. As opposed to spin, associated with the polarization, orbital angular momentum is related to the spatial structure of light fields, which possess an azimuthal phase dependence and a helical wavefront. This problem has received much interest recently and it has been demonstrated, both theoretically and experimentally, that although optical vortex beams exert forces and torques on matter, they do not engage in dichroic activity. The third part of the present work deals in fact with this issue but from a different and novel point of view. Instead of using light, we propose to employ vortex electron beams, and study the energy lost by these electrons upon interaction with chiral matter.

The invention of electron microscopes in the thirties was a scientific breakthrough. Suddenly, structures of tiny proportions, which were not resolved by optical microscopes, could be observed. Surprisingly, plasmons were first revealed in an experiment involving electron bombardment of a metallic film. Since then, electron beams have been extensively used to probe the optical properties of metallic nanostructures, employing the well-known technique of electron energy-loss spectroscopy. Vortex electron beams were experimentally generated in an electron microscope only a few years ago, and they are characterized by a helical wave-function. Specifically, we define a new kind of dichroism that can be computed as the difference in the energy loss suffered by different orbital angular components of the electron upon inelastic interaction with a chiral structure. In particular, we analyze two different samples: a silver tetramer and a biomolecule.

The silver cluster consists of nanospheres described in the dipolar approximation, which interact with each other in vacuum. One can describe the full electromagnetic response of the whole cluster via its Green tensor. We predict a large dichroism that can reach up to ten percent of the loss signal. This remarkably large value is principally due to the relatively low losses of silver. We calculate the energy loss for two different incoming electron wave-functions, a plane-wave and a focused beam. The latter would be useful to resolve chiral modes with sub-nanometer accuracy, something that is not possible with light. Moreover, electron beams would also be able to excite dark modes, which are plasmonic modes that cannot be accessed by optical means.

In the non-retarded limit, when the speed of light is considered to be infinite and the interactions are instantaneous, it is possible to decompose the total energy loss and dichroism as a sum of the contributions of the plasmonic eigenmodes of the cluster. Within this formalism, we predict that all of them generate a dichroic signal which gives rise to the complex response displayed by the structure. Moreover, one is able to calculate the forces and torques exerted upon the cluster by each of the different angular momentum components of the vortex beam. As expected, the conservation of linear and angular momenta is confirmed.

Although there has been a remarkable interest in chiral plasmonic nanostructures in the recent years, the main goal of circular dichroism spectroscopy is to be able to determine the handedness of a single molecule. To that purpose, we study the interaction between electron vortex beams and point-like molecules, which are described by non-orthogonal electric and magnetic dipoles – a configuration that breaks mirror symmetry. We derive a universal scaling law for the dichroism exhibited by any kind of structure that can be characterized by finite crossed electric and magnetic polarizabilities. Moreover, we also focus on a specific biomolecule: the α-helix, a common secondary structure of proteins. The interaction between electron vortex beams and biomolecules opens up the door to chemical and pharmaceutical applications.

One of the great advantages of using electrons as a probing source is their high spatial accuracy, due to their short de Broglie wavelength. Nowadays, electron microscopes reach sub-angstrom resolution, whereas optical microscopes are diffraction limited and, in the best-case scenario, are able to resolve around ten nanometers. Nevertheless, the energy resolution of electron microscopes is far from that achieved with optical tools. This is mainly due to the broad spectral width of electron beams and the limited resolution of the spectrometer. Currently, one of the main objectives of the electron microscopy community is to improve this seemingly low energy resolution. This is by no means a simple task, and many options, such as the use of monochromators, have been explored although the elusive energy resolution of light-based microscopes is still not within reach.

In this context, the final section of the thesis is devoted to proposing a new spectroscopy technique that combines the great spatial accuracy of electrons with the high energy resolution of light. This method is based upon the analysis of the energy gains and stimulated losses that the electron experiences when interacting with an illuminated nanostructure. Due to the evanescent nature of the surface modes of a metallic particle, the electron is able to emit or absorb photons, a physical process that is forbidden in free space due to energy-momentum conservation. Electron energy losses and gains have been already observed in a pioneering experiment a few years ago, in which an electron beam was sent in coincidence with a light pulse to the vicinity of two distinct samples: a silver wire, and a carbon nanotube. However, although it constituted a remarkable proof-of-principle, the experimental results did not provide any information about the optical response of the probed nanostructures.

Hence, we suggest that the spectral response of the sample can be observed by varying the frequency of the incoming light. In particular, we study metallic nanoshells consisting of a silica core and a gold or silver coating, which display sharp resonant features in the near infrared. We calculate the probability of energy gains and losses as a function of the incoming light frequency and intensity, for both pulsed and continuous-wave illumination. As the frequency of the light starts to match that of the plasmonic resonance, the elastic component of the electron wave-function begins to depopulate and the amplitude of the inelastic channels increase. For low intensities, this depopulation reaches a maximum at the near-field resonance frequency. Interestingly, the extinction cross-section resonant peak is blue-shifted a few nanometers with respect to the maximum depletion of the elastic electron component. This is a manifestation of the fact that the coupling between photons and electrons is mediated by the near-field, which is dominated by the surface modes. On the other hand, for higher intensities, a non-trivial interplay between different multiphoton channels takes over and gives rise to oscillations in the electron probability.

Remarkably, we predict substantial energy gains and losses for light intensities below the melting threshold of the particles, even under continuous-wave illumination. Due to the less lossy character of silver compared to gold nanoshells, the field enhancement produced by these nanostructures is higher, leading to the generation of multiphoton events at lower intensities. This allows one to speculate with the feasibility of experimental confirmations of our predictions in the near future. Finally, in order to place the energy gain probabilities into perspective, we compare them with those of more traditional spectroscopic techniques, such as energy-loss or cathodoluminescence (in which the plasmons created by the electron decay radiatively, generating light). To that purpose, we develop a unified analytical quantum model valid at low light intensities. This perturbative approach treats the aforementioned spectroscopies on equal footing and provides further insight about the fundamental processes on which they rely.

Resumen

Salvo por la fuerza gravitatoria, la interacción entre luz y materia es responsable de la mayoría de los fenómenos físicos que experimentamos cotidianamente. Los campos electromagnéticos nos rodean, dando lugar a un amplio abanico de efectos que van desde la radiación cósmica del universo primitivo a las fuerzas de vacío que perciben los átomos. Los misterios de estas interacciones han fascinado a la humanidad desde la antigüedad, y no hay duda de que la luz ha jugado un papel fundamental en la mayoría de los grandes hitos de la historia de la ciencia, desde la invención del microscopio a la teoría de la relatividad. La luz no sólo nos permite *ver* el mundo, sino también manipularlo. Los campos electromagnéticos transportan energía e información, y gracias a su control somos capaces de realizar complejas tareas ahora consideradas mundanas, como navegar por la web desde un ordenador cuya energía es suministrada por una placa solar.

Tal y como Richard Feynman señaló en su famosa charla *Hay mucho espacio al fondo*,[1] la manipulación de las interacciones entre luz y materia a pequeña escala abre las puertas a un nuevo mundo. De hecho, éstas varían dramáticamente en función de las dimensiones características de la materia y los campos electromagnéticos, y producen fenómenos exóticos cuando ambas coinciden. Dado que la longitud de onda de la luz visible es $\sim 400 - 700$ nanómetros, son los materiales nanostructurados los que capturan nuestro interés. Debido a la considerable mejora de las técnicas de fabricación en las últimas décadas, se ha logrado un impresionante grado de miniaturización. Esto ha dado lugar a la generación de una plétora de nanoestructuras que exhiben propiedades ópticas que difieren ostensiblemente de las que se encuentran en los materiales a grandes escalas. Entre los muchos medios que se han estudiado con el fin de controlar los campos de luz en la nanoescala, los metales juegan un papel fundamental. Las oscilaciones colectivas de sus electrones de conducción, llamadas excitaciones plasmónicas, son de vital importancia en el campo de la nanofotónica. En esencia, las nanopartículas metálicas son capaces de confinar la luz en espacios extraordinariamente pequeños y de incrementar la intensidad del campo incidente. Además de su interés para la ciencia básica, la plasmónica tiene un

---

[1] El título original es *There is plenty of room at the bottom*.

gran potencial tecnológico, con múltiples aplicaciones en áreas tan diversas como la energía fotovoltaica, la medicina o la detección molecular.

Esta tesis está dedicada al estudio de las interacciones entre nanoestructuras plasmónicas, luz y haces de electrones.

Además de energía e información, los campos electromagnéticos también poseen momento lineal y angular. Por tanto, son capaces de ejercer fuerzas y torques. En concreto, se ha demostrado que la luz circularmente polarizada – que tiene momento angular de espín – puede ser empleada para rotar estructuras tanto macroscópicas como nanoscópicas. Este hecho plantea cuestiones fundamentales tales como la modificación de las propiedades físicas de una partícula cuando está sometida a velocidades de rotación extremas, o la posibilidad de enfriar los grados de libertad de rotación de una micropartícula en una cavidad.

La primera parte de esta tesis se centra en el estudio de la respuesta óptica de nanopartículas metálicas que giran en el vacío expuestas a iluminación externa. Desarrollamos una teoría sencilla inspirada en el modelo de Drude-Lorentz, en la que se describe una partícula alargada como un oscilador armónico forzado por un campo de luz circularmente polarizada y con un término de amortiguamiento que representa las pérdidas intrínsecas. Por otra parte, también se incluye la fuerza de Abraham-Lorentz, con el fin de tener en cuenta la amortiguación debida a la radiación. A partir de la ecuación de movimiento, derivamos expresiones analíticas para el torque mecánico ejercido por la luz sobre la partícula, la potencia absorbida y las secciones eficaces de esparcimiento (*scattering*). Analizamos la aparición de un desplazamiento Doppler rotacional en la frecuencia de la luz dispersada. En la literatura, este fenómeno es conocido en el contexto de la espectroscopía Raman rotacional. Así mismo, también se ha propuesto como un método preciso para estimar velocidades de giro. Los parámetros de nuestro modelo pueden relacionarse fácilmente con los empleados para caracterizar partículas metálicas reales, tales como cilindros alargados o esferas, a través de la expresión para la polarizabilidad dipolar. Cabe destacar la validez de nuestra descripción para tratar nanoparticulas tanto absorbentes como no absorbentes, gracias a la inclusión de la amortiguación por radiación.

Sorprendentemente, el campo externo se amplifica cuando la frecuencia rotacional es mayor que la de éste, y el vector de polarización de la luz y la nanoestructura giran en la misma dirección. A pesar de que el fenómeno de la emisión estimulada es tratado habitualmente dentro de un marco cuántico, emerge también en este sistema clásico. Esta superradiancia se debe a la conversión de la energía de rotación en radiación, y está acompañada de una disminución de la velocidad rotacional, como se desprende de un análisis detallado de las expresiones para las secciones eficaces mecánica y de extinción, que son negativas.

Con el objetivo de demostrar la viabilidad experimental de alcanzar altas frecuencias de giro, calculamos la intensidad de luz necesaria para rotar distintos tipos de nanopartículas mediante luz circularmente polarizada. Además, también analizamos la temperatura de equilibrio alcanzada por estas estructuras debido a la absorción de dicha radiación. Las predicciones teóricas para pequeñas esferas de oro y nanotubos de carbono son optimistas: para intensidades de luz asociadas a altas aceleraciones, las partículas alcanzan una temperatura inferior a la de fusión del material.

Como sucede en el caso de partículas en rotación, la interacción de la luz circularmente polarizada con materia quiral también es asimétrica: las tasas de absorción y esparcimiento de luz son ligeramente diferentes dependiendo de la quiralidad de la estructura. La falta de simetría especular, también llamada quiralidad, es una característica muy común en las moléculas biológicas. Es extremadamente importante clasificar adecuadamente los diferentes enantiómeros según su naturaleza quiral. Sin embargo, ésta no es tarea fácil puesto que se comportan de forma idéntica al ser estudiados con técnicas estructurales. Afortunadamente, esta propiedad se revela en experimentos con luz circularmente polarizada, a pesar de que típicamente produce un efecto muy débil en la medida.

En los últimos años se ha despertado un gran interés por las nanoestructuras metálicas quirales. Debido al acoplamiento plasmónico, los efectos quirales pueden ser considerables en comparación con los observados en moléculas biológicas. La segunda parte de este manuscrito está dedicada a la investigación de tetrámeros quirales plasmónicos, que rompen la simetría especular debido a la disposición espacial de sus componentes. Específicamente, calculamos el dicroísmo circular (esto es, la diferencia entre la absorción de luz circularmente polarizada a izquierdas y a derechas) producido por estas estructuras y comparamos nuestras predicciones con resultados experimentales. [1] En concreto, los tetrámeros están formados por cuatro nanoesferas de oro funcionalizadas con hebras de ADN y ensambladas mediante una lámina rígida de origami de ADN para proporcionar estabilidad. Estas moléculas plasmónicas se sintetizan en una disolución de base acuosa y están por tanto orientadas al azar. La técnica de fabricación basada en el ADN constituye un nuevo enfoque para la generación ascendente (*bottom-up*) de nanoestructuras, con varias ventajas con respecto a los enfoques descendentes (*top-down*) más tradicionales, como la litografía. De hecho, es una técnica de producción en masa de partículas quirales con una precisión nanométrica debido a la especificidad de los ácidos nucleicos.

Para el cálculo de la absorción de luz por parte de las estructuras empleamos dos métodos diferentes. En primer lugar, modelamos las esferas como dipolos puntuales con una polarizabilidad dependiente de la frecuencia y analizamos su respuesta óptica de una manera autoconsistente y semianalítica. A continuación, comparamos

---

[1] A pesar del carácter inminentemente teórico de esta tesis, el estudio de estas estructuras se ha desarrollado en colaboración con los grupos experimentales de los Prof. Laura Na Liu y Baoquan Ding.

este enfoque de carácter más tutorial con un cálculo completamente numérico que tiene en cuenta la respuesta multipolar. Este último método es más preciso y es el empleado posteriormente para analizar los resultados experimentales. En ambos casos, a fin de tener en cuenta la orientación aleatoria de las partículas, realizamos un promedio sobre las direcciones de incidencia de la luz. Los espectros de dicroísmo muestran una señal característica, cuyo signo se invierte para las estructuras de quiralidad opuesta. La concordancia entre los resultados experimentales y numéricos es muy satisfactoria, aún habiendo, sin embargo, algunas discrepancias menores en la magnitud de la señal. La razón principal de esta pequeña disparidad es la incertidumbre experimental acerca de la concentración de partículas en la disolución. También puede ser debida a la alta sensibilidad del dicroísmo a ligeras variaciones en los tamaños y separaciones de las esferas, que no se tienen en cuenta en las simulaciones. Como experimento de control, se sintetiza también un trímero, que muestra nulo dicroísmo debido a la falta de quiralidad. De hecho, cuatro es el número mínimo de partículas aquirales necesarias para constituir un grupo quiral. Con el objetivo de analizar el papel del acoplamiento plasmónico, demostramos que el dicroísmo disminuye considerablemente cuando los diámetros de las esferas se reducen o la separación entre ellas aumenta, ya que la interacción debida al campo cercano (*near-field*) es fundamental para la respuesta quiral.

Cabe preguntarse si una estructura quiral muestra dicroísmo al interactuar con luz que posee momento angular orbital. A diferencia del intrínseco, asociado a la polarización, el momento angular orbital está relacionado con la estructura espacial de los haces de luz. Dichos haces poseen una fase con una dependencia acimutal, que se traduce en un frente de onda helicoidal. Esta cuestión ha suscitado un notable interés recientemente y se ha demostrado, tanto teórica como experimentalmente, que a pesar de que los vórtices ópticos ejercen fuerzas y torques sobre la materia, no involucran actividad dicroica. La tercera parte de este manuscrito trata sobre este tema, pero desde un punto de vista diferente y novedoso: en lugar de utilizar luz, proponemos emplear vórtices de electrones y estudiar la energía perdida por estos en la interacción con materia quiral.

La invención de los microscopios electrónicos en los años treinta del pasado siglo supuso un gran avance científico. De pronto, estructuras diminutas que no podían observarse con microscopios ópticos pudieron ser estudiadas. De hecho, los plasmones fueron detectados por primera vez en un experimento en el que se lanzaban electrones hacia una película metálica. Desde entonces, estas partículas cargadas se han empleado intensivamente para investigar las propiedades ópticas de nanoestructuras metálicas, mediante la técnica de espectroscopia de pérdida de energía (*EELS*, de sus siglas en inglés). Por otro lado, los vórtices de electrones –caracterizados por una función de onda helicoidal– se generaron experimentalmente hace tan sólo unos pocos años.

En esta tesis definimos un nuevo tipo de dicroísmo que se puede calcular como la diferencia de las pérdidas de energía que sufren las diferentes componentes de momento orbital angular tras la interacción inelástica con una muestra quiral. En particular, estudiamos dos muestras diferentes: un tetrámero de plata y una molécula biológica. La estructura de plata está formada por nanoesferas descritas en la aproximación dipolar y que interactúan entre ellas en el vacío. Describimos la respuesta electromagnética del conjunto a través de su tensor de Green. Predecimos un alto dicroísmo, que puede alcanzar hasta el diez por ciento de la señal de pérdida. Este valor es tan prominente debido, principalmente, a la alta conductividad de la plata. Calculamos la pérdida de energía para dos tipos distintos de funciones de onda incidentes: un haz extenso y otro enfocado. Este último es útil para analizar modos quirales con una precisión sub-nanométrica, algo que no es posible con luz. Por otra parte, los electrones también son capaces de excitar modos oscuros (oscilaciones plasmónicas que no pueden ser excitadas por medios ópticos).

En el límite sin retardo, cuando la velocidad de la luz es infinita y las interacciones son instantáneas, es posible descomponer la pérdida de energía y dicroísmo total como la suma de las contribuciones de los modos propios de la estructura. Dentro de este formalismo, predecimos que todos ellos generan una señal dicroica que da lugar a la compleja respuesta mostrada por la estructura. Por otra parte, calculamos las fuerzas y torques ejercidos sobre el tetrámero por cada una de las componentes de momento angular del vórtice. Como era de esperar, confirmamos la conservación del momento lineal y angular.

A pesar del notable interés acerca de las nanoestructuras plasmónicas quirales en los últimos años, el objetivo principal de la espectroscopia de dicroísmo circular es determinar la quiralidad de una única molécula. Con este propósito, estudiamos la interacción entre vórtices de electrones y moléculas, que describimos como dipolos eléctricos y magnéticos no ortogonales – una configuración que rompe la simetría especular. Derivamos una ley de escala universal para el dicroísmo exhibido por cualquier tipo de estructura que pueda ser caracterizada por polarizabilidades eléctricas y magnéticas cruzadas no nulas. Adicionalmente, también nos centramos en una biomolécula específica: la α-hélice, una estructura secundaria común de las proteínas. La interacción entre los vórtices y las biomoléculas puede tener aplicaciones químicas y farmacéuticas.

Una de las grandes ventajas del uso de electrones es su alta resolución espacial, debido a su corta longitud de onda de *de Broglie*. Hoy en día, los microscopios electrónicos alcanzan resoluciones por debajo del angstrom, mientras que los microscopios ópticos están limitados por la difracción y, en el mejor de los casos, su resolución es de alrededor de una decena de nanómetros. Sin embargo, la resolución en energías de los microscopios electrónicos se encuentra muy alejada de la de los ópticos.

En este contexto, la parte final de esta tesis está dedicada a la propuesta de una nueva técnica de espectroscopía que aúne la gran precisión espacial de los electrones con la alta resolución en energías de la luz. Este método se basa en el análisis de las ganancias y pérdidas estimuladas de energía que los electrones experimentan al interaccionar con una nanoestructura iluminada. Debido a la naturaleza evanescente de los modos de superficie de una partícula metálica, el electrón es capaz de emitir o absorber fotones, un proceso físico que está prohibido en el espacio libre debido a la conservación simultánea de energía y momento. Este fenómeno fue observado en un experimento pionero, en el que un haz de electrones interaccionó con un hilo de plata y un nanotubo de carbono en coincidencia con un pulso de luz. Sin embargo, los resultados experimentales no proporcionaron ninguna información acerca de la respuesta óptica de las nanoestructuras sondeadas.

En cambio, nosotros sugerimos que es posible analizar la respuesta espectral de la muestra mediante la variación de la frecuencia de la luz incidente. En concreto, estudiamos esferas con recubrimiento metálico (de oro y plata) y núcleo de óxido de silicio, que son resonantes en el infrarrojo cercano. Estimamos la probabilidad de ganancias y pérdidas de energía en función de la longitud de onda y la intensidad de la luz incidente, tanto en el caso de iluminación pulsada como continua. Cuando la frecuencia de la luz se aproxima a la de la resonancia plasmónica, la componente elástica de la función de onda del electrón comienza a despoblarse y la amplitud de los canales inelásticos aumenta. Para intensidades bajas, esta despoblación alcanza un máximo a la frecuencia de resonancia asociada al campo cercano. Curiosamente, la longitud de onda a la que la sección eficaz de extinción es máxima no coincide exactamente con la frecuencia a la que ocurre la mayor despoblación de la componente elástica del electrón. Esto es debido a que el acoplamiento entre fotones y electrones está mediado por el campo cercano, dominado por los plasmones de la nanoestructura.

Sorprendentemente, predecimos ganancias y pérdidas de energía sustanciales con intensidades de luz por debajo del umbral de fusión de las partículas, incluso con iluminación continua. Debido al carácter menos absorbente de la plata con respecto al oro, el aumento del campo inducido por las nanopartículas de plata es mayor, lo que conlleva la generación de eventos multifotónicos a intensidades más bajas. Por último, con el fin de dar cierta perspectiva a las probabilidades de ganancia obtenidas, las comparamos con las asociadas a técnicas espectroscópicas más tradicionales, tales como la pérdida de energía o la catodoluminiscencia (en la que los plasmones creados por los electrones decaen generando luz). Para tal fin, desarrollamos un modelo cuántico analítico y unificado, válido a bajas intensidades de luz. Esta aproximación perturbativa trata las espectroscopias mencionadas en igualdad de condiciones y proporciona una mayor comprensión acerca de los procesos físicos en los que se fundamentan.

La Nature est un temple où de vivants piliers
Laissent parfois sortir de confuses paroles;
L'homme y passe à travers des forêts de symboles
Qui l'observent avec des regards familiers.

Charles Baudelaire[1]

1

Introduction

In this chapter we provide a succinct introduction to the fundamental concepts that constitute the physical foundations of this thesis. In particular, we briefly review basic equations for electromagnetic fields, chiral interactions between light and matter, the behavior of electromagnetic fields in metals, and the interaction of electron beams with metallic structures.

1.1 Classical electrodynamics

Maxwell's equations

We first start by reviewing Maxwell's equations,[2] which govern the dynamics of electromagnetic fields. The classical description of light depicts electromagnetic fields as waves that fulfill the following macroscopic expressions: [1]

$$\nabla \cdot \mathbf{D}(\mathbf{r},t) = 4\pi\rho(\mathbf{r},t), \tag{1.1a}$$

$$\nabla \cdot \mathbf{B}(\mathbf{r},t) = 0, \tag{1.1b}$$

$$\nabla \times \mathbf{E}(\mathbf{r},t) = -\frac{1}{c}\frac{\partial}{\partial t}\mathbf{B}(\mathbf{r},t), \tag{1.1c}$$

$$\nabla \times \mathbf{H}(\mathbf{r},t) = \frac{1}{c}\left[\frac{\partial}{\partial t}\mathbf{D}(\mathbf{r},t) + 4\pi\mathbf{j}(\mathbf{r},t)\right], \tag{1.1d}$$

where **E** and **H** denote the electric and magnetic fields, respectively; **D** is the electric displacement; and **B** represents the magnetic induction. The sources of the fields are electric charges and their associated currents, which are represented by the local densities ρ and $\mathbf{j}$, respectively.

Maxwell's equations must be complemented by other expressions that relate the response of matter to electromagnetic fields, the so-called constitutive equations. For a linear, isotropic, homogeneous, and non-magnetic medium, these read

$$\mathbf{D}(\mathbf{r},t) = \int d\mathbf{r}' dt' \epsilon(\mathbf{r}-\mathbf{r}', t-t')\mathbf{E}(\mathbf{r}',t'),$$

$$\mathbf{H}(\mathbf{r},t) = \mathbf{B}(\mathbf{r},t),$$

where ϵ is the dielectric function. This thesis deals with the optical response of metallic nanoparticles of characteristic sizes larger than the electron Fermi wavelength (~ 0.5 nm in gold and silver). Therefore, the dielectric function is regarded as local (this is, we drop the spatial dependence on the position). On the other hand, metals exhibit strong temporal dispersion at optical frequencies, which needs to be taken into consideration. Thus, it is convenient to know the spectral behavior of the fields, which can be obtained by writing them in terms of different frequency components as

$$\mathbf{E}(\mathbf{r},t) = \frac{1}{2\pi}\int_{-\infty}^{\infty} d\omega\, \mathbf{E}(\mathbf{r},\omega)\, e^{-\mathrm{i}\omega t}.$$

---

[1] These equations are written in the Gaussian system of units, which is employed throughout this thesis.

The condition of reality of the fields imposes that

$$\mathbf{E}(\mathbf{r},-\omega)=\mathbf{E}^{*}(\mathbf{r},\omega),$$

and the same holds for the dielectric function. Hence, the spectral components of the fields follow Maxwell's equations in the frequency domain:

$$\begin{aligned}
\nabla\cdot\mathbf{D}(\mathbf{r},\omega) &= 4\pi\rho(\mathbf{r},\omega),\\
\nabla\cdot\mathbf{B}(\mathbf{r},\omega) &= 0,\\
\nabla\times\mathbf{E}(\mathbf{r},\omega) &= \mathrm{i}k\mathbf{B}(\mathbf{r},\omega),\\
\nabla\times\mathbf{H}(\mathbf{r},\omega) &= -\mathrm{i}k\mathbf{D}(\mathbf{r},\omega)+\frac{4\pi}{c}\mathbf{j}(\mathbf{r},\omega),
\end{aligned}$$

where $k=\omega/c$ is the light wave-vector. Besides, the constitutive equations are simply written as

$$\begin{aligned}
\mathbf{D}(\mathbf{r},\omega) &= \epsilon(\omega)\mathbf{E}(\mathbf{r},\omega),\\
\mathbf{H}(\mathbf{r},\omega) &= \mathbf{B}(\mathbf{r},\omega),
\end{aligned}$$

where the frequency-dependent response of the medium to electromagnetic fields is fully contained in $\epsilon(\omega)$. The specific expression of the dielectric function of metals will be given in an upcoming section.

Linear and angular momenta of the electromagnetic field

The physical consistency of Maxwell's equations guarantees the conservation of charge, as expressed by the continuity equation

$$\frac{\partial}{\partial t}\rho(\mathbf{r},t)+\nabla\cdot\mathbf{j}(\mathbf{r},t)=0.$$

Moreover, the energy and the linear and angular momenta are also conserved. For the sake of simplicity, we shall write these quantities for the free electromagnetic field. They read:[3]

$$\begin{aligned}
&\text{Energy density} && W=\frac{1}{8\pi}\left[|\mathbf{E}(\mathbf{r},t)|^{2}+|\mathbf{H}(\mathbf{r},t)|^{2}\right]\\
&\text{Linear momentum density} && \mathbf{P}=\frac{1}{4\pi c}\left[\mathbf{E}(\mathbf{r},t)\times\mathbf{H}(\mathbf{r},t)\right]\\
&\text{Angular momentum density} && \mathbf{J}=\mathbf{r}\times\mathbf{P}=\frac{1}{4\pi c}\mathbf{r}\times\left[\mathbf{E}(\mathbf{r},t)\times\mathbf{H}(\mathbf{r},t)\right]
\end{aligned}$$

These expressions are directly worked out from Eqs. (1.1). They can also be derived by observing the invariance of the Lagrangian of the electromagnetic field under certain infinitesimal transformations.[4] Specifically, symmetry under time displacements accounts for the conservation of energy, and linear and angular momenta are related to the invariance under space translations and rotations, respectively.

Due to the conservation of linear and angular momenta, the interaction of electromagnetic fields with matter results in the exertion of mechanical forces and torques, respectively. Actually, almost five hundred years ago, Johannes Kepler suggested that comet tails originate from the radiation pressure exerted by light coming from the sun. Nowadays, optical forces are crucial tools in nanotechnology. For instance, the many applications of optical tweezers (focused laser gradient-force traps, developed by Ashkin in 1970[5]) range from manipulating viruses and bacteria[6,7] to studying non-equilibrium thermodynamic properties of mesoscopic systems.[8,9]

This thesis pays special attention to the angular momentum of light, which is comprised of two different contributions. The spin component is connected to circular polarization, whereas the orbital part is associated with helical phase fronts of the fields.[10] A century ago, Poynting[11] inferred that a circularly-polarized beam carries angular momentum. This prediction was demonstrated by Beth[12] twenty years later. Since then, the angular momentum properties have been exploited in many different ways, such as in the detection of the rotational motion of a spinning body,[13,14] the characterization of light radiated by distant exoplanets[15] or for encoding quantum information.[16–18] Besides, circularly polarized light is crucial to determine chiral properties of matter, which will be discussed hereafter.

1.2 Chirality and circular dichroism

As mentioned in the previous section, symmetries play a fundamental role in physics. Until the second half of the 20th century, it was believed that all laws of nature conserved parity or, in other words, that a given experiment would yield the same outcome when reflected on a mirror. [1] Except for weak interactions,[20,21] the other fundamental forces of nature –strong interactions, gravitation, and electromagnetism– are invariant under spatial inversion (parity operation). [2]

---

[1] The discovery that weak interactions violate the conservation of parity was quite shocking for most of the physics community. However, Dirac was not very surprised. He adduced that the laws of physics should be invariant under transformations that could be regarded as the sum of infinitesimal increments (translations and rotations), but not discrete ones, like reflections or inversions.[19]

[2] The CPT Theorem states that all laws of physics (including weak forces) are invariant with respect to the product of charge conjugation, parity, and time reversal operations. Hitherto, there is no experimental evidence of the violation of this theorem.

Operator	Space Parity	Time Reversal
Hamiltonian	+	+
Angular momentum	+	−
Electric field	−	+
Magnetic field	+	−
Electric dipole	−	+
Magnetic dipole	+	−

Table 1.1: Transformation properties of some basic physical observables under parity and time reversal operations. The symbol + stands for even and − denotes odd.

Of course, this does not mean that every electromagnetic interaction should be achiral. In fact, mirror-symmetry breaking (chiral) structures are ubiquitous in nature. Not only our hands are not superimposable onto their mirror image, but most biological molecules, such as proteins or glucids, exhibit two different spatial flavors. These enantiomers are often present in only one of their two possible configurations. This selectivity is called homochirality and its origin and purpose still remain a mystery.[22]

Although chiral structures are indistinguishable under many physical or chemical experiments, they behave differently when probed with chiral sources. When interacting with chiral matter, the polarization plane of linearly polarized light – which is a superposition of LCP and RCP light – rotates. This phenomenon is called optical activity, and it was already discovered in the 18th century.[23,24] The measurement of this quantity over a whole range of light wavelengths gives rise to the so-called optical rotatory dispersion. Moreover, the difference in the absorption of left- and right-circularly polarized light by a chiral medium receives the name of circular dichroism. Both quantities are extremely connected, since they are Kramers-Kronig transforms[25] of each other. Precisely, the study of CD is the prevalent method to characterize chiral samples.

Now, we would like to give a brief explanation of the necessary conditions that are needed for a molecule to be chiral. We describe the molecule as possessing both electric, $\mathbf{p}$, and magnetic, $\mathbf{m}$, dipoles. [1] The interaction Hamiltonian that characterizes the coupling between the molecule and the electromagnetic radiation is based on the Power–Zienau–Woolley[26] multipolar representation and yields

$$H_{\text{int}} = -\mathbf{p} \cdot \mathbf{E} - \mathbf{m} \cdot \mathbf{H},$$

---

[1] Details about the electric and magnetic moments of chiral molecules are given in Appendix B.

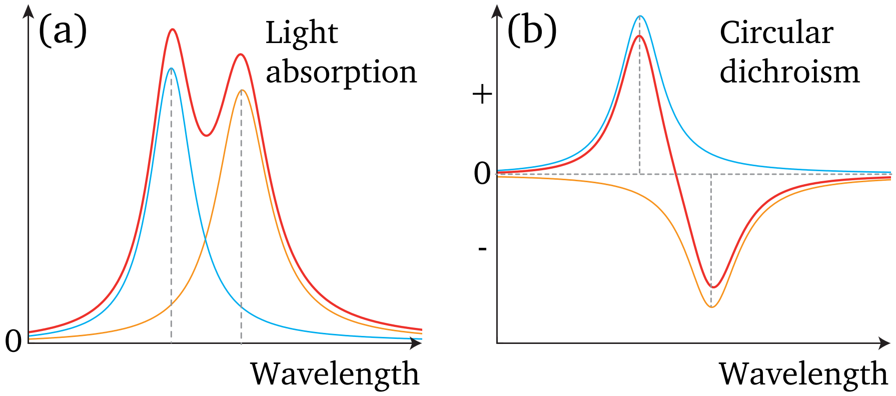

Figure 1.1: Sketch of the optical properties of a chiral structure (see more details in the main text). (a) LCP light absorption cross-section. (b) Circular dichroism, computed as the difference in the absorption of LCP and RCP light. The structure exhibits two resonances with opposite chiroptical behavior (blue and orange curves). The total extinction and CD are represented by the red curve.

where **E** and **H** are the electric and magnetic fields at the position of the molecule, respectively. Rosenfeld[27,28] demonstrated that, for a specific transition between different electronic states, the circular dichroism can be expressed in terms of the scalar product of the electric and magnetic dipoles as

$$\mathrm{CD} \propto \mathrm{Im}\{\mathbf{p}\cdot\mathbf{m}\}. \tag{1.3}$$

The same expression is obtained when considering a classical interaction between electric and magnetic dipoles and the fields. It is then clear that chiral response is only manifested when the dipoles are non-orthogonal. In a heuristic manner, one could argue that the dichroism appears because the electric dipole displaces the electronic charges and, simultaneously, the magnetic dipole induces a current loop that, in conjunction, give rise to a specific handedness or helical arrangement of the molecule's charge distribution.

On the other hand, technically speaking, chiral systems are defined as those that support time-even pseudoscalar observables (scalar quantities that change sign under parity operation). [1] Taking into account the behavior of electric and magnetic fields under space inversion in Table 1.1, it can be easily seen that Eq. (1.3) represents one

---

[1] For more details, the reader is referred to Refs.[29,30]

of such physical quantities. Furthermore, circularly polarized photons are characterized by their helicity,[31] which is also a time-even pseudoscalar. This is precisely the reason why CP light chiral influence is employed to probe chiral matter.

Figure 1.1 shows typical light extinction and CD spectra of an arbitrary chiral structure with two resonances. Both of them contribute with a Lorentzian curve to the CD, which arises due to the frequency dependence of the electric and magnetic dipoles. The scalar product of Eq. (1.3) has been chosen to have opposite sign in each of the resonant features and the CD spectrum has a bisignated character, which is very commonly encountered in biological molecules.[29,30] Typically, biomolecules absorb light in the UV region, but dichroic behavior can be extended toward the visible by using metallic nanostructures.[32,33]

1.3 Electromagnetic fields in metals

The electromagnetic response of metals is governed by conduction electrons. In the jellium approximation, the effect of the ion lattice is neglected and electrons can be considered to form a high density liquid ($\sim 10^{23}$ electrons per cm^3). Electrons' energy levels form a continuum distribution and even minuscule nanoparticles (down to a few nanometers) can be classically characterized by an effective dielectric function.

Electrons interact with each other via long-range Coulomb forces. However, in the spirit of Landau's Fermi liquid theory,[34–36] many of the physical properties of metals can be predicted by relying on the idea of independent-particle behavior. In particular, sophisticated fully microscopic calculations yield the same expression for the dielectric permittivity as that obtained within the simple Drude-Sommerfeld model. This dielectric function is given by the well-known expression[37]

$$\epsilon_m = \epsilon_b - \frac{\omega_p^2}{\omega(\omega + \mathrm{i}\gamma)}, \tag{1.4}$$

where the interband transitions are taken into account by adding a background permittivity ϵ_b (which is constant in the range of interest), the losses are characterized by γ, and

$$\omega_p = e\sqrt{4\pi n/m_e} \tag{1.5}$$

is the plasma frequency of the metal. In the above expression m_e and e are the electron mass and charge, respectively, and n is the electronic density. The plasma frequency is a crucial parameter in the response of metals to light:

- For frequencies above $\omega_p/\sqrt{\epsilon_b}$, metals behave like dielectrics and allow the propagation of light ($\epsilon_m > 0$).
- For frequencies below $\omega_p/\sqrt{\epsilon_b}$, electrons are able to screen the radiation. Therefore, metals do not tolerate the penetration of light and display a highly reflective behavior ($\epsilon_m < 0$).

Many-body effects in the electron plasma lead to the existence of collective charge density waves, called plasmons, which dictate the optical response at high frequencies. Depending on the boundary conditions, plasmons have different nature and behavior.

Bulk plasmons

Collective oscillations of electron plasma in the bulk of metals are called bulk or volume plasmons. These oscillatory eigenmodes trivially satisfy Maxwell's equations in the absence of any external source by imposing three conditions: null magnetic field, longitudinal electric field ($\nabla \times \mathbf{E} = 0$), and zero permittivity. As dictated by Eq. (1.4), the frequency of these excitations is precisely the plasma frequency. Due to the transverse character of electromagnetic radiation and the high frequencies of bulk plasmons (typically $\sim 5 - 15$ eV), these modes are not exploited in photonics. Nevertheless, they can be generated by swift electrons.[38] Shortly after the discovery of volume plasmons by electron bombardment, Ritchie proposed to study the effect of boundaries on the generation of collective excitations[39] and only two years later surface plasmons were first observed in electron energy-loss experiments.[40]

Surface plasmon polaritons

Surface plasmon polaritons are propagating solutions of Maxwell's equations at the interface of metals and dielectrics. Unlike bulk plasmons, surface plasmons are of transverse nature ($\nabla \cdot \mathbf{E} = 0$) and are related to non-zero magnetic fields in both the metal and the dielectric regions. The electromagnetic field at the boundary between two media obeys the continuity relations

$$\hat{\mathbf{r}} \times (\mathbf{E}_m - \mathbf{E}_d) = 0, \tag{1.6a}$$

$$\hat{\mathbf{r}} \cdot (\mathbf{D}_m - \mathbf{D}_d) = 4\pi\rho_s, \tag{1.6b}$$

$$\hat{\mathbf{r}} \times (\mathbf{H}_m - \mathbf{H}_d) = \frac{4\pi}{c}\mathbf{j}_s, \tag{1.6c}$$

$$\hat{\mathbf{r}} \cdot (\mathbf{B}_m - \mathbf{B}_d) = 0, \tag{1.6d}$$

where ρ_s and $\mathbf{j}_s$ are the external surface charge and current densities, respectively. Surface plasmon polaritons are homogeneous solutions of the wave equation for the electric field

$$\nabla \times \nabla \times \mathbf{E}(\mathbf{r}, \omega) - k^2 \epsilon(\mathbf{r}, \omega) \mathbf{E}(\mathbf{r}, \omega) = 0,$$

imposing the boundary conditions of Eqs. (1.6) in the absence of external sources ($\rho_s, \mathbf{j}_s = 0$). There are two kinds of waves that satisfy the above expressions: transverse magnetic (p) modes and transverse electric (s) modes, whose magnetic and electric fields, respectively, are orthogonal to the propagation direction. However, a careful analysis shows that transverse electric waves are not surface modes and propagate in the bulk.[41] Therefore, surface plasmon polaritons are p-polarized waves. Denoting by ϵ_m and ϵ_d the dielectric function of the metal and dielectric regions, SPPs satisfy the following dispersion relation:

$$k_{spp} = \frac{\omega}{c} \sqrt{\frac{\epsilon_m \epsilon_d}{\epsilon_m + \epsilon_d}}, \tag{1.7}$$

where k_{spp} is the wave-vector along the propagation direction. On the other hand, the normal component of the wave-vector in each of the interfaces is

$$k_{\perp,j} = \frac{\omega}{c} \sqrt{\frac{\epsilon_j^2}{\epsilon_m + \epsilon_d}}, \tag{1.8}$$

where $j = m, d$. Surface plasmon polaritons posses propagating character along the surface ($\mathrm{Re}\{k_{SPP}\} \neq 0$) and are evanescent – with an exponential decay – in the perpendicular direction ($\mathrm{Im}\{k_{\perp,j}\} > 0$). These conditions impose the following restrictions on the allowed value of the dielectric function of the metal:

$$\begin{aligned} \epsilon_m + \epsilon_d &< 0, \\ \epsilon_m \cdot \epsilon_d &< 0, \end{aligned}$$

which are fulfilled below $\omega_p / \sqrt{\epsilon_b}$, as shown by Eq. (1.4).

Figure 1.2 shows the relation dispersion of an SPP, as given by Eq. (1.7). The plasmon propagates at an interface between vacuum ($\epsilon_d = 1$) and a Drude metal with negligible losses ($\gamma = 0$) and a background permittivity of $\epsilon_b = 9.5$, which is a typical value used to fit tabulated data for gold.[42] According to the figure, there are two different modes of distinct nature. The one above the so-called surface plasmon frequency $\omega_s = \omega_p / \sqrt{\epsilon_b + 1}$ is a Brewster mode: it is not bounded to the interface ($\mathrm{Re}\{k_{\perp,j}\} \neq 0$) and, therefore, it is not a surface mode. In contrast, the mode below ω_s propagates along the surface with a dispersion relation below the light cone which demonstrates its non-radiative nature. As the frequency approaches ω_s, the

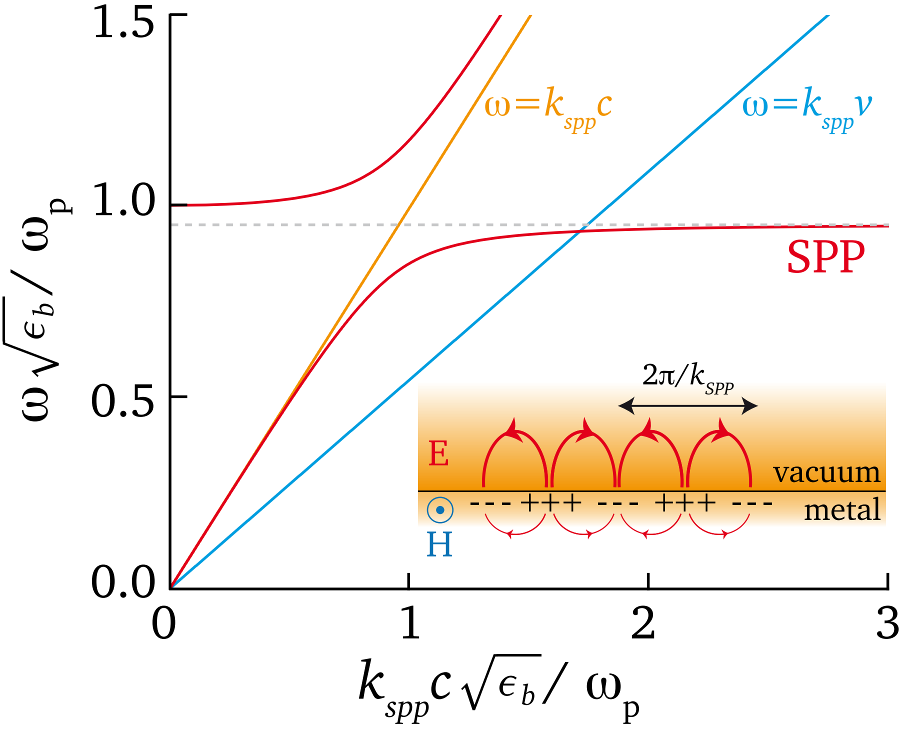

Figure 1.2: Dispersion relation of surface plasmon polaritons [red curve, see Eq. (1.7)] at the interface between vacuum and a Drude metal with negligible losses ($\gamma = 0$) and background permittivity taken to fit tabulated data of gold ($\epsilon_b = 9.5$).[42] The orange curve depicts the light line and the blue curve corresponds to the maximum energy transfer from an electron moving with velocity $v \simeq 0.55c$. Inset: Sketch of the electric (red) and magnetic (blue) fields of the SPP at the interface. The symbols $-$ and $+$ represent regions of high and low electron density, respectively.

group velocity tends to zero and the mode develops into an electrostatic excitation (becoming a solution of Laplace equation for an interface).[43] Since the SPP lies below the light cone, it is not possible to directly excite surface modes with light fields without special phase-matching techniques.[44] Nevertheless, as we will see in the following section, electron beams can excite SPPs. The blue curve in Fig. 1.2 depicts the maximum energy transfer from such a beam.

So far, the analysis of the dispersion of SPPs has been performed without taking into account ohmic losses. However, metals at optical frequencies are lossy materials. Damping affects the lifetime of the modes in a fundamental way: they are no longer well-defined excitations (eigenmodes), and they decay after a certain time. Losses limit both the propagation distance of SPPs and their degree of confinement to the interface. Typically, at optical frequencies, the propagation distance of SPPs is around tens of micrometers and the decay across the interface is ~ 25 nm into the metallic region and hundreds of nanometers into the vacuum.

Localized surface plasmons

Plasmons can also be supported by other metallic systems, without the requirement of translational invariance. In particular, plasmons exist in confining structures such as small particles of different geometries. These modes are constrained to the dimensions of the particle that supports them and are therefore called localized surface plasmons. LSPs couple directly to radiation, producing light absorption and scattering.

Solving Maxwell's equations for arbitrary geometries is a highly complex problem that often involves numerical computation. Nevertheless, an exact solution exists for spherically symmetric particles. It was first obtained by Gustav Mie in the early 20th century and it is nowadays known as Mie scattering theory.[45] This solution is based on expanding the internal and scattered fields as an infinite sum of vector harmonics around the center of the spherical structure.

In particular, the extinction cross-section (that includes both absorption and scattering processes) of a homogeneous sphere of radius a placed in vacuum reads[46,47]

$$\sigma^{ext} = \frac{\lambda^2}{2\pi} \sum_{l=1}^{\infty} (2l+1) \left[\mathrm{Im}\left\{ t_l^E \right\} + \mathrm{Im}\left\{ t_l^M \right\} \right],$$

in terms of the corresponding electric and magnetic Mie coefficients[48]

$$t_l^E = \frac{\epsilon_m j_l(\rho_m)\left[j_l(\rho_d)+\rho_d j_l'(\rho_d)\right] - j_l(\rho_d)\left[j_l(\rho_m)+\rho_m j_l'(\rho_m)\right]}{\mathrm{i}h_l^{(1)}(\rho_d)\left[j_l(\rho_m)+\rho_m j_l'(\rho_m)\right] - \epsilon_m j_l(\rho_m)\left[\mathrm{i}h_l^{(1)}(\rho_d)+\rho_d \mathrm{i}h_l^{(1)'}(\rho_d)\right]}, \tag{1.9a}$$

$$t_l^M = \frac{\rho_d j_l'(\rho_d) j_l(\rho_m) - \rho_m j_l(\rho_d) j_l'(\rho_m)}{\rho_m \mathrm{i}h_l^{(1)}(\rho_d)\, j_l'(\rho_m) - \rho_d \mathrm{i}h_l^{(1)'}(\rho_d)\, j_l(\rho_m)}, \tag{1.9b}$$

where l is the multipolar order, ϵ_m is the metal dielectric function inside the particle, and the primes indicate differentiation of the spherical Bessel and Hankel functions j_l and $h_l^{(1)}$ with respect to their arguments: $\rho_d = ka$ and $\rho_m = \sqrt{\epsilon_m}\rho_d$.

The poles of these coefficients give rise to different multipolar LSP resonances: dipolar (l=1), quadrupolar (l=2), hexapolar (l=3), etcetera. Incidentally, Mie theory predicts the existence of not only electric but also magnetic resonances. The latter result in very small extinction cross-sections at optical frequencies, but the magnetic response of the sphere might be relevant at far-IR regions.[49]

The extinction cross-section can also be defined in terms of the multipolar polarizabilities

$$\alpha_l^{E,M} = \frac{3}{2k^3} t_l^{E,M}. \tag{1.10}$$

In the non-retarded (electrostatic) limit, the electric polarizability of order l reduces to

$$\alpha = a^{2l+1}\frac{l(\epsilon_m - 1)}{l(\epsilon_m + 1) + 1}.$$

Inserting Drude dielectric function [see Eq. (1.4)] into the above equation, one is able to determine that electric multipolar resonances show up at frequencies

$$\omega = \omega_p \sqrt{\frac{l}{l(\epsilon_b + 1) + 1}}. \tag{1.11}$$

The previous expressions can be also derived by realizing that Maxwell's equations reduce to Poisson's equation in the electrostatic limit, since the electric and magnetic fields are uncoupled. As in the planar surface case, the latter does not produce plasmons in this regime, whereas the former leads to resonances at the frequencies given by Eq. (1.11). Remarkably, for very large l, the surface charge oscillations are not sensitive to the curvature of the structure and the resonance frequency evolves into that of SPPs ($\omega_s = \omega_p/\sqrt{\epsilon_b + 1}$).

For small enough spheres, the electric field inside them is constant, and their optical response is dominated by the dipolar mode ($l = 1$). The quasistatic polarizability is then

$$\alpha = a^3 \frac{\epsilon_m - 1}{\epsilon_m + 2}, \tag{1.12}$$

which, for metals described by Drude's dielectric function, presents a resonance at $\omega_p / \sqrt{\epsilon_b + 2}$ (which for gold and silver, lies in the visible regime). However, the above expression violates the optical theorem since light scattering is not taken into account. This can be corrected by including the particle interaction with its own radiated field.[50]

Spherical nanoshells also admit an analytical fully retarded solution of Maxwell's equations and their optical response depends on the thickness of the metallic coating that surrounds their core. In fact, slight variations of the crust radius imply large displacements of the resonance frequency, thus making nanoshells great hosts for easily-tunable LSPs. Other nanostructures, such as rods, also provide a fine tuning of their optical behavior by modifying the aspect ratio between their two main axis.

LSPs are of crucial importance in nanophotonics as they allow subwavelength confinement and enhancement of electromagnetic fields. Besides their fundamental interest, these features are responsible for the many applications that LSPs have in nanotechnology, ranging from quantum optics[51–54] and photovoltaic devices[55,56] to molecular sensing[57–59] or biomedicine.[60–62]

1.4 Electron beam interactions with metals

Light is only one of the many sources employed to study the physical properties of matter. In fact, techniques based upon particle scattering are precious components of physicists' toolkits. More than a century ago, Rutherford performed a pioneering experiment in which $\alpha-$particles were launched towards a thin gold foil.[63] The collected data showed that the formerly prevailing plum pudding model was not correct and led him to suggest a groundbreaking theory of the atomic structure. Some decades later, neutrons were first used in diffraction experiments in order to observe the structure of ice and the arrangement of magnetic moments in solids.[64]

As we will see hereafter, electron beams are perfect candidates to characterize the optical properties of metals. Actually, plasmons were first revealed as energy loss features in the spectra of electrons reflected from metallic surfaces.[40] Since then, electron beams have become an important tool to yield information on these plasma oscillations.[65,66] More recently, EELS has been extensively used to map plasmons in metallic nanostructures,[67,68] and it is thus helping to develop new applications of these collective modes.

Let's first start by giving an intuitive idea of why electrons are such good plasmonic probes. Within a classical formalism, a swift electron that moves in a homogeneous medium of permittivity ϵ describing a straight-line trajectory given by $\mathbf{r}_e(t) = \mathbf{v}t$ (with velocity $\mathbf{v} = \mathrm{v}\hat{\mathbf{z}}$ [1]) carries a charge density which reads

$$\rho\,(\mathbf{r}, t) = -e\,\delta(\mathbf{r} - \mathbf{v}t).$$

This moving charge creates a current density which reduces to

$$\mathbf{j}\,(\mathbf{r}, \omega) = \rho\,(\mathbf{r}, \omega)\,\mathbf{v} = -e\,\delta(\mathbf{R})\,e^{\mathrm{i}\frac{\omega}{\mathrm{v}}z}\,\hat{\mathbf{z}} \tag{1.13}$$

in the frequency domain, where the notation $\mathbf{r} = (\mathbf{R}, z)$ has been employed due to the cylindrical symmetry of the problem. From Maxwell's equations, the electric field created by the electron current yields

$$\mathbf{E}\,(\mathbf{r}, \omega) = \frac{\mathrm{i}}{\epsilon\omega} \int d^3\mathbf{r}'\,\mathcal{G}(\mathbf{r}, \mathbf{r}', \omega) \cdot \mathbf{j}\,(\mathbf{r}', \omega),$$

where

$$\mathcal{G}(\mathbf{r}, \omega) = \left(\epsilon k^2 \mathbb{1} + \nabla \otimes \nabla\right) \frac{e^{\mathrm{i}\sqrt{\epsilon}kr}}{r}$$

is the electromagnetic Green tensor of the medium. Plugging Eq. (1.13) into the expression for the field, we find

$$\mathbf{E}\,(\mathbf{r}, \omega) = \frac{2e\omega}{\gamma\epsilon\mathrm{v}^2} e^{\mathrm{i}\frac{\omega}{\mathrm{v}}z} \left[\frac{\mathrm{i}}{\gamma} K_0\left(\frac{\omega R}{\gamma\mathrm{v}}\right)\hat{\mathbf{z}} - K_1\left(\frac{\omega R}{\gamma\mathrm{v}}\right)\hat{\mathbf{R}}\right], \tag{1.14}$$

where $\gamma = 1/\sqrt{1 - \epsilon\mathrm{v}^2/c^2}$ is the Lorentz factor, and $K_{0,1}$ are modified Bessel functions of the second kind. A careful look into this expression reveals an exponential decay of the electric field at large distances in both the parallel and orthogonal directions to the trajectory. More importantly, the electron field has transversal as well as longitudinal components (in contrast to the transverse nature of plane waves). This is precisely the reason why electrons are able to excite both bulk and surface plasmons.

One can now consider the interaction between a plasmonic nanoparticle placed in vacuum ($\epsilon = 1$) and an electron beam that passes close by. The Coulomb field of the swift electron repels the surface charges on the nanoparticle inducing charge density waves. As the electron interacts for a very short time with the sample (less than a femtosecond for a 100 keV electron traveling close to a 20-nm sphere), it can be regarded as a highly focused white light source.[69] Therefore, by measuring the

---

[1] Throughout this thesis, the magnitude of an arbitrary vector $\mathbf{x}$ is indicated simply as x.

energy lost by the electron upon interaction, it is possible to spectrally map a wide range of excitations of the sample.

Certainly, due to energy-momentum conservation, there is a maximum allowed energy and momentum transfer from the electron to the excitations in the medium.[68] In the non-recoil approximation, an exchange of momentum $\mathbf{q}$ implies an energy transfer

$$\omega = \frac{1}{2\hbar} m_e \mathrm{v}^2 - \frac{1}{2\hbar m_e} |m_e \mathbf{v} - \hbar \mathbf{q}|^2 = \mathbf{q}\cdot\mathbf{v} - \frac{\hbar q^2}{2m_e} \simeq \mathbf{q}\cdot\mathbf{v}, \tag{1.15}$$

where the dot product results from taking into account all possible relative orientations between $\mathbf{v}$ and $\mathbf{q}$. In particular, the blue curve in Fig. 1.2 represents the maximum energy and momentum transfer from a 100 keV electron ($\mathrm{v} \simeq 0.55c$) to a medium that supports SPPs. The electron couples to all the modes below that line and, specifically, to the surface plasmon (red curve).

There are several ways to calculate the energy lost by an electron upon interaction with a sample, depending on whether or not we include retardation effects or the quantum nature of the electron and the target. One of the options is to compute it as the work exerted by an electric field upon a moving charge

$$\Delta E = -\int dt \int d\mathbf{r}\, \mathbf{j}(\mathbf{r},t)\cdot \mathbf{E}^{ind}(\mathbf{r},t),$$

where $\mathbf{E}^{ind}$ is the electric field induced by the current density, that acts back on the electron. In the frequency domain, this can be written as

$$\Delta E = \int_0^\infty d\omega\, \hbar\omega\, \Gamma(\omega),$$

where the energy-loss probability reads

$$\begin{aligned}\Gamma(\omega) &= -\frac{1}{\pi\hbar\omega}\int d\mathbf{r}\, \mathrm{Re}\left\{\mathbf{j}^*(\mathbf{r},\omega)\cdot \mathbf{E}^{ind}(\mathbf{r},\omega)\right\} \\ &= \frac{1}{\pi\hbar\omega^2}\int d\mathbf{r} \int d\mathbf{r}'\, \mathrm{Im}\left\{\mathbf{j}^*(\mathbf{r},\omega)\cdot \mathscr{G}(\mathbf{r},\mathbf{r}',\omega)\cdot \mathbf{j}(\mathbf{r}',\omega)\right\}.\end{aligned}$$

Therefore, the full electromagnetic response of the medium is collected in the Green tensor, and the electron is characterized by its current density.

As in the calculation of light extinction by arbitrary structures, analytical expressions for the energy-loss probability are only known for specific geometries. Nevertheless, the simple case of an electron interacting with a spherical particle admits a solution in terms of Mie coefficients [given by Eqs. (1.9)].[70,71] The red curve in Fig. 1.3 (a) shows the electron energy loss suffered by a 100 keV electron passing 1 nm away from the surface of a 20-nm sphere. The dielectric function of the sphere follows Eq. (1.4) with $\omega_p = 8.89$ eV, $\gamma = 0.071$ eV and $\epsilon_b = 1$. These are typical values taken to fit tabulated data for gold,[42] but neglecting interband transitions in order to show high-energy multipolar resonances that would otherwise be hindered. Light extinction cross-section and cathodoluminescence (light emission induced by electron excitation) probability are also displayed in blue and orange curves, respectively. Non-dipolar modes do not couple to light (*i. e.*, they are *dark* for sufficiently small particles) and do not appear as resonant features in the light extinction and CL spectra. On the contrary, the energy-loss spectrum reveals all multipolar excitations.[72,73] Due to the small dimensions of the sphere, the resonances can be accurately predicted by Eq. (1.11) and high order peaks' frequencies saturate towards the surface plasmon value $\omega_s = \omega_p/\sqrt{2}$.

Besides the ability to unveil dark plasmonic modes, electron beams also provide information about the spatial distribution of the excitations. The left column of Fig. 1.3 (b) displays EELS maps associated with different resonant energies. [1] The right column shows the induced surface charges generated when the electron passes close to the particle. In fact, the charge patterns allows one to determine whether a given resonance corresponds to a specific multipolar excitation.

It is unquestionable that electrons' capacity to access near fields makes TEMs great tools to spatially probe surface plasmons. Nowadays, the resolution of electron microscopes is down to $\sim 1\,\text{Å}$,[76] just a factor of ~ 40 larger than the de Broglie wavelength at typical electron-beam energies $\sim 200\,$keV. This resolution is extremely high when compared to that of optical microscopes, which is diffraction limited.[77] The energy resolution of TEMs is also improving. For example, plasmons have been recently mapped in silver nanowires with an impressive energy resolution $< 0.1\,$eV relying on a new generation of transmission electron microscopes that are equipped with electron monochromators.[78] However, it is still limited by the spectral width of the electron beams, the energy response of the spectrometer, and the zero-loss peak (generated by the electrons that have not undergone inelastic scattering).

As a final comment, we should remark that electrons do not only yield information about the low-loss region – from 0.5 to 50 eV, where plasmonic excitations appear– but also provide important knowledge of core excitations – from 50 eV to several keV. High energy features reveal electronic and chemical properties of the samples.[79–81]

---

[1] EELS maps are generated by calculating the energy loss of the electron at different positions employing boundary element method.[74,75]

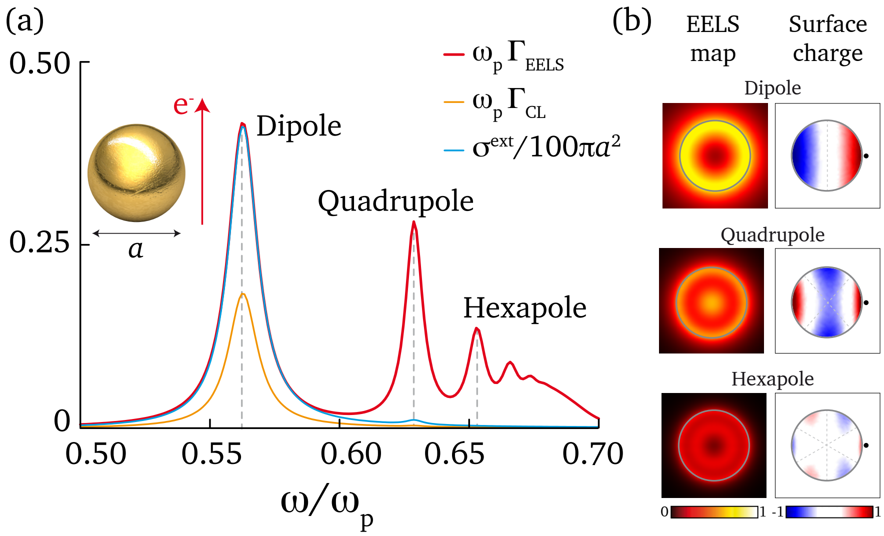

Figure 1.3: (a) Comparison between the extinction cross-section (blue curve) and EELS and CL probabilities (red and orange curves, respectively) for a metal sphere whose dielectric function follows Eq. (1.4) with $\epsilon_b = 1$, $\omega_p = 8.89$ eV, and $\gamma = 0.071$ eV (Drude parameters for gold, neglecting interband transitions). The diameter of the sphere is $a = 20$ nm and the 100-keV electron is passing at 1 nm from the surface. (b) Energy-loss maps (left) and induced surface charge (right) at the energies of different multipolar resonances, in arbitrary units. The black dot in the left plots depicts the electron trajectory for which the surface charge is calculated.

1.4.1 Electron beams and light fields

In free space, net emission or absorption of photons by electrons are forbidden processes, as can be seen from Eq. (1.15), since the velocity of the latter is always smaller than the speed of the former. However, electrons' interaction with matter shall give rise to the emission of light. The paradigmatic example of this phenomenon is Cherenkov radiation,[82] generated by electrons that travel faster than light in a given medium ($v > c/\sqrt{\epsilon}$). Generation of radiation might occur when an electron crosses a metal surface, since the cancellation of its image charge induces an effective dipole that subsequently radiates.[83,84] One further example of light emission by electrons is diffraction radiation, which arises when the electron travels near nanostructured interfaces,[85] such as metallic gratings.[86,87]

All the above processes are examples of cathodoluminescence. In particular, SPP cathodoluminescence has been observed by outcoupling propagating plasmons in metallic thin films using gratings.[88–90] In the case of metallic nanoparticles, light emission is generated by radiative decay of plasmons, due to their finite life-time. Although much weaker than EELS signal, CL also benefits from a high spatial resolution provided by electrons.[91–93] However, not all plasmonic modes decay radiatively – only *bright* ones do – and CL spectra typically present less resonant features than EELS spectra. This phenomenon is clearly shown in Fig. 1.3 (a), where only the dipolar mode displays a significant CL probability.

Electron energy-gain spectroscopy

So far we have analyzed the emission of radiation by electrons. The question then arises: is it possible to reverse the process? Is it possible for electrons to absorb a photon, gaining energy? Actually, energy gains by electrons are not unknown. Nearly half a century ago, an experiment was performed in which electrons absorbed thermal phonons of a LiF sample[94] (recently, this process has been mapped with atomic resolution in $SrTiO_3$[95]). A few years later, energy-gains were observed to be produced by absorption of surface plasmons previously generated by other electrons in an intense beam.[96]

Due to the energy-momentum mismatch, electrons are not able to absorb photons in free space. Nevertheless, illuminated nanostructured materials take the role of couplers: electron beams would absorb laser-generated plasmons in the vicinity of the structures, since the evanescent components provide enough momentum. Figure 1.4 represents a sketch of the process and the resulting energy spectrum. When the laser is off, the spectrum displays two peaks: one corresponds to electrons that have not lost any energy, centered at $\omega = 0$, and the other represents the excitation of a

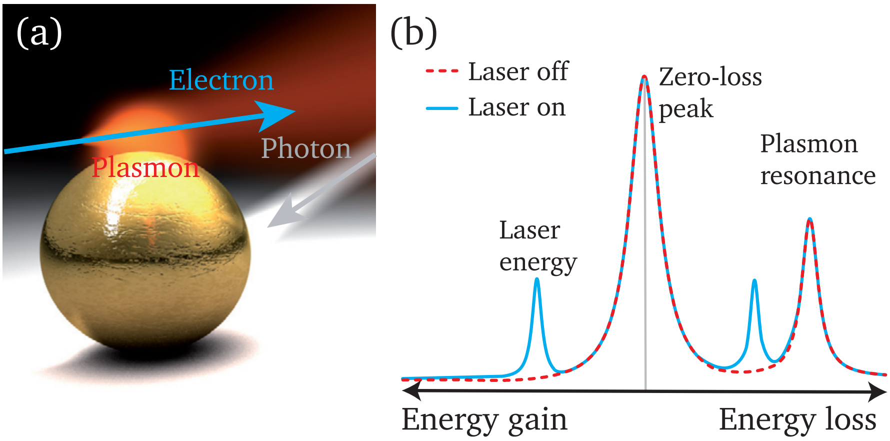

Figure 1.4: Sketch of EEGS. (a) A swift electron interacts with the plasmons of an illuminated nanoparticle. (b) Electron energy loss and gain spectra showing characteristic peaks at the laser frequency when the particle is illuminated.

	Spatial resolution	Energy resolution
Optical microscope	Diffraction-limited	$\sim$ meV
Electron microscope	$\sim$ 1Å	$\sim$ 0.1 eV
EEGS-based microscope	$\sim$ 1Å	$\sim$ meV

Table 1.2: Comparison between different microscopy techniques.

plasmon in the nanostructure. When the laser is turned on, two symmetrical peaks appear at the laser frequency, due to gains and stimulated losses of an evanescent photon.

Remarkably, EEGS combines both the spatial resolution of electron beams and the energy resolution of the photons, which is only limited by the spectral width of the external illumination. The advantages of EEGS-based microscopy are summarized in Table 1.2. The energy resolution of this technique would be much higher than that displayed by regular EELS-based TEMs. Of course, the low-energy excitations would still be hindered by the zero-loss peak, but higher-energy modes would be resolved with excellent accuracy. Moreover, the use of pulsed laser beams would add temporal control over the excitations.

However, EEGS requires a state-of-the-art electron microscope with integrated optics, which is extremely challenging. A pioneering experiment was performed by Ahmed Zewail's group only a few years ago,[97] which demonstrated the feasibility of observing laser-induced energy gains. Some other experiments have been carried out afterwards,[98, 99] yielding promising results.

The final result, the physical truth, interests me, almost regardless of who finds it first. It would be enough if only I had the strength to understand it!

Yakov B. Zel'dovich

2

Stimulated light emission and scattering by rotating particles

The rotational dynamics of particles subject to external illumination produces light amplification and inelastic scattering at high rotation velocities. Light emission at frequencies shifted with respect to the incident light by twice the rotation frequency dominates over elastic scattering within a wide range of light and rotation frequencies. Remarkably, net amplification of the incident light is produced in this classical system via stimulated emission. Large optically induced acceleration rates are predicted in vacuum accompanied by moderate heating of the particle, thus supporting the possibility of observing these effects under extreme rotation conditions.

2.1 Introduction

Every interaction between light and matter implies an exchange of momentum. Despite its minuteness, this transfer is responsible for observable phenomena ranging from the formation of comet tails to the trapping[5, 100] and cooling[101] of small particles down to single atoms. As discussed in the previous chapter, light carries both linear and angular momenta. The linear momentum of a photon of frequency ω is a vector which points in the propagation direction and whose magnitude is simply $\hbar\omega/c$, where $\hbar$ is the reduced Planck constant and c is the speed of light. From the two contributions of different physical origin to the angular momentum, it is the intrinsic one that plays a crucial role in the present chapter. The spin angular momentum is related to the chirality of the two circular polarization states (the so-called helicity): its magnitude is $\hbar$ and is oriented either parallel or anti-parallel to the propagation direction.

Due to the conservation of angular momentum, light might exert mechanical torques on matter. In a pioneering experiment, Beth showed that optical spin can induce rotation in birefringent plates illuminated by CP light.[12] This effect has been subsequently confirmed on the macro-,[102] micro-,[103] and nanoscales.[104, 105] On the other hand, angular orbital momentum has also been widely used to produce vortex-like motion of microparticles.[106] Additionally, under certain configurations, particles undergo rotation even when illuminated by linearly polarized plane waves (*i.e.*, light without net angular momentum); for instance, helical-shaped particles[107] or elongated structures that spin if the incident polarization is rotated.[108]

The interaction of light with rotating particles raises fundamental questions, such as the possibility of cooling the rotational degrees of freedom down to the quantum regime. On the opposite side, the material response of particles rotating at extreme velocities can be largely influenced by spinning forces, eventually leading to centrifugal explosion. In particular, recent experimental results demonstrate rotational velocities up to 5 MHz for microparticles in vacuum.[109] Moreover, even the kinematic change between lab and rotating frames is known to produce frequency shifts in the light emitted by rotating particles.[110–113] These effects might occur in cosmic dust irradiated by polarized light over enormous periods of time. Particle trapping in vacuum[114] may provide a suitable framework to analyze these phenomena.

In this chapter, we study the electromagnetic torque and scattering properties of rotating particles subject to external illumination. The chapter is divided in four sections. First, we show the physical model that describes a rotating induced dipole and we derive critical expressions such as the mechanical torque, the absorbed power, and the scattering cross-sections for a rod-like particle. We observe that, as in rotational Raman scattering,[13] the particle produces inelastic scattering at frequencies separated from the incoming light by twice the rotation frequency. Also, at large spinning velocities, inelastic scattering is stronger than elastic scattering. The second section shows how to connect the properties of this toy-model with those of actual particles, characterized by a given polarizability, like metallic rods or spheres. In the third section, we demonstrate that net amplification of the incident light takes place via stimulated emission. We base this conclusion on analytical expressions derived for the mechanical and extinction cross-sections, from which a complex resonant interplay between the light frequency and the particle rotation frequency is observed. Feasible experimental conditions for the observation of light amplification are discussed. Finally, we overview how long does it take to accelerate a particle up to a given rotational frequency and discuss whether this is possible without reaching the melting point of the material. We show remarkably high rotational frequencies for both a gold nanosphere and a carbon nanotube.

2.2 Physical model and dynamical properties

In this first section we introduce a toy-model in order to describe a spinning particle illuminated by a monochromatic electromagnetic field. This simplified physical system allows one to understand the crucial physics involved in the interaction as well as to predict surprising behaviors like inelastic light scattering or stimulated emission.

Oscillator model for a spinning particle

For the sake of simplicity, we consider a spinning rod, whose optical response can be modeled with an effective spring consisting of a point particle of mass m and charge Q oscillating around a fixed charge $-Q$ with natural frequency ω_0 and damping rate γ. The point-particle motion of the charge is constrained to the longitudinal direction of the rod $\hat{\rho}$, which is rotating with frequency Ω around a direction $\hat{\mathbf{z}}$ perpendicular to $\hat{\rho}$ (see Fig. 2.1), so that the instantaneous position of this charge can be written as

$$\mathbf{r}(t) = \rho(t)\hat{\rho}, \tag{2.1}$$

where $\rho(t)$ is the distance to the central charge. The force equation of motion is then given by

$$m\ddot{\mathbf{r}} = -m\omega_0^2\rho\hat{\rho} - m\gamma\dot{\rho}\hat{\rho} + Q\mathbf{E} + m\tau\dddot{\mathbf{r}} + F^{\text{react}}\hat{\varphi}. \tag{2.2}$$

In the above equation, the terms on the right-hand side are (from left to right):

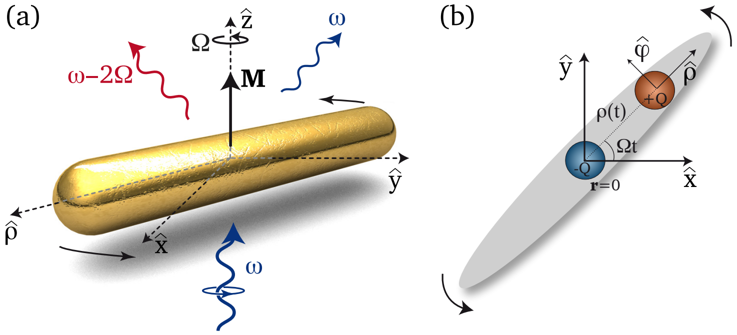

Figure 2.1: Sketch of a rod-like particle rotating with frequency Ω around a transversal direction (z axis). (a) An incident light plane wave of frequency ω illuminates the rod along a direction normal to its axis, thus producing an electromagnetic torque **M** and scattered light of frequencies ω and $\omega \pm 2\Omega$. For LCP light, as considered in the figure, only the $\omega - 2\Omega$ inelastic component is emitted. (b) Physical analogy of the rotating dipole: a charge Q rotates with frequency Ω around a static charge $-Q$. The moving charge oscillates along the rod axis.

- the restoring force;
- the intrinsic (non-radiative) friction;
- the external field force;
- the Abraham-Lorentz force, which includes radiation damping proportional to $\tau = 2Q^2/3mc^3$.[3,115] The oscillating charge, due to its accelerated motion, emits radiation and, therefore, loses energy and momentum. Within the formalism of non-relativistic classical electrodynamics, the easiest way to account for radiation reaction is via this self-force. In fact, the inclusion of this term guarantees the conservation of energy, and gives rise to a radiatively correct expression for the polarizability [see Eq. (2.14)];
- the particle reaction force F^{react}, taken to cancel other azimuthal components in order to constrain the motion of the point charge along the rotating $\hat{\rho}$ axis,

$$F^{\text{react}} = (m\ddot{\mathbf{r}} - Q\mathbf{E} - m\tau\dddot{\mathbf{r}}) \cdot \hat{\varphi}. \tag{2.3}$$

In what follows, we make two approximations that simplify the calculations and do not alter the validity of the model. First, the transversal polarization of the rod is considered to be negligible. Second, the magnetic component of the force is overlooked (although it could lead to a small precession), since the charge velocity is assumed to be small compared to the speed of light.

The radial and azimuthal unit vectors depend on time as $\hat{\rho} = \hat{\mathbf{x}}\cos\Omega t + \hat{\mathbf{y}}\sin\Omega t$ and $\hat{\varphi} = -\hat{\mathbf{x}}\sin\Omega t + \hat{\mathbf{y}}\cos\Omega t$, respectively. Inserting Eq. (2.1) into Eq. (2.2) and noticing that $\dot{\hat{\rho}} = \Omega\hat{\varphi}$ and $\dot{\hat{\varphi}} = -\Omega\hat{\rho}$, the radial equation of motion reduces to

$$m\left(\omega_0^2\rho - \Omega^2\rho + \ddot{\rho} + \gamma\dot{\rho} - \tau\dddot{\rho} + 3\tau\Omega^2\dot{\rho}\right) = Q\mathbf{E}\cdot\hat{\rho}, \tag{2.4}$$

whereas the azimuthal equation is trivially satisfied by our choice of F^{react}.

The external monochromatic electric field is a plane wave, written as

$$\mathbf{E} = (E_x\hat{\mathbf{x}} + E_y\hat{\mathbf{y}})e^{-\mathrm{i}\omega t} + c.c.,$$

where $c.c.$ stands for complex conjugate. The inhomogeneous solution of Eq. (2.4) corresponding to this incident field is

$$\rho(t) = \frac{Q}{2m}\left(\frac{E_+}{d_+}e^{-\mathrm{i}\omega_+ t} + \frac{E_-}{d_-}e^{-\mathrm{i}\omega_- t} + c.c.\right), \tag{2.5}$$

where

$$\omega_\pm = \omega \pm \Omega,$$
$$E_\pm = E_x \pm \mathrm{i}E_y,$$

and

$$d_\pm = \omega_0^2 - \Omega^2 - \omega_\pm(\omega_\pm + \mathrm{i}\gamma) - \mathrm{i}\tau\omega_\pm(\omega_\pm^2 + 3\Omega^2).$$

Due to the rotational motion, the natural oscillation frequency ω_0 is split into two shifted frequencies $\omega_\pm$ by the effect of a finite Ω.

Electromagnetic torque and mechanical cross-section

The torque M that the light exerts on the particle is directed along $\hat{\mathbf{z}}$ and originates in the reaction force according to $M = -F^{\text{react}}\rho$. Inserting Eqs. (2.3) and (2.5) into this expression and retaining only time-independent terms (*i.e.*, the time-averaged contribution), we find

$$M = \frac{Q^2}{2m}\left[-\left(\gamma\omega_+ + \tau\omega_{++}^3\right)\frac{|E_+|^2}{|d_+|^2} + \left(\gamma\omega_- + \tau\omega_{--}^3\right)\frac{|E_-|^2}{|d_-|^2}\right], \tag{2.6}$$

where $\omega_{++} = \omega + 2\Omega$ and $\omega_{--} = \omega - 2\Omega$. The γ terms in the above equation originate in photon absorption by the particle, whereas the τ terms describe a radiative reaction torque similar to what happens in rotating dipoles.[116] The torque predicted by Eq. (2.6) presents resonant features signaled by the zeros of $d_\pm$. In small absorbing particles, for which the τ radiation terms can be neglected compared to the γ absorption terms, this condition reduces to the ellipses

$$\Omega^2 + (\omega \pm \Omega)^2 = \omega_0^2, \tag{2.7}$$

as is clear in Fig. 2.2(a) for LCP incident light, corresponding to the lower sign in the above expression. The figure actually represents the cross-section towards mechanical work, given by

$$\begin{aligned} \sigma_{\rm mech} &= M\Omega/I \qquad (2.8) \\ &= \frac{\pi Q^2 \Omega}{mc}\left[-\left(\gamma\omega_+ + \tau\omega_{++}^3\right)\frac{|E_+/E|^2}{|d_+|^2} + \left(\gamma\omega_- + \tau\omega_{--}^3\right)\frac{|E_-/E|^2}{|d_-|^2}\right], \end{aligned}$$

where $I = (c/2\pi)|E|^2$ is the external light intensity and $|E|^2 = |E_x|^2 + |E_y|^2$.

A careful analysis of this expression unveils interesting physical features depending on the rotation and illumination frequencies:

- $\omega = \Omega$: For equal light and rotational frequencies, the particle sees a frozen incident field, and the torque is therefore zero [it vanishes along the $\omega = \Omega$ line in Fig. 2.2(a)].
- $\omega > \Omega$: For slower rotation, the torque is positive, pointing to a net transfer of momentum from the light field to the particle.
- $\omega < \Omega$: For faster rotation, both the torque and the mechanical cross-section become negative, even when the light and the particle rotate in the same direction ($\Omega > \omega > 0$). This suggests that the incident light is actually braking the particle by effectively producing stimulated photon emission with contributions proportional to the ohmic and radiative losses (terms in γ and τ, respectively). This process is studied in more detail in Section 2.4.

Absorption, scattering and extinction cross-sections

The particle dissipates energy via light absorption by the material of which it is made. The absorption power is calculated in terms of the dissipative force and yields,

$$P^{abs} = \left(m\gamma\dot{\rho}\hat{\rho}\right)\cdot\dot{\mathbf{r}}$$

Light also exerts a mechanical torque on the particle resulting in a power transfer given by $P^{\rm mech} = M\Omega$. Besides, the total (mechanical plus absorption) work exerted

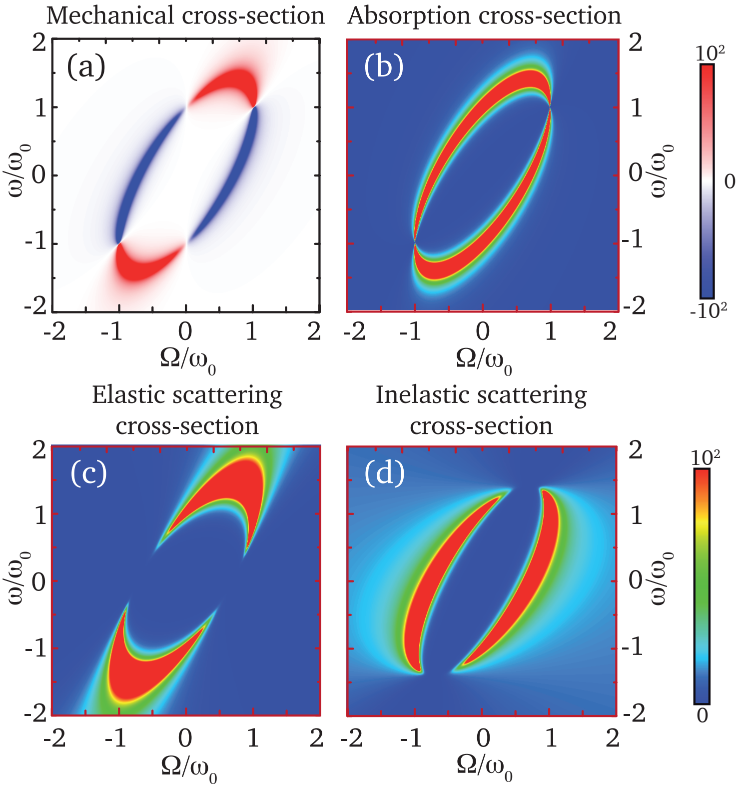

Figure 2.2: Dynamical properties of a rod illuminated by LCP light of frequency ω and rotating at frequency Ω, both normalized to the excitation resonance frequency of the rod ω_0. (a) Mechanical cross-section $M\Omega/I$, where M is the electromagnetic torque and I is the light intensity. (b) Absorption cross-section. (c) Elastic scattering cross-section. (d) Inelastic scattering cross-section (emission at frequency $\omega - 2\Omega$). The particle is described by a rotating harmonic oscillator with intrinsic damping rate $\gamma = 0.1\omega_0$. The color scale is in units of $Q^2\gamma/mc\omega_0^2$ in (a)-(b) and $Q^2\tau/mc$ in (c)-(d), assuming $\gamma \gg \tau\omega_0^2$, and it is saturated at the limits specified in the legend.

by the external light on the particle per unit time has to include the self-field scattered by the particle in order to account for radiation damping, and it is then

$$P = (Q\mathbf{E} + m\tau\dddot{\mathbf{r}})\cdot\dot{\mathbf{r}}.$$

The time-averaged absorption power is found to reduce to

$$\begin{aligned} P^{\mathrm{abs}} &= P - P^{\mathrm{mech}} \\ &= \frac{\gamma Q^2}{2m}\left(\omega_+^2\frac{|E_+|^2}{|d_+|^2} + \omega_-^2\frac{|E_-|^2}{|d_-|^2}\right). \end{aligned}$$

This result can be divided by the external light intensity to obtain the absorption cross-section

$$\sigma_{\mathrm{abs}} = \frac{\pi\gamma Q^2}{mc}\left(\omega_+^2\frac{|E_+/E|^2}{|d_+|^2} + \omega_-^2\frac{|E_-/E|^2}{|d_-|^2}\right). \tag{2.9}$$

It is reassuring to observe that our model predicts the absorption cross-section to be proportional to the intrinsic friction rate γ.

In order to obtain the scattering cross-sections, the dipole moment must be calculated. In the rest frame, the dipole induced in the rotating particle is written as

$$\begin{aligned} \mathbf{p} = \quad Q\rho\hat{\rho} = \quad & \frac{Q^2}{4m}\left\{ \left[\left(\frac{E_+}{d_+} + \frac{E_-}{d_-}\right)e^{-\mathrm{i}\omega t} + \frac{E_+}{d_+}e^{-\mathrm{i}\omega_{++}t} + \frac{E_-}{d_-}e^{-\mathrm{i}\omega_{--}t}\right]\hat{\mathbf{x}} \right. \qquad (2.10) \\ & \left. -\mathrm{i}\left[\left(\frac{E_+}{d_+} - \frac{E_-}{d_-}\right)e^{-\mathrm{i}\omega t} - \frac{E_+}{d_+}e^{-\mathrm{i}\omega_{++}t} + \frac{E_-}{d_-}e^{-\mathrm{i}\omega_{--}t}\right]\hat{\mathbf{y}} + c.c.\right\}. \end{aligned}$$

This expression contains terms of frequencies ω, $\omega + 2\Omega$, and $\omega - 2\Omega$, and allows to obtain the scattering cross-sections associated with these spectral components. In particular, the elastic cross-section, corresponding to the field re-radiated at frequency ω, is

$$\sigma_\omega = \frac{\pi Q^4\omega^4}{3m^2c^4}\left(\frac{|E_+/E|^2}{|d_+|^2} + \frac{|E_-/E|^2}{|d_-|^2}\right), \tag{2.11}$$

as obtained from the time-averaged integral of the far-field Poynting vector (that is, the integral of the squared far-field amplitude) divided by the external field intensity. Interestingly, the rotational motion produces inelastic scattering components at frequencies $\omega \pm 2\Omega$[13] of cross-sections

$$\sigma_{\omega\pm2\Omega} = \frac{\pi Q^4(\omega\pm2\Omega)^4}{3m^2c^4}\frac{|E_\pm/E|^2}{|d_\pm|^2}. \tag{2.12}$$

This is closely related to the rotational frequency shift observed from rotating emitters.[110,113] The quantities $\sigma_{\omega\pm2\Omega}$ describe the effective area of the particles to inelastically scatter the incident light. Numerical results are given in Fig. 2.2 for LCP incident light ($|E_+/E|^2 = 0$ and $|E_-/E|^2 = 2$). The partial cross-sections are also resonant under the condition of Eq. (2.7). In particular, light absorption [Fig. 2.2(b)] produces a positive transfer of intrinsic angular momentum from each absorbed photon to the particle ($\propto \sigma_{\mathrm{abs}} I$). Elastic scattering scattering [Fig. 2.2(c)] dominates the $\Omega \sim \omega$ region and, specifically, at $\omega = \Omega$, the particle does not absorb any radiation at all, only scatters it.

For RCP light, we obtain similar results, with the ellipsoids of M, σ_{abs}, and σ_ω reflected with respect to the $\omega = 0$ axis. For linear polarization ($|E_+/E|^2 = |E_-/E|^2 = 1$), the right and left circularly polarized components of the incident light produce inelastic emission at frequencies $\omega + 2\Omega$ and $\omega - 2\Omega$, respectively, as shown in Fig. 2.3(d)-(e). The torque and absorbed power are the superposition of the contributions originating from these two components. As expected, these terms add up in the absorption but they cancel each other in the torque at $\Omega = 0$.

Finally, the optical theorem allows us to use the ω component of the induced dipole $\mathbf{p}$ [Eq. (2.10)] to obtain the total extinction cross-section

$$\begin{aligned}\sigma_{\mathrm{ext}} = \frac{2\pi\omega}{c|E|^2}\langle \mathbf{p}\cdot\mathbf{E}\rangle = \frac{\pi Q^2\omega}{mc}\Bigg(&\omega_+\left[\gamma + \tau(\omega_+^2 + 3\Omega^2)\right]\frac{|E_+/E|^2}{|d_+|^2} \\ &+\omega_-\left[\gamma + \tau(\omega_-^2 + 3\Omega^2)\right]\frac{|E_-/E|^2}{|d_-|^2}\Bigg),\end{aligned} \tag{2.13}$$

where $\langle ... \rangle$ denotes time average. The total balance of power must be zero, leading to the condition

$$\sigma_{\mathrm{ext}} = \sigma_{\mathrm{mech}} + \sigma_{\mathrm{abs}} + \sigma_\omega + \sigma_{\omega+2\Omega} + \sigma_{\omega-2\Omega}.$$

This is indeed satisfied by Eqs. (2.8), (2.9), (2.11) and (2.12), which corroborates the consistency of the model.

It is important to stress that two remarkable effects emerge at large rotation velocities ($|\Omega| > |\omega|$):

- inelastic emission (at frequency $\omega - \Omega$ for LCP light) becomes a leading process.
- like the mechanical cross-section, the total extinction cross-section can be negative (e.g., for $\Omega > \omega > 0$ and LCP light), thus confirming a net stimulated light emission, whereby mechanical motion is converted into photons (see Section 2.4).

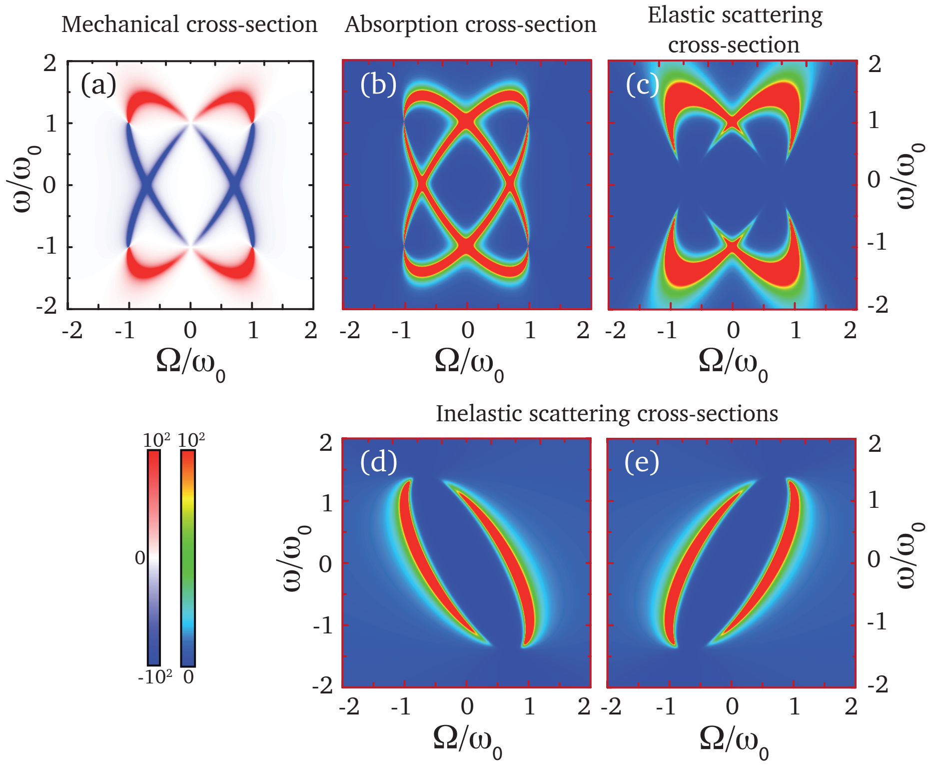

Figure 2.3: Dynamical properties of a rotating rod for linearly polarized incident light in the same conditions as Fig. 2.2. (a) Mechanical cross-section. (b) Absorption cross-section. (c) Elastic scattering cross-section. (d) Inelastic scattering cross-section at frequency $\omega + 2\Omega$. (e) Inelastic scattering cross-section at frequency $\omega - 2\Omega$.

2.3 Connection to actual particles

This section is devoted to establishing a relation between the parameters of the previous model and the properties of actual particles by means of their polarizability. Additionally, we extend the theory in order to be able to deal with isotropic particles.

The parameters Q^2/m, ω_0, and γ can be easily adjusted to fit the polarizability of a particle at rest ($\Omega = 0$). Computing the induced dipole $\mathbf{p}$ [Eq. (2.10)] from our model, we find $\mathbf{p} = \alpha\mathbf{E}$, where

$$\alpha = \frac{Q^2}{m}\frac{1}{\omega_0^2 - \omega(\omega + \mathrm{i}\gamma) - \mathrm{i}\tau\omega^3}, \tag{2.14}$$

is the polarizability. Due to the inclusion of the Abraham-Lorentz force in the equation of motion [Eq. (2.2)], this expression satisfies the property $\mathrm{Im}\{-\alpha^{-1}\} = 2\omega^3/3c^3$ in the absence of internal friction ($\gamma = 0$), as expected from the optical theorem for non-absorbing particles.[47]

This static polarizability permits determining a connection between our simple oscillator model and actual physical parameters of real nanoparticles. For a metallic ellipsoid of volume V described by a Drude dielectric function of bulk plasmon frequency ω_p and damping rate γ, the electrostatic polarizability, corrected for radiative losses,[117] reduces to the above expression with $Q^2/m = \omega_p^2 V/4\pi$ and $\omega_0 = \omega_p\sqrt{L}$, where L is the depolarization factor that depends on the aspect ratio.[48] In particular, for a sphere of radius R, this reduces to $\omega_0 = \omega_p/\sqrt{3}$ and $Q^2/m = \omega_0^2 R^3$.

Now, the question is whether it is possible to extend our formalism in order to deal with isotropic particles. From an analysis based upon Maxwell's stress tensor[3,41] (see Appendix A), at low Ω and within the dipole approximation, we find

$$M/|E|^2 = \mathrm{Im}\{\alpha_{\parallel} + \alpha_{\perp}\} - (4\omega^3/3c^3)\mathrm{Re}\{\alpha_{\parallel}\alpha_{\perp}^*\}$$

for the torque produced by LCP light on a rod under the conditions of Fig. 2.1, where $\alpha_{\parallel}$ and $\alpha_{\perp}$ are the polarizabilities along directions parallel and perpendicular to the rod, respectively. This torque vanishes for non-absorbing spheres in virtue of the optical theorem. In contrast, non-absorbing rods ($\alpha_{\parallel} \neq \alpha_{\perp}$) experience a net torque because the term in ω^3/c^3 cannot compensate the first one. This indicates that the torque acting on small lossy spheres, in which absorption (the γ term) governs $\mathrm{Im}\{-\alpha^{-1}\}$, can be approximated with our formalism as twice the torque acting on a rod, but using the above identification of model parameters. Just to give a better idea of the order of magnitude of the mechanical and absorption cross-sections for a Drude sphere, the units in the color scale of Fig. 2.2(a)-(b) are $Q^2\gamma/mc\omega_0^2 = R^3/(c/\gamma)$, with typical values of $c/\gamma \sim 1\,\mu$m in noble metals.

2.4 Stimulated emission and light amplification

In this section we analyze the physical mechanisms that lead to stimulated emission of radiation by this purely classical system. It is clear from Eq. (2.13) that the extinction cross-section can take negative values when the light and the particle rotate in the same direction (e.g., for $E_+ = 0$ and $\Omega > 0$), provided the particle rotates faster than the light frequency ($\Omega > \omega$). We show in Fig. 2.4 the partial cross-sections of rotating rods in the limits of high, (a), and low, (b), ohmic losses. The negative extinction represents an increase in the amplitude of the incident beam after interaction with the rotating particle. Stimulated emission takes place at $\omega < \Omega$ by transferring mechanical energy from the particle to the incident beam (coherently added photons), similar to what happens in lossy rotating cylinders,[118, 119] but the effect persists even without dissipation.

Actually, stimulated emission by spinning particles is an example of rotational superradiance. This phenomenon was first predicted by Zel'dovich[118] and Starobinskii,[120] who anticipated amplification of light by Kerr black holes, and subsequently extended to the non-rotating case, becoming known as Hawking radiation.[121] The recently reported rotational friction[122] can be understood as the spontaneous-emission counterpart of the stimulated emission under discussion.

Moreover, we speculate with the possibility of constructing a laser in which an incident CP light beam is exponentially building up as it encounters rotating particles along its path. Particle rotation can be sustained by external means (e.g., either mechanically for radio waves or via optical pumping at higher frequencies), so that the system acts as a transducer that converts the externally supplied energy into coherent radiation. This scheme is robust because it is insensitive to finite distributions of particle size and rotation velocity, as long as the latter exceeds the light frequency. In a more sophisticated arrangement, we envision an electromagnetic cavity containing such an amplifying medium, in which the radiation is making several passes before leaving the cavity (e.g., in a parallel mirror configuration). The seed in this system can be provided either by external illumination or by intrinsic spontaneous emission within the system.[123]

Incidentally, lasing and light amplification effects can be potentially achievable within various windows of the electromagnetic spectrum. For example, one can rely on mechanically or magnetically induced motion up to radio frequencies lower than 1 MHz. Light-driven rotation of nanoparticles levitated in vacuum could be used for higher frequencies in the GHz regime before the particles break apart. Molecular rotators could also be employed up to THz frequencies, in a process resembling the rotational Raman effect. These regimes can be accompanied by intrinsic resonance frequencies of the rotating bodies relying on LC circuits at low frequencies or physically equiva-

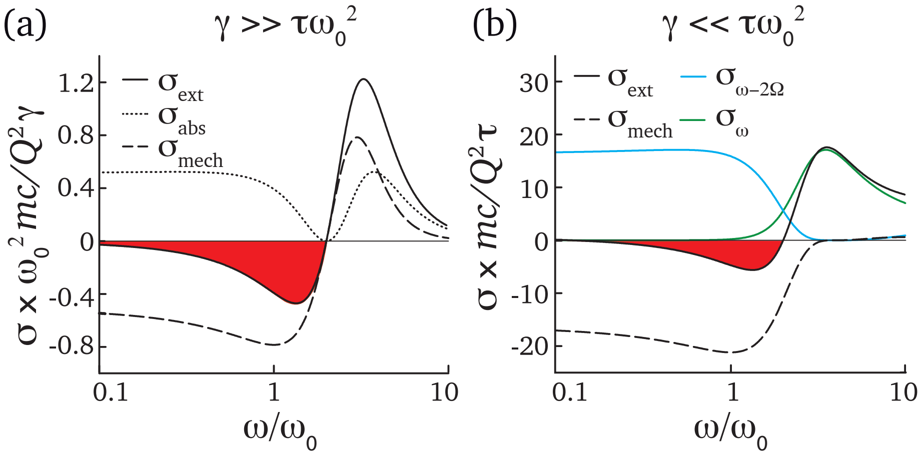

Figure 2.4: Stimulated light emission in rotating particles. The plots show the spectral dependence of the partial cross-sections for (a) dissipative ($\gamma \gg \tau\omega_0^2$) and (b) non-dissipative ($\gamma \ll \tau\omega_0^2$) rods rotating with frequency $\Omega = 2\omega_0$. The shaded areas for negative extinction ($\sigma_{\text{ext}} < 0$) give the excess of photons added to the incident beam as a result of the interaction with the particle.

lent excitations such as Mie resonances, plasmons, and optical phonons.

Additionally, dust clouds in cosmic environments provide a plausible scenario for electromagnetic amplification since they are formed by microparticles that are exposed to the effect of neighboring light sources (e.g., stars and galaxies), which are circularly polarized in some cases. This illumination acts over enormous periods of time (millions of years), thus potentially inducing large rotation in the particles in the range of GHz before they are destroyed by centrifugal explosion. Therefore, amplification can be expected up to GHz frequencies, compatible with the low-end of the cosmic microwave background.

2.5 Particle heating and acceleration time

Controlling a particle's speed and handedness of rotation in a simple and accurate way opens up a whole range of applications that go from generating light at shifted frequencies $\omega \pm 2\Omega$ to measuring the torsional properties of biological molecules by attaching them to a spinning body.[124] However, we first need to analyze how large are the light intensities required for acquiring high rotational frequencies and predict

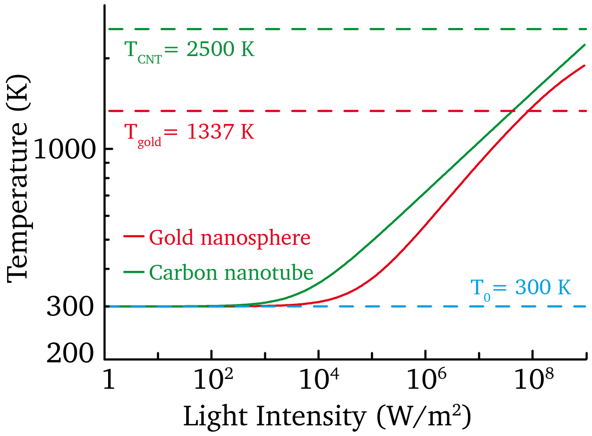

Figure 2.5: Equilibrium temperature of a 20-nm gold sphere and a 6 × 6 10-nm-long single-wall carbon nanotube as a function of incident CP light intensity. The particles are rotating in vacuum at an external temperature $T_0 = 300\,$K. The gold and carbon melting points are indicated by dashed lines. The light frequency is $\omega = 2\pi \times 10^{14}\,$Hz (wavelength $\sim 3\,\mu$m).

whether a given particle can stand them without melting.

Particle heating

For constant incident light intensity, light absorption leads to heating of the particle until it reaches an equilibrium temperature $T_{\rm eq}$ above the temperature of the surrounding vacuum T_0. This equilibrium is established when the absorbed power $\sigma_{\rm abs} I$ equals the radiative cooling rate $P^{\rm rad}$. The radiated power is calculated by means of the fluctuation-dissipation theorem,[122] and yields

$$P^{rad} = \frac{4\hbar}{3\pi c^3} \int_{-\infty}^{\infty} d\omega\, \omega^4\, {\rm Im}\{\alpha(\omega_-)\}[n_{eq}(\omega_-) - n_0(\omega)], \qquad (2.15)$$

where n_{eq} and n_0 are the Bose-Einstein distributions at temperature T_{eq} and T_0, respectively. In the Drude approximation for a metal sphere and neglecting the effect of Ω, which only enters at large velocities, we have $P^{\rm rad} \propto T_{\rm eq}^6 - T_0^6$, which leads to

$$T_{\rm eq}^6 = T_0^6 + C\sigma_{\rm abs} I,$$

where C is a constant that depends on the material properties. This is represented in Fig. 2.5 for a 10-nm carbon nanotube (green curve) for which the polarizability has been obtained in the discrete-dipole approximation.[68] There are two different regimes in the dependence of T_{eq} on light intensity: at low I, the particle is nearly at the vacuum temperature, but when the intensity increases, the particle heats up, asymptotically approaching a $I^{1/6}$ power law. A similar behavior is observed for a gold nanosphere (red curve), characterized by a tabulated dielectric function,[42, 122] and incorporating the effect of magnetic polarization to both the absorption and emission processes [for the latter, we add an identical term to Eq. (2.15) but substituting the electric polarizability by the magnetic one].

Acceleration time

We now compute the required time to accelerate a particle up to a given rotational frequency. As shown by Eq. (2.6), the sign of the torque depends on the polarization of the incoming light and it is therefore possible to either speed up (LCP light) or slow down (RCP light) a spinning body just by changing the handedness of the illuminating field. The acceleration time is calculated from Newton's second law, $M = \mathfrak{I}\dot{\Omega}$, where $\mathfrak{I}$ is the moment of inertia.

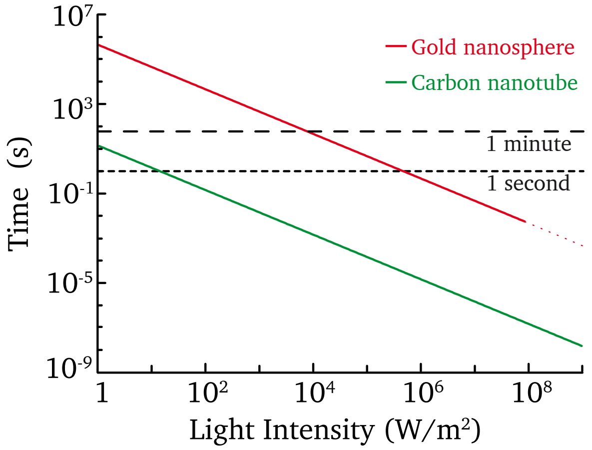

Figure 2.6: Time needed to accelerate a 20-nm gold sphere and a 6 × 6 10-nm-long single-wall carbon nanotube to a rotational velocity $\Omega = 1\,\mathrm{MHz}$ as a function of incident CP light intensity. The gold nanosphere melts at high intensities represented by the dotted line. The light frequency is $\omega = 2\pi \times 10^{14}\,\mathrm{Hz}$ (wavelength $\sim 3\,\mu$m), and the external temperature is $T_0 = 300\,\mathrm{K}$.

The time needed to accelerate a carbon nanotube and a gold nanosphere to 1 MHz is represented in Fig. 2.6 as a function of LCP light intensity, as calculated with the torque of Eq. (2.6). Since the carbon nanotube is lighter and less conducting than the gold nanoparticle, it is more rapidly accelerated. At the same time, its equilibrium temperature is higher, thus becoming a very good candidate for high-speed centrifugal experiments. The time scales approximately as $\propto R^2\omega_0^2\Omega/\gamma\omega I$ under the condition $\gamma\omega \ll \omega_0^2$, and it plunges well under 0.01 s for light intensities below the melting threshold. This suggests the possibility of achieving extreme rotation velocities in optically trapped nanoparticles, and eventually producing centrifugal explosion, thus introducing an unprecedented physical scenario (this should happen close to the point at which the centrifugal energy reaches the surface-tension energy, which in a 20-nm liquid gold particle occurs at $\Omega \sim 3$GHz).

2.6 Conclusions

In the first part of this chapter, we have presented a self-consistent oscillator model that captures the dipolar optical response of rotating rod-like particles. We have obtained analytical expressions for crucial dynamical properties such as the torque, the absorption, and scattering cross-sections as a function of the incoming light frequency, that emerges in a non-trivial way in the equations. We have predicted exotic phenomena such as strong inelastic scattering, at frequencies shifted by twice the rotation frequency, depending on the light polarization. In the following section, we have made a connection between the parameters of this toy-model and the optical properties of real particles. We have demonstrated that our theory adequately describes the behavior of absorbing as well as non-absorbing particles due to the inclusion of radiation reaction through the Abraham-Lorentz force, yielding a radiatively correct expression for the polarizability. Besides, it can be extended to deal with isotropic absorbing particles.

Most notably, we have explored the possibility of realizing a laser running on a classical system by exploiting our prediction of light amplification by particles rotating faster than the light frequency. There are several avenues towards potentially practical implementations of these systems, such as, for example, (1) a diluted gas of linear molecules driven to THz rotational frequencies by CP light and acting as the active medium of a laser operating in that demanded frequency range; (2) an extension of these ideas to acoustic lasing based on a similar classical interaction with subwavelength particles rotating faster than the sound frequency; (3) microwave waveguide setups such as those used to monitor rotational frequency shifts;[102] (4) dust clouds in cosmic environments exposed to polarized light, in which radio wave amplification might be taking place.

In the last part of the chapter, we have demonstrated the feasibility of achieving very high rotational frequencies without melting the particles. This could be a potential mechanism for particle accelerators by liberating the rotational energy as translational energy in the emitted byproducts. Also, light-induced torques raise the possibility of optically driven nano-machines. For example, the induced rotation of particles in a fluid can be used to control turbulence flow and transport.

L' univers est un ensemble dissymétrique, et je suis persuadé que la vie, telle qu'elle se manifeste à nous, est fonction de la dissymétrie de l'univers ou des conséquences qu'elle entraîne.

Louis Pasteur

3

Chiral interactions between light and matter

Motivated by the chiral architectures of biological molecules, we study plasmonic tetramers composed of identical gold nanospheres assembled using DNA structural technology. [1] These clusters exhibit strong circular dichroism in the visible regime. We compare experimental and theoretical results, which are in good agreement, and analyze the crucial role of plasmonic coupling between particles in the dichroic signal.

---

[1] All measurements presented throughout this chapter were performed by the groups of Prof. Laura Na Liu in the Max-Planck-Institute for Intelligent Systems (Stuttgart, Germany) and Prof. Baoquan Ding in the National Center for Nanoscience and Technology (Beijing, China).

3.1 Introduction

Many biologically active structures are chiral and, actually, different enantiomers may display dramatically divergent behaviors. For instance, depending on their handedness, drugs made of chiral molecules might have strikingly distinct pharmacological effects, as was painfully manifested during the thalidomide crisis.[125] Evidently, optical chirality occurs at the region where the molecules present resonant features. In particular, biomolecules exhibit CD response mainly in the UV, which hinders their potential applicability. By designing artificial plasmonic molecules it is possible to obtain a strong CD signal in the visible and infrared regimes,[126,127] thus paving the way towards the generation of chirality-sensitive optoelectronic devices or biosensors.[128] Many three-dimensional plasmonic chiral structures have been created by top-down[129–132] approaches, such as by direct laser writing[129] or electron-beam lithography.[130] Inspired by biomolecules, several geometries and configurations have been explored: gold spirals, twisted gammadions, and split-ring resonators that bear resemblance to DNA helices.

However, these techniques are not suitable for mass production of chiral clusters, and the synthesized structures usually reside on two-dimensional substrates. This is why the bottom-up approach[33,133] has arisen as a disruptive innovation in the fabrication field, thanks to the efforts of biochemists to generate 3D geometries of metal nanoparticles. For instance, peptide amphiphile supramolecules have been employed as scaffolds for building chiral gold nanostructures.[134] Besides, helical chains formed by metallic spheres have been generated using DNA templates.[33,135] Moreover, α-helices have served as well as inspiration to design smart artificial plasmonic nanostructures. In this molecule, four different substituents (COOH, R, NH_2, and H) are bonded to a tetravalent carbon atom, which forms a stereogenic center. This tetrahedral molecule imprints a “twist” character to their electronic clouds and generates a chiral response in the interaction with CP light. In a cutting edge experiment, Mastroianni *et al.* attempted to build a plasmonic analogue of a natural chiral molecule.[136] They generated a tetrahedron by assembling four different gold nanoparticles monofunctionalized with single strands of DNA and taking advantage of programmable DNA hybridization. However, the resulting clusters did not exhibit any dichroic response due to both the floppiness of single-stranded DNA and the weak plasmonic coupling between the nanoparticles.

In this chapter, we demonstrate that circular dichroism can be generated with artificial plasmonic chiral nanostructures. In the first part, the experimental methods are reviewed. We show how four identical gold nanospheres are organized at their designated binding sites on a rigid DNA origami template[137–141] with nanometer spatial accuracy. In the following section, we provide details on the calculation of both ligth extinction and CD spectra. We discuss the results obtained by using a dipole-dipole interaction model with those calculated considering the full multipolar response of the cluster. We then compare the theoretical predictions with the experimental data, finding very good agreement. Finally, the role of plasmonic coupling is studied and other feasible structures are proposed.

3.2 Experimental methods

The experimental scheme is illustrated in Figure 3.1. First, the rectangular DNA origami is formed by annealing the M13 scaffold strand, capture strands, and helper strands in a ratio of 1:5:10 from 90 °C to room temperature. The product is purified with a filter device to remove the extra helper and capture stands. The dimensions of the origami are $\sim 90 \times 60 \times 2$ nm. DNA capture strands (shown in different colors) are placed at four precise locations and are carefully engineered to contain specific bases sequences. Three binding sites are designed on the top surface of the DNA template and the fourth one is located on the opposite side, in order to accurately organize four gold nanoparticles.

Each of the gold nanoparticles are assembled to the DNA origami by identical-sequence capture strands located at each binding site. In order to avoid nonspecific binding, the sequences of the capture strands corresponding to different binding spots are all distinct from each other. Then, the purified DNA origami and the nanospheres functionalized with corresponding complementary DNA strands are mixed and annealed from 43°C to 23°C for 24 hours. Ensuing DNA hybridization, the nanoparticles are assembled on the DNA template forming chiral left- and right-handed tetramers. As a control experiment, an achiral structure (consisting of only three nanospheres) is also built.

Afterwards, the annealed product is analyzed by agarose gel electrophoresis, as displayed in Fig. 3.2(a). Lane 1 corresponds to the M13 strand and lane 2 contains the rectangular DNA origami. Lane 3 shows the DNA modified gold nanoparticles. Lanes 4 and 5 contain the left- and right-handed clusters, respectively, and lane 6 corresponds to the achiral structures. White-dashed lines highlight bands of the target structures. These bands are subsequently sliced and extracted by electroelution with dialysis tubing membranes.

Figure 3.2 shows TEM images of left-(b) and right-handed (c) clusters, respectively. Stereographic TEM imaging is performed at different cluster orientations to obtain geometrical information of the structures. The schematic plots in the insets, constructed by taking into account the tilting angle, clearly show their chiral character.

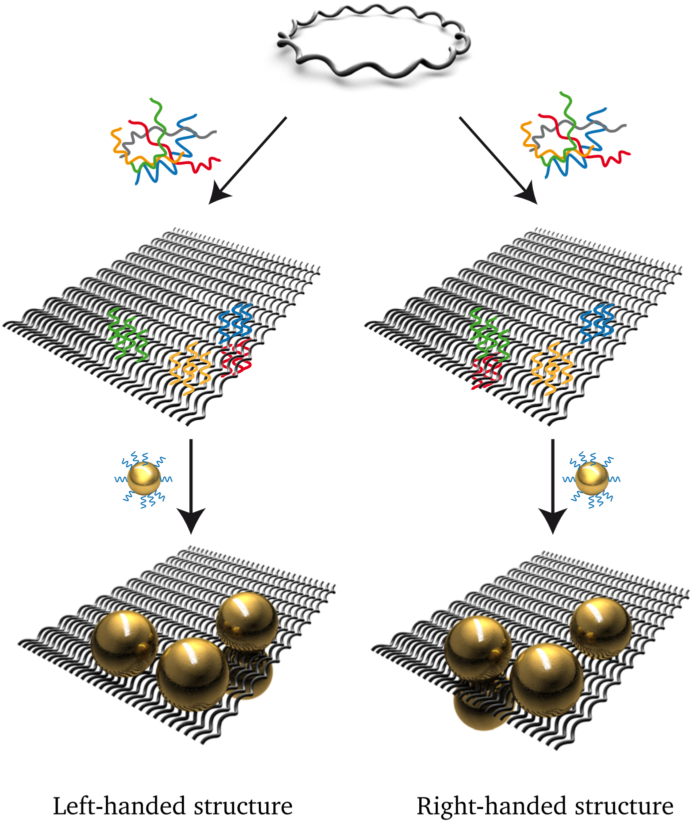

Figure 3.1: Schematic illustration of the experiment. A long scaffold single DNA strand (M13) hybridizes with helper and capture strands to form a rectangular DNA origami template with well-defined binding sites. The capture strands are extended from four binding sites, three on the top surface and one on the bottom surface of the origami template. The binding sites with different DNA sequences are illustrated using red, yellow, green, and blue colors. Gold nanoparticles functionalized with corresponding complementary DNA strands are assembled at the predesignated locations on the origami template through DNA hybridization, forming left- and right-handed structures.

Finally, in order to characterize the chiral response of the clusters, extinction and CD measurements are carried out with a quartz cuvette (0.5 cm path length) using a J-810 Circular Dichroism Spectrometer. All plasmonic structures in this study are dispersed in a TAE/Mg^{2+} water-based buffer during optical measurements.

3.3 Theory and modeling

In order to compare the theoretical results with the experimental data, we need to calculate the extinction cross-sections for left- and right-circularly polarized light, from which we obtain the CD spectra. Since the orientations of the chiral assemblies in the solution are totally random, we carry out an average over the angles of light incidence (or equivalently, over all possible assembly orientations for fixed light incidence). The dichroic signal (in millidegrees) is

$$\mathrm{CD\ (mdeg)} = \frac{45N_A}{\pi}\langle\sigma_L - \sigma_R\rangle_\Omega(\mathrm{cm}^2)\cdot c(\mathrm{M})\cdot l(\mathrm{cm}).$$

In the above expression, $c = 0.3$ nM is the chiral assembly concentration, $l = 0.5$ cm is the optical path length, σ_L and σ_R are the extinction cross-sections for the left and right circularly polarized light, respectively, and $\langle\ldots\rangle_\Omega$ denotes the average over the solid angle of the tetramer orientations. This average is approximated by

$$\langle\sigma_{L,R}\rangle_\Omega \simeq \frac{1}{4\pi}\frac{2\pi^2}{N_\theta N_\varphi}\sum_{i,j}\sigma_{L,R}(\theta_i,\varphi_j)\sin\theta_i,$$

where the polar and azimuthal angles are in the ranges of $\theta_i \in [0,\pi)$ and $\varphi_j \in [0,2\pi)$ in N_θ and N_φ steps, respectively. In what follows, we present two different ways of calculating the extinction cross-section: a tutorial semi-analytical dipole-dipole interaction calculation and a multipolar, fully numerical one.

3.3.1 Dipole-dipole interaction

We first carry out a semi-analytical calculation in which the particles are considered to behave as electric dipoles. The extinction of light by a particle cluster is just the sum of the extinction produced by all the particles conforming it:

$$\sigma = \sum_j \sigma_j,$$

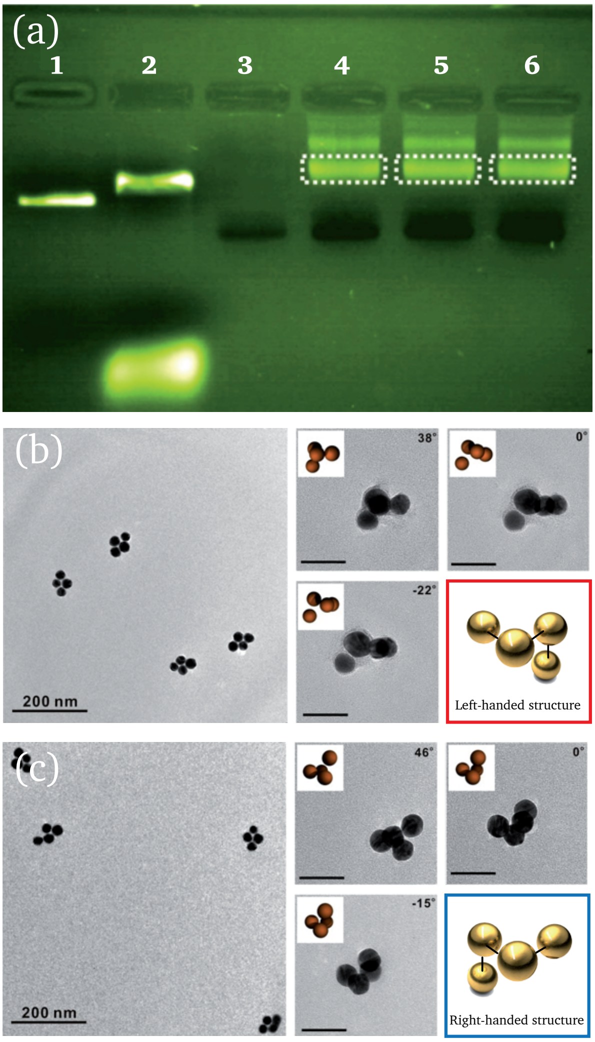

Figure 3.2: Agarose gel image and TEM images of the left- and right-handed structures. (a) Ethidium bromide-stained agarose gel image of the products at different experimental stages. Lane 1: M13. Lane 2: rectangular DNA origami. Lane 3: DNA-modified gold nanoparticles. Lane 4: left-handed clusters. Lane 5: right-handed clusters. Lane 6: achiral clusters. The target products are contained in the bands that are highlighted using white dashed lines. (b,c) Left: Overview TEM image of several left- (b) and right-handed (c) structures. Right: TEM images of an individual left-handed structure at different titling angles, which are well matched by the schematic illustrations shown as insets. The scale bars are 50 nm.

where σ_j is the extinction cross-section of particle j. By the optical theorem, it yields

$$\sigma_j = \frac{4\pi k}{\sqrt{\epsilon_h}\,|\mathbf{E}_j^{\text{ext}}|^2}\,\text{Im}\left\{\mathbf{p}_j \cdot (\mathbf{E}_j^{\text{ext}})^*\right\},$$

where ϵ_h is the permittivity of the host medium, $k = \omega/c$ is the light wave-vector, and $\mathbf{E}_j^{\text{ext}} = \mathbf{E}^{\text{ext}}(\mathbf{r}_j, \omega)$ is the external electric field at the position of the particle j. The particles are described as self-consistent dipoles which read

$$\mathbf{p}_j = \alpha\left(\mathbf{E}_j^{\text{ext}} + \frac{1}{\epsilon_h}\sum_{j' \neq j} \mathcal{G}^0_{jj'} \cdot \mathbf{p}_{j'}\right), \tag{3.1}$$

where α is the polarizability,

$$\mathcal{G}^0_{jj'} = \mathcal{G}^0(\mathbf{r}_j - \mathbf{r}_{j'}, \omega) = \left(q^2\mathbb{1} + \nabla_j \otimes \nabla_j\right)\frac{e^{\text{i}q|\mathbf{r}_j - \mathbf{r}_{j'}|}}{|\mathbf{r}_j - \mathbf{r}_{j'}|}$$

is the Green tensor of the host medium, and $q = \sqrt{\epsilon_h}k$. The sum in Eq. (3.1) stems from the field produced at $\mathbf{r}_j$ by dipoles other than j. In matrix notation, with matrix indices running over the three Cartesian directions for each and all of the particles j, Eq. (3.1) can be recast as

$$\mathbf{p} = \frac{\mathbf{1}}{\alpha^{-1} - \mathcal{G}^0/\epsilon_h} \cdot \mathbf{E}^{\text{ext}}.$$

Finally, the extinction cross-section reads

$$\sigma = \frac{4\pi k}{\sqrt{\epsilon_h}\,|\mathbf{E}^{\text{ext}}|^2}\text{Im}\left\{(\mathbf{E}^{\text{ext}})^* \cdot \frac{\mathbf{1}}{\alpha^{-1} - \mathcal{G}^0/\epsilon_h} \cdot \mathbf{E}^{\text{ext}}\right\}. \tag{3.2}$$

As we already showed in Section 1.3, the polarizability of spheres admits a closed-form expression readily available from Mie scattering theory,[45,47]

$$\alpha = \frac{3}{2}\frac{1}{\sqrt{\epsilon_h}k^3}t_1^E, \tag{3.3}$$

in terms of the corresponding dipolar Mie coefficients, which in a medium of permittivity ϵ_h read

$$t_1^E = \frac{-\epsilon_h j_1(\rho_h)\left[\rho_m j_1(\rho_m)\right]' + \epsilon_m j_1(\rho_m)\left[\rho_h j_1(\rho_h)\right]'}{\epsilon_h h_1^{(+)}(\rho_h)\left[\rho_m j_1(\rho_m)\right]' - \epsilon_m j_1(\rho_m)\left[\rho_h h_1^{(+)}(\rho_h)\right]'}, \tag{3.4}$$

where ϵ_m is the metal dielectric function of the particle, $\rho_m = \sqrt{\epsilon_m}kR$, $\rho_h = \sqrt{\epsilon_h}kR$, R is the radius, $h_1^{(+)} = ih_1^{(1)}$, and the primes indicate differentiation of the spherical Bessel and Hankel functions j_1 and $h_1^{(+)}$ with respect to their arguments.

For the calculations, the dielectric function of gold (ϵ_m) is taken from tabulated optical data.[42] The chiral assembly is in water ($\epsilon_h = 1.77$), and we ignore the presence of DNA in the solution. This is a safe assumption for several reasons: DNA occupies a small volume, its dielectric constant is non-resonant (it absorbs light in the UV region[28]), and has small contrast with water.

3.3.2 Multiple scattering multipolar calculation

In the numerical simulation, rather than relying on just dipoles, we use a full multipolar expansion of the electromagnetic field around each nanoparticle in the tetramer. The self-consistent interaction among these multipoles allows us to calculate the extinction cross-sections for left- and right-circularly polarized light, respectively, from which we obtain the CD spectra. A multiple elastic scattering of multipolar expansions (MESME) code is used for this purpose.[142, 143] Within this formalism, the incoming electromagnetic field is first decomposed into multipoles around each nanoparticle. Then, the field is obtained in terms of the scattering matrices of the bodies and finally, multiple scattering is performed until convergence is reached.

Figure 3.3(a) compares the results for LCP light extinction and dichroism (see inset) for the left-handed cluster for both dipole-dipole and full calculations. In order to perform the angular average, we have chosen $N_\theta = 50$ and $N_\varphi = 100$, covering 5,000 different orientations.

The dipolar approximation is qualitatively valid when the ratio between the spheres separation and their radii is larger than $\sim$3.[144, 145] Although the exact diameter and separation of the nanoparticles are not known, it is possible to estimate their average values by comparing the calculated results to the extinction cross-section spectra of the chiral assemblies and the dip-peak positions in the CD spectra obtained from the experiment. The experimental results are consistent with the calculated results when 20-nm nanoparticles and a 8-nm inter-particle separation are employed in MESME calculations. Larger particles lead to a spectral redshift relative to the experimental data in both the extinction cross-section and the CD spectra. Although the ratio between the separation distance and the radius is slightly smaller (2.8) than the validity region of the dipole-dipole model, the results for the extinction cross-section are in very good agreement with those obtained taking into account the full multipolar response. However, despite the small size of the spheres compared to the light wavelength, the high-order multipoles play an important role to fully describe

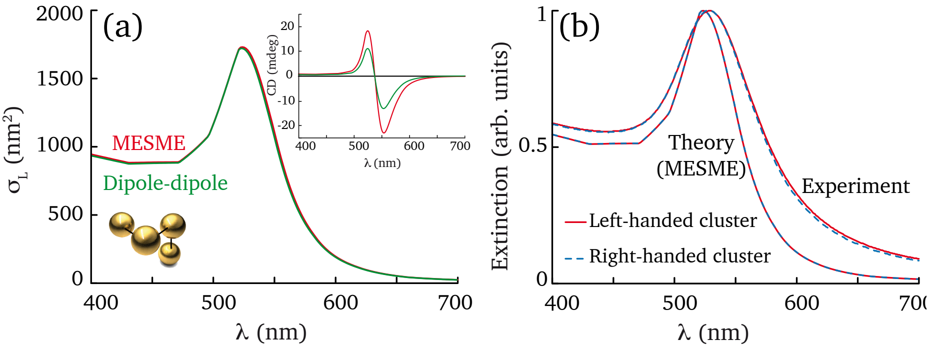

Figure 3.3: (a) Theoretical LCP light extinction cross-section and CD spectra (see inset) for the left-handed cluster, for multipolar (MESME) and dipolar calculations [following Eq. (3.2)]. (b) Measured and calculated LCP light extinction for the tetramers. For the calculations, the structure is considered to consist of 20-nm gold nanospheres with a surface-to-surface separation of 8 nm.

the dichroic spectrum [see inset of 3.3(b)]. Therefore, all the following calculations are performed using MESME.

3.4 Agreement between experimental and theoretical results

Experimental UV-visible extinction spectra of the left- and right-handed chiral assemblies are shown by red and (dashed) blue lines in Fig. 3.3(b), respectively. The two spectra nearly coincide with each other. The figure also displays the theoretical curves obtained using MESME, for 20-nm spheres with 8-nm interparticle distance. The calculated resonance frequency matches that obtained experimentally. Nevertheless, the experimental curve is broader than the theoretical one due to the probably large dispersions in both the size and inter-particle separation distances in the tetramers of the experiment, which are not considered in the calculations.

Figure 3.4 shows the measured (a) and theoretical (b) CD spectra for left- and right-handed assemblies (red and blue lines, respectively). The left-handed cluster displays a characteristic bisignate peak-dip dichroic profile. The spectrum flips when the handedness is reversed, presenting a bisignate dip-peak CD signal for right-handed samples. Incidentally, the spectral response associated with chiral plasmonic tetramers

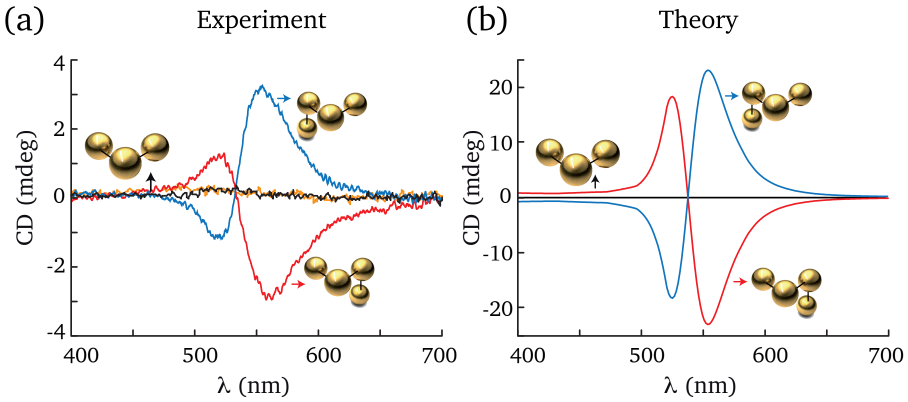

Figure 3.4: Measured (a) and calculated (b) CD spectra of the achiral, right-, and left-handed structures. The orange line in (a) represents the CD signal of DNA-functionalized spheres. For the calculations, the structure is regarded as a 20-nm gold nanoparticle assembly with a particle spacing of 8 nm.

generated by electron-beam lithography is remarkably different, as these structures stand still on the substrate and, therefore, exhibit preferential response to circularly polarized light upon forward or backward illumination conditions.[132] In contrast, our chiral assemblies are oriented along all possible directions with respect to the incident light as they freely move in an aqueous solution. As expected, the trimer does not exhibit any CD response, as shown by the black line in Fig. 3.4. Since trimer structures have an inversion center, they are not chiral. In fact, four is the minimum number of identical spherical nanoparticles that allows obtaining 3D chirality.[32, 146, 147]

It shall be emphasized that the chiral response of the clusters is due to the strong plasmonic resonant coupling between the metallic nanoparticles in each individual assembly. As was already stated in Section 1.2, chiral molecules are described by non-orthogonal electric and magnetic dipoles, resulting in a helical distribution of their charges. In the case of tetramers, it is their 3D geometrical configuration the one responsible for their dichroic behavior, as it generates a "corkscrew” character on the plasmon modes, introducing a twist of specific handedness into the propagation of light. In fact, although their CD spectra is qualitatively explained by assuming that each sphere behaves as an electric dipole, the collective response of all of them can be understood in terms of the appearance of global, effective, non-orthogonal electric and magnetic dipoles that characterize the assembly as a whole.

Theory agrees qualitatively well with experiment, although the measured CD amplitudes are smaller than those predicted by the calculations. The main reason for this discrepancy lies in the assessment of the concentration of the chiral plasmonic tetramers, which cannot be directly determined from the experiment. The actual concentration is lower than the nominal one ($c = 0.3$ nM), as indicated by the fact that the chiral assemblies were only part of the final products [see the bands in lanes 4 and 5 of Fig. 3.2(a)]. Additionally, the CD response is very sensitive to imperfections of the samples, such as the slight size and separation variations in the individual assemblies, which contribute to the lower amplitude and broader profile of the measured CD signal.

In order to demonstrate that the circular dichroism here reported is mostly coming from the chiral arrangement of the tetramers, we have to rule out other possible origin – the DNA's own dichroic response. Surprisingly, it has been demonstrated that natural chiral molecules attached to nonchiral plasmonic particles may induce CD at optical wavelengths.[146, 148, 149] As a control experiment, the CD spectrum of DNA-modified individual gold nanospheres is measured [see orange curve in Fig. 3.4]. The signal is negligible within the wavelength range of interest and, therefore, we can positively claim that the dichroic response observed in our experiments is due to the plasmonic resonant coupling of the four gold nanoparticles arranged in a 3D chiral tetramer.

3.5 The role of plasmonic coupling

In this section, we analyze the importance of the plasmonic near-field coupling on the dichroic signal and discuss possible sources that explain the larger CD obtained in the calculations with respect to the measured data.

As shown in Fig. 3.5, decreasing the particle size and increasing the inter-particle distance can lead to a dramatic reduction of the CD signal because of the weakened interaction among the nanoparticles. For a chiral assembly formed by 20-nm spheres separated by 8 nm, the rotation of the field vector along the assembly at the wavelength of maximum dichroism is $\sim 30^o$. When the field propagates along larger assemblies, the degree of rotation increases, and therefore the CD is also more pronounced.

Furthermore, other important factor that contributes to explain the smaller experimental signal with respect to the theoretical prediction is the uncertainty in the relative positions of the nanoparticles in the individual chiral assemblies. As shown by Kuzyk *et al.*,[33] the CD bisignate pattern is robust against this source of disorder in a helical configuration, but it might have a more substantial effect in tetramers

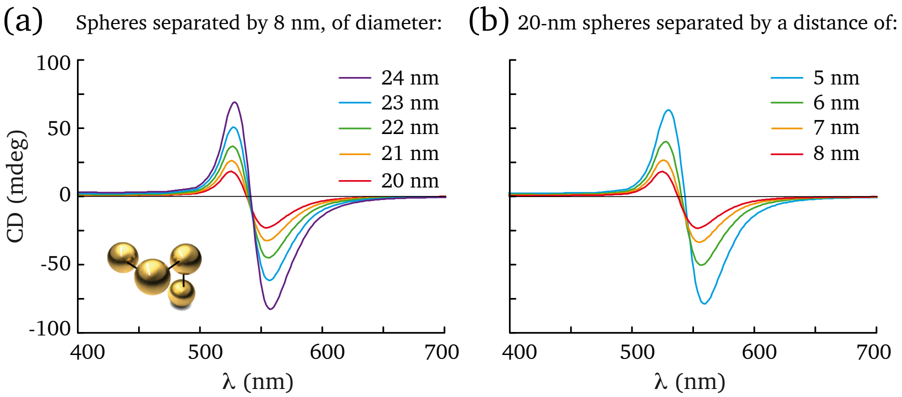

Figure 3.5: Influence of the size and separation of the nanoparticles on the CD spectra. The calculations are carried out for the left-handed tetramer that is shown in the inset. (a) CD for different nanospheres' diameters and a fixed separation of 8 nm. (b) CD for different separation distances and a fixed nanospheres' diameter of 20 nm.

with a smaller number of particles (*i.e.*, uncertainties in the position of any of the particles are more relevant to the response of the entire cluster).

Under illumination with different light polarizations or incident angles, the plasmonic modes of the chiral assembly display different excitation intensities. This effect is analyzed in Fig. 3.6. The red curve represents the difference between the extinction cross-sections for left- and right-circularly polarized light averaged over all assembly orientations, as discussed above. The green and orange curves correspond to the incidence directions indicated in the inset. Interestingly, it is also possible to obtain an angular averaged curve within $< 1\%$ error relative to the red curve just by averaging the six spectra obtained from the six different incidence configurations, which are along three orthogonal directions, as shown in the inset.[147] Obviously, the magnitude of the CD signal for specific directions of incidence is larger than the average. Also, sign changes of the spectrum signal may occur, due to the angle-dependent relative excitation amplitudes of the different modes. The orientation average washes out these features, giving rise to the characteristic bisignated signal.

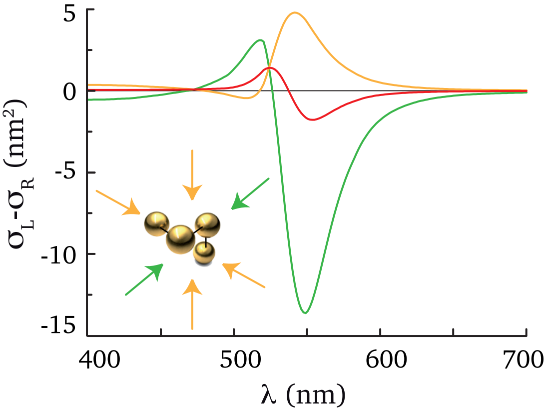

Figure 3.6: Influence of the incidence direction on the CD. The orange and green curves correspond to the results under the specific light incidence directions shown by the arrows in the inset. The red curve is the average over the spectra obtained from the six different incidence configurations. For the calculations, the structure is considered to be an assembly of 20-nm gold nanoparticles with a particle spacing of 8 nm.

3.6 Other systems

Bottom-up techniques based on DNA origami structural technology might play a major role in the assembly of smart, 3D chiral plasmonic nanostructures. For the gold tetramers here presented, the difference between the extinction cross-sections of the left and right circularly polarized light is actually very small. The normalized dichroism at the maximum of the CD signal is

$$\frac{\langle \sigma_L - \sigma_R \rangle_\Omega}{\langle \sigma_L + \sigma_R \rangle_\Omega} \simeq 0.1\% \tag{3.5}$$

Luckily, such a small difference produces experimentally resolvable dichroism. Nevertheless, one may resort to other configurations in order to increase this ratio. One approach would be to use silver instead of gold as the nanoparticles' material. The lower losses of this metal, and subsequent stronger near-field coupling, would yield a much higher signal than that of gold. Besides, the employment of different metals would extend the spectral range of CD response to other energies (for instance, silver clusters would display CD at higher energies than those here reported).

Another exciting possibility consists in modifying the geometry of the building blocks of the cluster. It has been demonstrated that larger structures such as gold nanorods[150] provide a very high near-field enhancement that, in turn, generates strong CD signals. Furthermore, reconfigurable plasmonic structures based on gold nanospheres[151] and nanorods[152] have been designed via DNA-controlled conformational changes. Moreover, exotic scenarios might arise from the interplay between the chirality due to the geometrical arrangement of the particles and the DNA's own dichroic response.[153]

Very recently, 3D DNA polyhedra of sizes of one-tenth of a bacterium have been generated.[154] This promising advances in DNA self-assembly techniques allows one to speculate with building increasingly complex chiral metamolecules.

3.7 Conclusions

In this chapter, we have dealt with plasmonic tetramers that successfully resemble molecular models. These chiral clusters display strong CD response in the visible regime due to plasmonic resonant coupling.

In the first part of the chapter, we have reviewed the experimental methods. When compared with top-down techniques, structural DNA technology provides great flexibility for engineering 3D plasmonic nanostructures. Additionally, this method is scalable and can be used for mass production of chiral clusters. The following section has been devoted to the theoretical calculation of the extinction cross-section of light by these nanostructures. Two different approaches have been presented: one that relies in a semi-analytical dipole-dipole interaction calculation and a numerical simulation that considers the full multipolar response of the whole cluster. We have then compared the numerical results with the data obtained from the experiments and found a very good agreement. Finally, we have analyzed the role of the plasmonic coupling in the CD signal and suggested other chiral systems with interesting properties.

Chiral sensing emerges as the most appealing application of these structures. For instance, due to the high sensitivity of the CD signal to the spatial configuration, a structural modification resulting from the bending of the strands that are used to link the gold nanoparticles to the DNA origami platform could be automatically detected, even in real time.

From a more general point of view, we envision large-scale production of smart artificial plasmonic nanostructures based on concepts and configurations translated from biology and molecular chemistry. It would be possible to synthesize chiral metamolecules with a growing degree of architectural complexity. Due to the high spatial accuracy provided by the specifity of the DNA, it would be possible to build nanostructures that mimic complex natural biological systems, but with highly tunable spectral features.

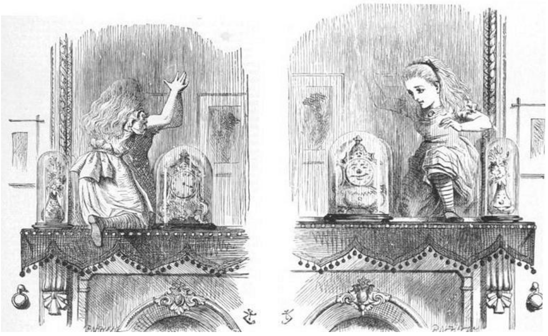

Alice crossing to the mirror world. Illustration by John Tenniel, from the book "Through the looking glass", by Lewis Carroll.[155]

4

Chiral interactions between electron vortex beams and matter

We study the interaction of chiral matter with a new kind of chiral source: vortex electron beams. We demonstrate large dichroism in the electron energy-loss spectra after inelastic scattering from staircase plasmonic nanostructures and biomolecules. We illustrate this phenomenon with calculations for chiral and nonchiral clusters of silver spheres using both focused and extended electron beams, which exhibit $\sim 10\,\%$ difference between channels of opposite angular momentum. Besides its fundamental interest, this remarkably high dichroism suggests a way of spatially resolving chiral optical excitations, including dark plasmons. We also predict a dichroic response when probing a chiral biomolecule, which suggests the use of these electron beams for resolving different enantiomers.

4.1 Introduction

Vortex electron beams have been theoretically anticipated as propagating solutions of the Schrödinger equation in free space.[156] Since this prediction, a lot of experimental work has been carried out in order to generate these vortices in transmission electron microscopes. In particular, they have been recently produced by passing electron beams through different types of phase masks[157–160] in order to select specific values of the orbital angular momentum. Following a previous suggestion,[156,161] electron vortices have been additionally created by exploiting the interaction between an electron beam and an effective magnetic monopole consisting in a magnetized needle.[162]

These advances have stimulated innovative ways of using electron beams to interact with nanostructured materials. For instance, electron vortices possess a magnetic moment proportional to their OAM that can make them excellent probes of core-level magnetic transitions. Recently, many works have analyzed the range of applicability of these vortices for performing magnetic chiral dichroism.[163–165] A similar effect has been proposed for mapping plasmons in nanostructures.[166] Additionally, the interaction with a longitudinal magnetic field has been predicted to produce Faraday rotation on the electron vortices.[167] This configuration has been further suggested as a way to observe the Aharonov-Bohm effect[168] and Landau states[168] as well as the Gouy phase for quantum matter waves and Zeeman-Larmor rotation.[169] Chiral electron beams have even been postulated as suitable tools for inducing mechanical rotation of nanoparticles,[170,171] thus opening the path to study friction and mechanical motion of nanostructures with an unprecedented spatial control given by the smaller dimensions of the electron beams compared to light or sound waves.

Besides all these promising properties, electron vortex beams can be used to characterize the response of chiral structures. Traditionally, circularly polarized light has been used to probe chiral samples, as they produce polarization-dependent absorption cross-sections (as has been shown in the previous chapter). However, OAM dichroism cannot be observed when employing optical Laguerre-Gauss beams,[172–176] clearly revealing that chiral light-matter coupling is exclusively mediated by the intrinsic angular momentum of light. In contrast, electrons can engage not only in mechanical but also chiral transfer of OAM with matter.[174]

In this chapter, we demonstrate the exchange of OAM between vortex electron beams and two different samples of chiral nature: plasmonic nanostructures and biomolecules. In the first section, we provide a general framework to deal with swift electrons that interact with structures whose optical response is characterized by their electromagnetic Green tensor.

In the following section, this expression is applied to deal with plasmonic tetramers, for both extended and focused incoming electron beams. We predict large differences ($\sim 10\%$) in the intensity of opposite OAM components of electrons that are inelastically scattered from these chiral clusters formed by closely arranged silver nanospheres. Besides, we analyze the contribution of the different plasmonic modes to the loss signal and study the forces and torques exerted on the structure by the electron vortex.

In the final section, we concentrate on the interaction of vortex electron beams with chiral biomolecules, characterized by non-orthogonal electric and magnetic dipoles. We also predict significant dichroism in the electron energy-loss signal produced by α-helix molecules and demonstrate that, for high-energy electrons, the dichroic signal is comparable to that obtained by probing them with circularly polarized light.

4.2 Generalized expression for the transition probability

In this section we derive an expression for the probability that an electron prepared in an incident state i undergoes inelastic transitions to final states f, accompanied by a net transfer of OAM and energy to a chiral sample. The transition rate reads[68]

$$\frac{d\Gamma_{fi}}{dt} = \int d\omega\, \frac{d\Gamma_{fi}(\omega)}{dt},$$

where

$$\frac{d\Gamma_{fi}(\omega)}{dt} = \frac{2\hbar e^2}{\omega^2 m_e^2} \int d^3\mathbf{r}\, d^3\mathbf{r}'\, \psi_f(\mathbf{r})\psi_f^*(\mathbf{r}')[\nabla\psi_i^*(\mathbf{r})] \cdot \mathrm{Im}\{\mathcal{G}(\mathbf{r},\mathbf{r}',\omega)\} \cdot [\nabla\psi_i(\mathbf{r}')] \times \delta(\varepsilon_f - \varepsilon_i + \omega) \tag{4.1}$$

is the spectrally resolved rate, $\hbar\varepsilon_i$ and $\hbar\varepsilon_f$ are the initial and final electron energies, and $\mathcal{G}(\mathbf{r},\mathbf{r}',\omega)$ is the electromagnetic Green tensor, which contains the fully retarded response of the sample. [1]

Swift electrons in a TEM are well described by a plane wave along the propagation

---

[1] Derivations for the expressions regarding the electromagnetic response of chiral samples are provided in the appendices. In particular, the polarizability tensors of chiral materials are given in Appendix B, and their associated Green tensors are presented in Appendix C.

direction $\hat{\mathbf{z}}$,

$$\psi_{i,f}(\mathbf{r}) = \frac{1}{\sqrt{L}} e^{\mathrm{i}p_{zi,f}z} \psi_{i,f\perp}(\mathbf{R}), \tag{4.2}$$

where L is the quantization length along that direction, and the dependence on transversal coordinates $\mathbf{R} = (x, y)$ is taken into account in the transversal wave-function $\psi_{i,f\perp}(\mathbf{R})$.

In what follows, we consider beams of small divergence angle, so that the transversal momentum components $\mathbf{P}$ associated with $\psi_\perp$ are small compared with p_z (*i.e.*, $|p_z| \gg |\mathbf{P}|$). We sum over final plane-wave states and separate this sum into longitudinal and transversal components as

$$\sum_f \rightarrow \frac{L}{2\pi} \int dp_{zf} \sum_{f_\perp}.$$

The low-kinetic energies of the transversal motion allows us to approximate the frequency transfer by

$$\omega = \varepsilon_i - \varepsilon_f \approx q_z \mathrm{v}$$

within the non-recoil approximation, where $q_z = p_{zi} - p_{zf}$ is the wave-vector transfer and v is the electron velocity (*i. e.* $\mathrm{v} = 0.55\,c$ for 100-keV electrons). Then, the p_{zf} integral is performed using the δ function of Eq. (4.1), yielding

$$\int dp_{zf}\, e^{\mathrm{i}(p_{zf}-p_{zi})(z-z')} \delta(\varepsilon_f - \varepsilon_i + \omega) = \frac{1}{v} e^{-\mathrm{i}q_z(z-z')}.$$

We further neglect the gradient of the electron wave function along the transversal direction and divide by the electron beam current v/L in order to obtain the probability per electron. We find

$$\Gamma(\omega) = \sum_{f_\perp} \int d^2\mathbf{R}\, d^2\mathbf{R}'\, \psi_{f\perp}(\mathbf{R}) \psi^*_{i\perp}(\mathbf{R}) \psi^*_{f\perp}(\mathbf{R}') \psi_{i\perp}(\mathbf{R}')\, h(\mathbf{R}, \mathbf{R}', \omega), \tag{4.3}$$

with

$$h(\mathbf{R}, \mathbf{R}', \omega) = \frac{e^2}{\pi\hbar\omega^2} \int dz\, dz'\, e^{-\mathrm{i}q_z(z-z')}\, \mathrm{Im}\{\mathcal{G}_{zz}(\mathbf{r}, \mathbf{r}', \omega)\}, \tag{4.4}$$

where we have dropped the initial-state subindex i. In the following sections we will derive explicit expressions for specific initial wave-functions (described by $\psi_{i\perp}$) interacting with different samples of chiral matter (characterized by the Green tensor $\mathcal{G}_{zz}$).

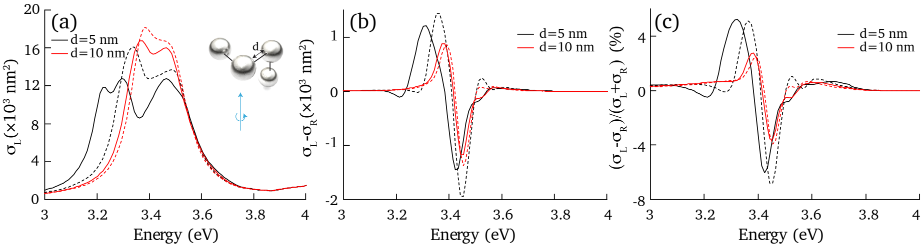

Figure 4.1: Left circularly polarized light extinction cross-section, (a), dichroism, (b), and normalized dichroism, (c), as a function of photon enegy for the cluster shown in the inset of (a) and two different surface-to-surface distances d. Light propagates along the direction of the blue arrow. Continuous (broken) curves correspond to multipolar (dipolar) calculations. The clusters consist of 30-nm silver spheres.

4.3 Chiral plasmonic cluster

In this section we study how electrons interact with plasmons in chiral clusters formed by non-mirror-symmetric geometrical arrangements of metallic spherical nanoparticles.[33, 129] In particular, we address the cases of a staircase tetramer and its mirror image, along with a non-chiral planar trimer. For simplicity, the particles are assumed to be small enough as to describe them through a scalar electric Mie polarizability $\alpha(\omega)$ [see Eq. (3.3)].

As we have argued in the previous chapter, due to multipolar contributions at short inter-particle separations, the validity of the dipolar approximation might be questionable. We show that it is qualitatively correct by examining light extinction cross-sections and circular dichroism spectra, for which we perform converged electromagnetic simulations with full inclusion of all multiples up to a high order using a multiple elastic scattering of multipolar expansions (MESME) approach.[143] In particular, regarding 30-nm silver spheres (with a tabulated permittivity[42]), Fig. 4.1 shows that for surface-to-surface distances of only 5 nm (black curves) the agreement between multipolar and dipolar calculations is qualitatively reasonable and becomes quantitatively good for separations of 10 nm (red cuves). Therefore, presuming a dipolar behavior of the particles turns out to be a good approximation for the 30-nm silver spheres separated by 5-nm gaps that we examine throughout this section.

Plugging the expression for the Green tensor of a cluster of small spheres derived in

Appendix C [Eq. (C.7)], Eq. (4.4) becomes

$$
\begin{aligned}
h(\mathbf{R},\mathbf{R}',\omega) = {} & \frac{e^2}{\pi\hbar\omega^2}\int dz\,dz'\,e^{-\mathrm{i}q_z(z-z')} \\
& \times \sum_{j,j'} \mathrm{Im}\left\{\left[\hat{\mathbf{z}}\cdot\mathcal{G}^0(\mathbf{r}-\mathbf{r}_j,\omega)\right]\cdot\boldsymbol{\alpha}_{jj'}\cdot\left[\hat{\mathbf{z}}\cdot\mathcal{G}^0(\mathbf{r}'-\mathbf{r}_{j'},\omega)\right]\right\},
\end{aligned}
\tag{4.5}
$$

where

$$
\boldsymbol{\alpha} = \frac{\mathbf{1}}{\alpha^{-1}-\mathcal{G}^0}
\tag{4.6}
$$

is a generalized polarizability matrix describing the response of the sample (see Appendix B), $\mathcal{G}^0_{jj'} = \mathcal{G}^0(\mathbf{r}_j-\mathbf{r}_{j'},\omega)$ describes the retarded interaction between particle dipoles at positions $\mathbf{r}_j$ and $\mathbf{r}_{j'}$, and $\mathcal{G}^0(\mathbf{r}-\mathbf{r}_j,\omega)$ is the vacuum Green tensor given by Eq. (C.3). In the above expression, we use matrix notation with indices running over the three Cartesian directions for each and all of the spheres. The evaluation of the z and z' integrals involves

$$
\begin{aligned}
& \int dz\,e^{\mathrm{i}q_z z}\,\hat{\mathbf{z}}\cdot\mathcal{G}^0(\mathbf{r}-\mathbf{r}_j,\omega) = 2\left(\frac{\omega^2}{c^2}\hat{\mathbf{z}}+\nabla_j\partial_{z_j}\right)e^{\mathrm{i}q_z z_j}K_0\left(\frac{q_z|\mathbf{R}-\mathbf{R}_j|}{\gamma}\right) \\
& = 2\mathrm{i}\frac{q_z^2}{\gamma}e^{\mathrm{i}q_z z_j}\left[\frac{(\mathbf{R}-\mathbf{R}_j)}{|\mathbf{R}-\mathbf{R}_j|}K_1\left(\frac{q_z|\mathbf{R}-\mathbf{R}_j|}{\gamma}\right)+\hat{\mathbf{z}}\frac{i}{\gamma}K_0\left(\frac{q_z|\mathbf{R}-\mathbf{R}_j|}{\gamma}\right)\right],
\end{aligned}
$$

where $\gamma = 1/\sqrt{1-(\mathrm{v}/c)^2}$ is the Lorentz factor and K_0 and K_1 are modified Bessel functions of the second kind.

Finally, we find the probability that an electron undergoes a transition between $\psi_{i\perp}$ and $\psi_{f\perp}$ transversal states to have the form

$$
\Gamma(\omega) = \frac{4e^2q_z^2}{\pi\hbar\mathrm{v}^2\gamma^2}\sum_{f_\perp}\mathrm{Im}\{\mathbf{N}^+\cdot\boldsymbol{\alpha}\cdot\mathbf{N}\},
\tag{4.7}
$$

where the spatial components of the electromagnetic matrix element $\mathbf{N}$ associated with particle j are given by

$$
\mathbf{N}_j = e^{\mathrm{i}q_z z_j}\int d^2\mathbf{R}\,\psi^*_{f\perp}(\mathbf{R})\psi_{i\perp}(\mathbf{R})\,\left[\frac{(\mathbf{R}-\mathbf{R}_j)}{|\mathbf{R}-\mathbf{R}_j|}K_1\left(\frac{q_z|\mathbf{R}-\mathbf{R}_j|}{\gamma}\right)+\hat{\mathbf{z}}\frac{i}{\gamma}K_0\left(\frac{q_z|\mathbf{R}-\mathbf{R}_j|}{\gamma}\right)\right].
\tag{4.8}
$$

In the following subsections, we present numerical results obtained by evaluating these expressions for either incident electron plane waves (uniform $\psi_{i\perp}$) or Gaussian beams ($\psi_{i\perp} \propto e^{-R^2/\Delta^2}$). We analyze transitions to a vortex electron carrying a definite amount of OAM $\hbar m_f$, characterized by an orbital momentum number m_f and transversal wave vector P_f, such as

$$\psi_{f\perp}(\mathbf{R}) \propto e^{\mathrm{i}m_f\varphi} J_{m_f}(P_f R),$$

where J_{m_f} is a Bessel function of the first kind.

4.3.1 Transition from a plane wave to a vortex

Inspired by the concept of circular dichroism in optics, we define dichroism in electron energy-loss spectroscopy as the difference in the loss probability of electron vortices with opposite OAM (e.g., $\pm\hbar$). We envision an experiment in which the orbital number m_f can be pre(post)-selected by means of an OAM analyzer placed before (after) the sample. Although the design and fabrication of OAM analyzers still pose a tremendous experimental challenge, excellent progress has been recently made[160, 177–179] in this direction. For simplicity, we study incident beams without a net OAM interacting with chiral samples and resolved in OAM components by a post-selection analyzer, although the present work can be trivially extended to deal with pre-selection analyzers.

In particular, we first consider a 100-keV plane-wave electron passing through a chiral sample and subsequently entering a OAM analyzer, which deflects different m_f components along different outgoing directions [see Fig. 4.2(a)]. Energy loss spectra are recorded for several m_f's through an angle-resolved spectrometer. In the Fourier plane, the transmitted $m_f = \pm1, \pm2$ signals display a characteristic annular pattern, in contrast to the more intense $m_f = 0$ disk-like angular map.

Explicit expression for the cross-section

For an electron plane wave propagating along the direction z, we can write the initial wave function as

$$\psi_{i\perp}(\mathbf{R}) = \frac{1}{\sqrt{A}},$$

where A is the quantization area in the $x-y$ transversal plane. We now consider a complete orthonormal basis set of transversal plane waves labeled by wave vectors $\mathbf{P}_f$, which can be decomposed as

$$\psi_{f\perp}(\mathbf{R}) = \frac{1}{\sqrt{A}} e^{\mathrm{i}\mathbf{P}_f\cdot\mathbf{R}} = \frac{1}{\sqrt{A}} \sum_{m_f=-\infty}^{\infty} \mathrm{i}^{m_f} e^{\mathrm{i}m_f(\varphi-\varphi_{\mathbf{P}_f})} J_{m_f}(P_f R)$$

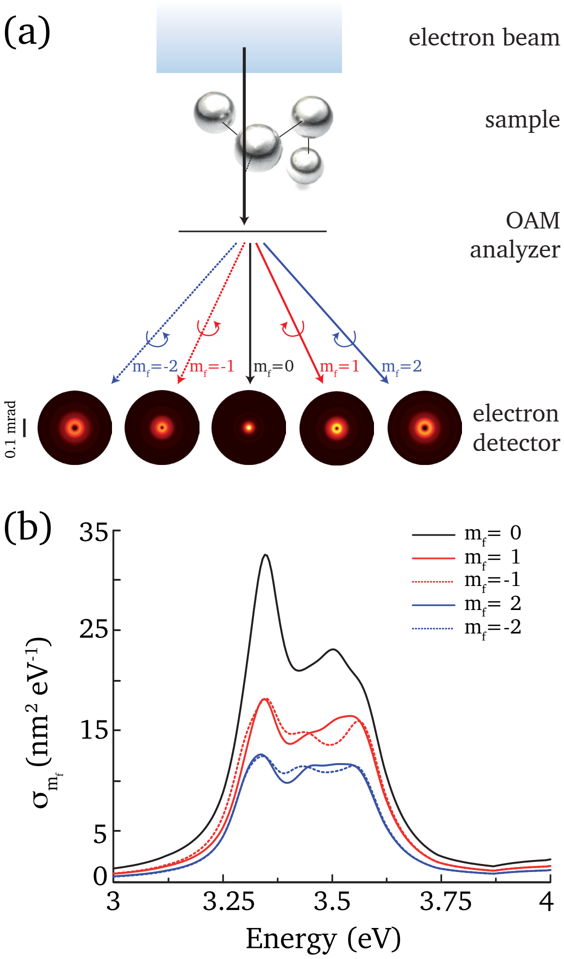

Figure 4.2: (a) Sketch of the system: a 100-keV electron plane wave impinges on a cluster (left-handed tetramer) consisting of four 30-nm silver spheres separated by 5-nm gaps. The electron is subsequently passing through a OAM analyzer that splits the beam into different orbital angular momentum components m_f along different transmission directions. These components are independently energy-analyzed by an angle-resolved spectrometer. The angular distribution of different m_f components are represented at the bottom for a 3.5 eV energy loss. For visualization purposes, the intensities of the $m_f = \pm 1$ and $m_f = \pm 2$ components are multiplied by factors of 5 and 10, respectively. (b) Energy-loss cross-section spectra under the conditions of (a). The origin of OAM is made to coincide with the position of the electron arrow depicted in (a).

in terms of Bessel functions J_m, using polar coordinates $\mathbf{R} = (R, \varphi)$ and $\mathbf{P}_f = (P_f, \varphi_{\mathbf{P}_f})$. As we are only interested in transitions to a given component of final angular momentum m_f, it is convenient to use the complete set of final states

$$\psi_{f\perp}(\mathbf{R}) = \frac{1}{\sqrt{A}} \mathrm{i}^{m_f} e^{\mathrm{i} m_f \varphi} J_{m_f}(P_f R), \tag{4.9}$$

in which each state is characterized by a particular choice of P_f and m_f. With this final state representation, the components of vector $\mathbf{N}$ [given by Eq. (4.8)] become

$$\begin{aligned} \mathbf{N}_j = \frac{(-\mathrm{i})^{m_f}}{A} e^{\mathrm{i} q_z z_j} \int d^2\mathbf{R}\, e^{-\mathrm{i} m_f \varphi} J_{m_f}(P_f R) \\ \times \left[\frac{(\mathbf{R}-\mathbf{R}_j)}{|\mathbf{R}-\mathbf{R}_j|} K_1 \left(\frac{q_z |\mathbf{R}-\mathbf{R}_j|}{\gamma} \right) + \hat{\mathbf{z}} \frac{i}{\gamma} K_0 \left(\frac{q_z |\mathbf{R}-\mathbf{R}_j|}{\gamma} \right) \right]. \end{aligned}$$

The angular integral of the z component of this vector reduces to

$$\int d\varphi\, e^{-\mathrm{i} m_f \varphi} K_0 \left(\frac{q_z |\mathbf{R}-\mathbf{R}_j|}{\gamma} \right) = 2\pi\, e^{-\mathrm{i} m_f \varphi_j} I_{m_f} \left(\frac{q_z R_<}{\gamma} \right) K_{m_f} \left(\frac{q_z R_>}{\gamma} \right),$$

where $R_< = \min\{R, R_j\}$, $R_> = \max\{R, R_j\}$, and I_m and K_m are modified Bessel functions. Likewise, the remaining transversal components involve

$$\begin{aligned} \int d\varphi\, e^{-\mathrm{i} m_f \varphi} \frac{(\mathbf{R}-\mathbf{R}_j)}{|\mathbf{R}-\mathbf{R}_j|} K_1 \left(\frac{q_z |\mathbf{R}-\mathbf{R}_j|}{\gamma} \right) = 2\pi e^{-\mathrm{i} m_f \varphi_j} \\ \times \begin{cases} I_{m_f}\left(\frac{q_z R}{\gamma}\right) K'_{m_f}\left(\frac{q_z R_j}{\gamma}\right) \hat{\mathbf{R}}_j - \mathrm{i} m_f \frac{\gamma}{q_z R_j} I_{m_f}\left(\frac{q_z R}{\gamma}\right) K_{m_f}\left(\frac{q_z R_j}{\gamma}\right) \hat{\varphi}_j, & (R \le R_j) \\ K_{m_f}\left(\frac{q_z R}{\gamma}\right) I'_{m_f}\left(\frac{q_z R_j}{\gamma}\right) \hat{\mathbf{R}}_j - \mathrm{i} m_f \frac{\gamma}{q_z R_j} K_{m_f}\left(\frac{q_z R}{\gamma}\right) I_{m_f}\left(\frac{q_z R_j}{\gamma}\right) \hat{\varphi}_j, & (R > R_j) \end{cases} \end{aligned}$$

where (R_j, φ_j) are the polar coordinates of $\mathbf{R}_j$. For the incident plane wave under consideration, it is useful to define the loss cross-section, which we separate in different frequency-loss components as

$$\sigma_{m_f} = \int_0^\infty d\omega\, \sigma_{m_f}(\omega).$$

We obtain the cross-section as the transition probability per electron multiplied by the transversal area A, that is, $\sigma_{m_f}(\omega) = A\Gamma(\omega)$. A more convenient expression is derived by summing over final transversal wave vectors $\mathbf{P}_f$ using the customary prescription

$$\sum_{f_\perp} \to \frac{A}{(2\pi)^2} \int_0^\infty P_f\, dP_f \int_0^{2\pi} d\varphi_f = \frac{A}{2\pi} \int_0^\infty P_f\, dP_f,$$

which leads to

$$\sigma_{m_f}(\omega) = \frac{8e^2 q_z^2}{\hbar \mathrm{v}^2 \gamma^2} \int_0^\infty P_f \, dP_f \, \mathrm{Im}\left\{ \mathbf{M}^+ \cdot \frac{\mathbf{1}}{\alpha^{-1} - \mathcal{G}^0} \cdot \mathbf{M} \right\}, \tag{4.10}$$

where the components of vector **M** are

$$\begin{aligned} \mathbf{M}_j =& e^{\mathrm{i} q_z z_j} e^{-\mathrm{i} m_f \varphi_j} \times \left\{ \left[g_1 \, K'_{m_f}\left(\frac{q_z R_j}{\gamma}\right) + g_2 \, I'_{m_f}\left(\frac{q_z R_j}{\gamma}\right) \right] \hat{R}_j \right. \\ & \left. + \left[g_1 \, K_{m_f}\left(\frac{q_z R_j}{\gamma}\right) + g_2 \, I_{m_f}\left(\frac{q_z R_j}{\gamma}\right) \right] \mathrm{i} \left(\frac{-m_f \gamma}{R_j q_z} \hat{\varphi}_j + \frac{1}{\gamma} \hat{z}_j \right) \right\}. \end{aligned} \tag{4.11}$$

Here, we have defined

$$g_1 = \int_0^{R_j} R \, dR \, J_{m_f}(P_f R) \, I_{m_f}\left(\frac{q_z R}{\gamma}\right), \tag{4.12a}$$

$$g_2 = \int_{R_j}^{\infty} R \, dR \, J_{m_f}(P_f R) \, K_{m_f}\left(\frac{q_z R}{\gamma}\right). \tag{4.12b}$$

Dichroism for different enantiomeric clusters

The spectrally resolved cross-section exhibits complex features with several peaks, corresponding to the excitation of plasmons in the cluster [Fig. 4.2(b)]. The $m_f = \pm 1$ spectra show slightly different intensity for each of the spectral features. This prompts us to define the absolute and relative degrees of dichroism associated with the orbital number m_f as $\sigma_{m_f} - \sigma_{-m_f}$ and $(\sigma_{m_f} - \sigma_{-m_f})/(\sigma_{m_f} + \sigma_{-m_f})$, respectively. For the clusters under consideration, these quantities decrease with increasing m_f [see Fig. 4.2(b)].

Figure 4.3 displays the $m_f = 1$ dichroism produced by different clusters. The relative electron dichroism reaches up to $\sim$ 10%, which is remarkably high compared with typical values in its optical counterpart.[29,30] As expected, the effect changes sign upon mirror reflection of the sample, while a cluster formed by only three particles lying on a plane normal to the beam does not produce dichroism at all, as it is not seen as chiral by the electron. In contrast, a net dichroism effect is observed for the trimer by tilting it [Fig. 4.3(c)], so that the electron sees again a staircase-like structure along the direction of electron propagation. In optics, this phenomenon is known as extrinsic dichroism, which is produced when oriented non-chiral molecules form a chiral triad with the light wave vector.[180–182] This is precisely what happens when the normal of the plane that contains the cluster is tilted with respect to the

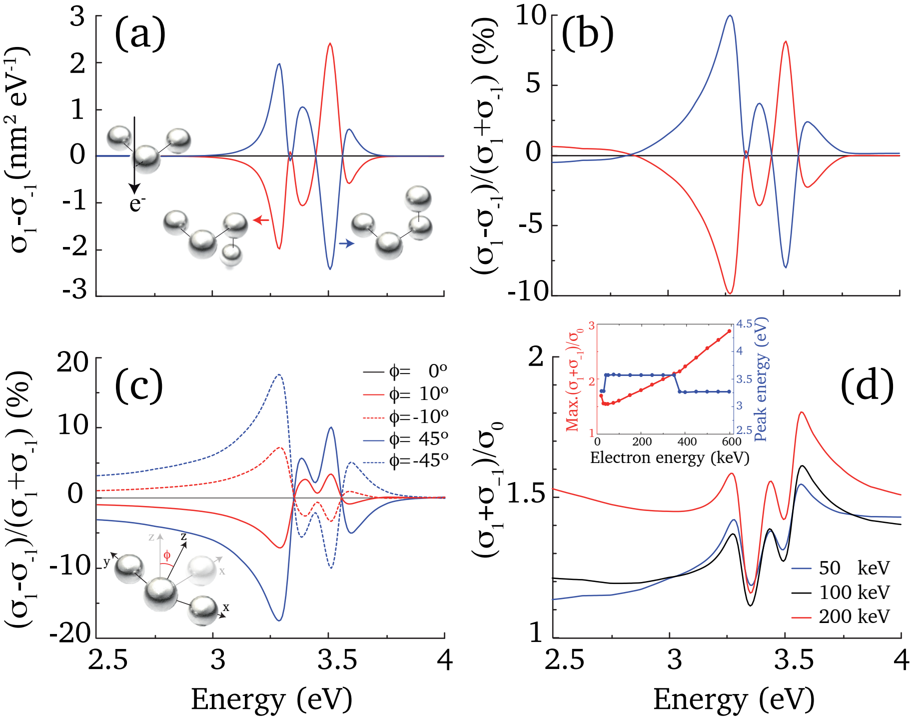

Figure 4.3: (a) Dichroism between $m_f = \pm 1$ components in the spectrally resolved inelastic cross-section of 100-keV electrons for different clusters of 30-nm silver spheres with gaps of 5-nm (see insets). The planar trimer does not exhibit any dichroism. (b) Same as (a), normalized to the sum of $m_f = \pm 1$ cross-sections. (c) Extrinsic dichroism displayed by the trimer when it is tilted with respect to the direction of electron propagation. (d) Partial $m_f = \pm 1$ inelastic cross-sections normalized to the $m_f = 0$ transmitted beam component for different electron energies in the left-handed tetramer. The inset of (d) shows the maximum of this ratio (left, red curve) and the energy loss at which this happens (right, blue curve) as a function of electron energy. The origin of OAM is the same as in Fig. 4.2

electron incidence direction, and once more, the effect changes sign upon mirror reflection of the sample. However, this apparent chirality is erased when averaging over all cluster orientations.

Remarkably, the fraction of inelastically scattered electrons that transfer OAM is actually large. Figure 4.3(d) compares the $m_f = \pm 1$ and $m_f = 0$ components. For 100-keV electrons, $\sigma_1 \simeq 0.75\,\sigma_0$ at $\omega \sim 3.5$ eV, pointing out the significant contribution of the chiral components to the total energy loss.

Influence of relevant parameters on electron dichroism

In the previous chapter we showed that optical dichroism is very sensitive to the distribution of sizes and separations between the particles in the clusters. As expected, these parameters also play an important role in determining the strength of the chiral coupling to the electron.

In particular, the dependence on the material, size, and separation between particles is analyzed in Figs. 4.4(a)-(c). The dichroism for silver spheres is remarkably large compared to that of gold particles [Fig. 4.4(a)] because silver is a less lossy material. Both the EELS intensity and the dichroism increase with particle size [Fig. 4.4(c)], but the latter is reduced with particle separation [Fig. 4.4(b)]. This is in agreement with the intuitive idea that larger structures can transfer a bigger amount of angular momentum, provided the coupling between spheres is sufficiently strong (*i.e.*, close interaction between the spheres is required to sustain a strong chiral plasmon that extends over the entire cluster).

The coupling to different chiral modes of the sample is also strongly affected by the relative position and alignment between the cluster and the vortex generator [Fig. 4.4(d)]. More precisely, the origin of electron OAM (*i.e.*, the origin of azimuthal angles φ) is referred to the center of OAM analyzer. If the planes of the sample and the analyzer are taken to be conjugated in the electron optics setup, with a 1:100 demagnification factor for the latter, relative alignment requires sub-micron-scale displacements of the analyzer to produce nanometer-scale displacements at the conjugated sample plane.

Mode decomposition in the non-retarded limit

It is fair to wonder whether all plasmonic modes contribute to the dichroic response displayed by the chiral tetramers. In the non-retarded limit ($c \rightarrow \infty$), we can decompose the energy loss experienced by the electron into a sum of all these modes and determine their individual contributions.

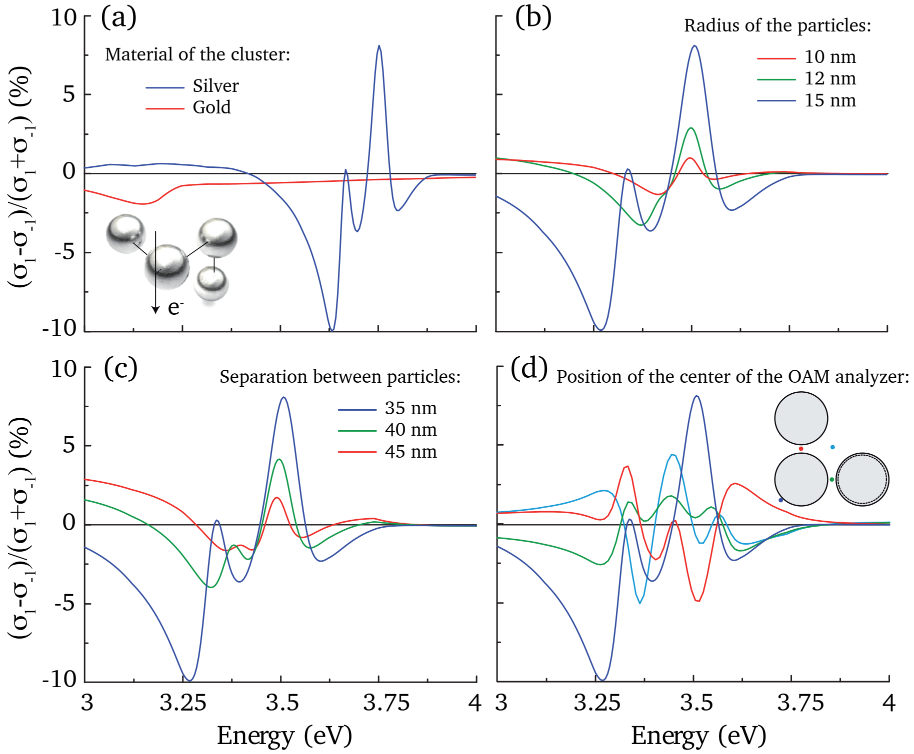

Figure 4.4: (a-c) Influence of cluster material (a), particle size (b), and separation between particles (c), on the dichroism produced on a plane-wave electron upon interation with a staircase chiral tetramer arrangement of spheres [see inset in (a)]. (d) Dichroism for different positions of the OAM analyzer relative to the tetramer. Each spectral curve corresponds to a position of the analyzer center as indicated by a dot of the same color in the inset. The following default parameters are assumed, unless otherwise specified (see legends): 100-keV electrons, 15-nm particle radius, and 35-nm center-to-center particle spacing. In (a-c) the analyzer is at the position of the electron arrow of the inset to (a), which corresponds to the dark blue dot of the inset to (d).

In this regime, Eq. (4.1) reduces to[68]

$$\frac{d\Gamma(\omega)}{dt} = \frac{2e^2}{\hbar}\sum_f \int d^3\mathbf{r}\, d^3\mathbf{r}'\, \psi_f(\mathbf{r})\psi_i^*(\mathbf{r})\psi_f^*(\mathbf{r}')\psi_i(\mathbf{r}')\,\mathrm{Im}\{-W^{\mathrm{ind}}(\mathbf{r},\mathbf{r}',\omega)\} \qquad (4.13)$$
$$\times\, \delta(\varepsilon_f - \varepsilon_i + \omega),$$

where the coupling to the sample is mediated by the electrostatic screened interaction W^{ind}, which is defined as the electric potential induced at $\mathbf{r}$ by an external point charge at $\mathbf{r}'$. For a cluster composed of n particles, it is given by

$$W^{\mathrm{ind}}(\mathbf{r},\mathbf{r}',\omega) = -\mathbf{S}(\mathbf{r})^+ \cdot \frac{\mathbf{1}}{\alpha^{-1}(\omega) - \mathcal{G}^0} \cdot \mathbf{S}(\mathbf{r}'), \qquad (4.14)$$

where the components of vector $\mathbf{S}$ run over the three Cartesian directions for each and all of the spheres j and read

$$\mathbf{S}_j(\mathbf{r}) = \frac{\mathbf{r} - \mathbf{r}_j}{|\mathbf{r} - \mathbf{r}_j|^3} = \nabla_j \frac{1}{|\mathbf{r} - \mathbf{r}_j|}.$$

Equation (4.14) can be derived in a similar way as its retarded counterpart (see Appendix C). Likewise, the non-retarded Green tensor $\mathcal{G}^0$ is given by the $k \to 0$ limit of Eq. (C.2). As $\mathcal{G}^0$ is real and symmetric, its eigenvectors form an orthonormal basis set, each of them defining a mode of the system. The energy loss suffered by the electron can then be separated as the sum of the contributions from the resulting $3n$ modes. Using matrix notation

$$\mathcal{G}^0\, \mathbf{p}_l = \mu_l \mathbf{p}_l,$$

where $\mathbf{p}_l$ and μ_l are the real eigenvector and eigenvalue of mode l, Eq. (4.14) can be recast into

$$W^{\mathrm{ind}}(\mathbf{r},\mathbf{r}',\omega) = -\sum_l \mathbf{S}(\mathbf{r})^+ \cdot \mathbf{p}_l \frac{\mathbf{1}}{\alpha^{-1}(\omega) - \mu_l} \mathbf{p}_l^+ \cdot \mathbf{S}(\mathbf{r}').$$

After some algebra, the loss probability reduces to

$$\Gamma(\omega) = \frac{e^2}{\pi\hbar v^2}\sum_l \left[\mathrm{Im}\left\{ \frac{\mathbf{1}}{\alpha^{-1}(\omega) - \mu_l} \right\} \sum_{f_\perp} |N_l|^2 \right],$$

where

$$N_l = \int d^3\mathbf{r}\, e^{\mathrm{i}q_z z} \psi_{f\perp}^*(\mathbf{R})\, \psi_{i\perp}(\mathbf{R})\, \mathbf{p}_l^+ \cdot \mathbf{S}(\mathbf{r})$$
$$= \frac{1}{\pi}\sum_j \mathbf{p}_{l,j} \cdot \nabla_j\, e^{\mathrm{i}q_z z_J} \int d^2\mathbf{R} \int d^2\mathbf{Q}\, \frac{e^{-\mathrm{i}\mathbf{Q}\cdot(\mathbf{R}-\mathbf{R}_j)}}{Q^2 + q_z^2}\, \psi_{f\perp}^*(\mathbf{R})\psi_{i\perp}(\mathbf{R}).$$

Finally, for a transition from an incident plane wave to a m_f vortex beam, the inelastic cross-section reads

$$\sigma_{m_f}(\omega) = \frac{8e^2}{\hbar v^2} \sum_l \left[\mathrm{Im}\left\{ \frac{\mathbf{1}}{\alpha^{-1}(\omega) - \mu_l} \right\} \int_0^\infty \frac{P_f \, dP_f}{\left[P_f^2 + q_z^2\right]^2} |M_l(P_f)|^2 \right],$$

where

$$M_l(P_f) = \sum_j \mathbf{p}_{l,j} \cdot \nabla_j \left[e^{-\mathrm{i}m_f \varphi_j} e^{\mathrm{i}q_z z_j} J_{m_f}(P_f R_j) \right].$$

We compare retarded and non-retarded calculations in Fig. 4.5(a). Incidentaly, all of the modes contribute to both the energy loss and the dichroism, thus resulting in a non-trivial dichroic signal that cannot be ascribed in general to specific dominant modes [see Fig. 4.5(b,c)]. Since the non-retarded theory is qualitatively correct, we endorse it in next section to analyze the transfer of mechanical angular momentum to the sample.

Mechanical transfer of linear and angular momentum to the sample

Due to conservation of angular momentum, the OAM transferred by the electron produces a mechanical torque on the cluster, which can be separated into two different contributions: intrinsic torque acting on each individual particle and extrinsic torque acting on the cluster as a whole, relative to the origin of electron OAM. Additionally, cathodoluminescence emission might take a net amount of angular momentum that needs to be included in this balance.

As we show below, neglecting retardation (and therefore, cathodoluminescence), the increase in mechanical angular momentum (intrinsic plus extrinsic) produced by the self-consistent electromagnetic field arising from interaction with the electron exactly accounts for the electron momentum transfer.

The torque and force exerted by the electron on the cluster can be calculated from the Maxwell's stress tensor (see Appendix A). In what follows, we summarize the resulting expressions for a non-monochromatic external field (like the one produced by an electron). The torque contains both extrinsic and intrisic contributions:

$$\boldsymbol{\tau}(\omega) = \sum_j \boldsymbol{\tau}_j^i(\omega) + \boldsymbol{\tau}_j^e(\omega).$$

The intrinsic torque acting on particle j, which makes that particle spin around its axes, reduces to

$$\tau_j^i(\omega) = \frac{1}{\pi}\left[\mathrm{Re}\left\{\mathbf{p}_j \times \mathbf{E}_j^*\right\} + \frac{2k^3}{3}\mathrm{Im}\left\{\mathbf{p}_j \times \mathbf{p}_j^*\right\}\right],$$

whereas the extrinsic component, which contributes to rotations of the cluster as a whole, is

$$\tau_j^e(\omega) = \mathbf{r}_j \times \mathbf{F}_j(\omega),$$

where the force on particle j is written as

$$\mathbf{F}_j(\omega) = \frac{1}{\pi}\sum_{\beta=x,y,z}\mathrm{Re}\left\{p_{j,\beta}\nabla E_{j,\beta}^*\right\}.$$

In these expressions, the field reads

$$\mathbf{E}_j(\omega) = \alpha^{-1}\sum_{j'}\left(\frac{\mathbf{1}}{\alpha^{-1} - \mathcal{G}^0}\right)_{jj'} \cdot \mathbf{E}_{j'}^{\mathrm{ext}},$$

where $\mathbf{E}_{j'}^{\mathrm{ext}}$ is the external field of the electron.

Since radiation corrections can be neglected in the non-retarded limit, the transfer of linear momentum along z has to precisely coincide with the time-integral of the force in that direction. A detailed balance expression can be written in frequency components as

$$F_z(\omega) = \frac{\hbar\omega}{\mathrm{v}}\Gamma(\omega).$$

Additionally, the angular momentum transfer to the cluster, obtained from the integral of $\tau(\omega)$ over the entire frequency spectrum, should be the opposite of the orbital momentum gained by the electron. Taking into account that the incident electron has no orbital angular momentum, conservation of the z component leads to

$$\tau_z(\omega) = -\hbar m\Gamma(\omega).$$

It is not difficult to analytically corroborate the above expressions for a single particle. However, for clusters consisting of several particles, the algebra becomes rather involved, but we have numerically verified them up to the computer numerical precision.

As shown in Fig. 4.5(d), the extrinsic torque dominates the transfer to this particular chiral cluster. Nevertheless, the relative contributions of the intrinsic and extrinsic torques are very dependent on geometry, and their relative weight might be modified for different arrangements.

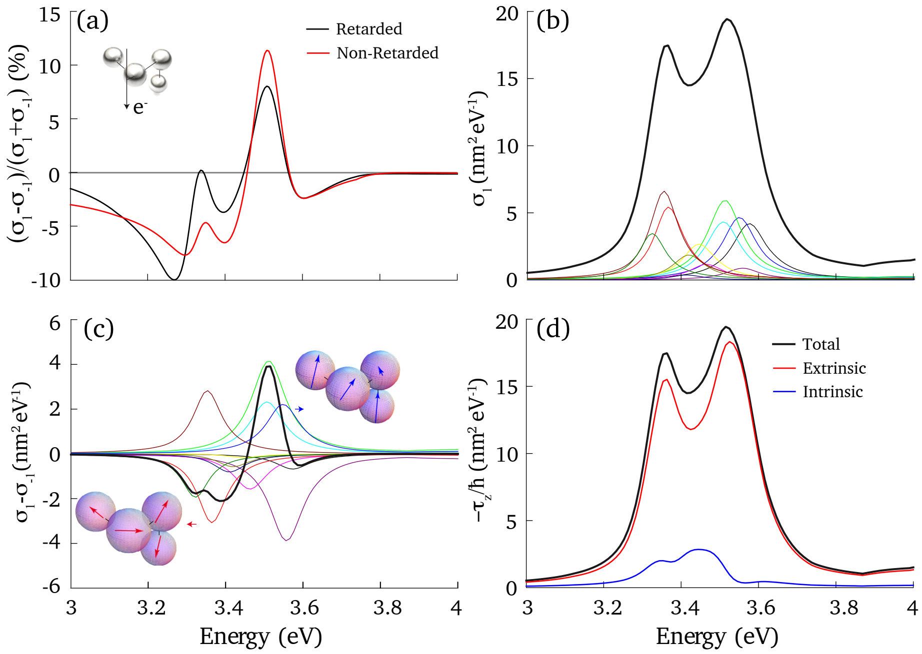

Figure 4.5: (a) Retarded and non-retarded dichroism for the cluster shown in the inset. (b,c) Non-retarded calculation of the inelastic cross-section (b), and the dichroism (c). The black curve corresponds to the total result, while the contributions of individual plasmon modes are shown in different colors. The insets in (c) illustrate the dipole orientations for two of these modes. The incident electron is a plane wave of 100-keV energy, while the cluster is made of 30-nm silver spheres separated by 5-nm gaps. (d) Total, extrinsic, and intrinsic z-component of the non-retarded torque, normalized to yield cross-section units. We consider transitions from the incident plane wave to a $m = 1$ vortex in all cases.

4.3.2 Transition from a gaussian beam to a vortex

In this section, we propose to rely on the excellent spatial resolution of electron microscopes for visualizing optical near fields[67,68,183] in order to study the chirality associated with each of the observed plasmon features. The incident transversally focused beam is well represented by a Gaussian wave function

$$\psi_{i\perp}(\mathbf{R}) = \frac{1}{\sqrt{\pi}\Delta} e^{-R^2/\Delta^2},$$

where the full width at half maximum of the beam is $2\sqrt{\ln 2}\Delta \approx 1.4\,\Delta$. We analyze again the final vortex states of Eq. (4.9) and concentrate on a specific final angular momentum number m_f. Following the same procedure as before, we find that the loss probability reduces to

$$\Gamma_{m_f}(\omega) = \frac{8e^2 q_z^2}{\pi\hbar\Delta^2 \mathrm{v}^2\gamma^2} \int_0^\infty P_f\, dP_f \,\mathrm{Im}\left\{\mathbf{M}^+ \cdot \frac{\mathbf{1}}{\alpha^{-1} - \mathcal{G}^0} \cdot \mathbf{M}\right\}, \tag{4.15}$$

where vector $\mathbf{M}$ is still given by Eq. (4.11) with an appropriate redefinition of functions

$$g_1 = \int_0^{R_j} R\,dR\, J_{m_f}(P_f R)\, I_{m_f}\left(\frac{q_z R}{\gamma}\right) e^{-R^2/\Delta^2},$$

$$g_2 = \int_{R_j}^\infty R\,dR\, J_{m_f}(P_f R)\, K_{m_f}\left(\frac{q_z R}{\gamma}\right) e^{-R^2/\Delta^2}.$$

We show some calculated spectra for incident Gaussian beams of different FWHM and $m_f = 1$ in Fig. 4.6(a,b). Selected maps of the EELS intensity (upper plots) and the dichroism (lower plots) as a function of beam position reveal that both of these quantities are enhanced at the particle gaps [Fig. 4.6(c,d)]. However, the dichroic signal is more delocalized and changes sign when moving from the gaps to other neighboring regions of the cluster. The net orbital angular momentum transfer is thus rather sensitive to the position of the beam relative to the sample, since different plasmonic modes are more efficiently excited.

Remarkably, we find the relative degree of dichroism to display a sign and magnitude that are rather independent on the Gaussian focusing Δ, although the absolute effect quickly vanishes for beams that are much narrower than the size of the plasmon modes.

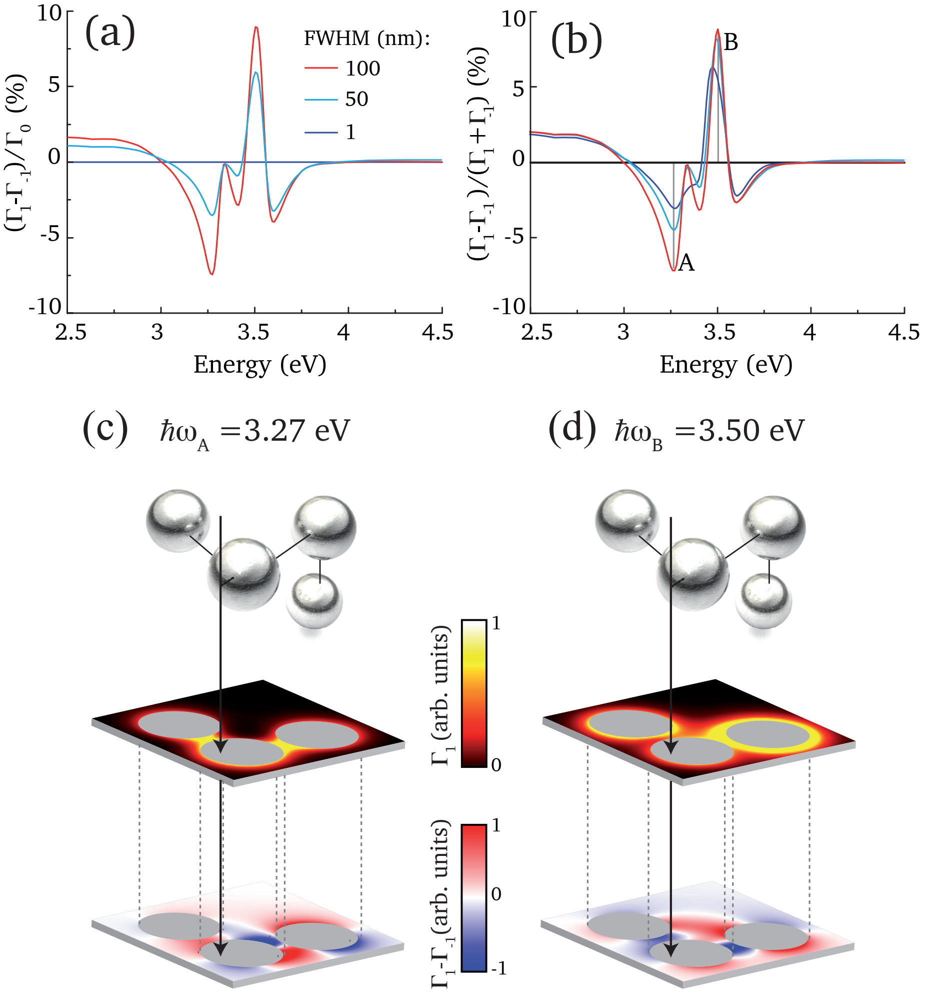

Figure 4.6: Dichroism for a focused electron beam. (a,b) Absolute (a) and relative (b) degrees of dichroism for Gaussian beams of $\exp(-R^2/\Delta^2)$ profile with different values of the FWHM. The position and orientation of the beam relative to the sample is shown in the inset of (c). The origin of orbital angular momentum is made to coincide with the center of the electron beam. (c,d) Energy loss probability (upper density plots) and dichroism (lower plots) distributions as a function of beam position for FWHM= 1 nm and two different loss energies, corresponding to features A and B in (b). The electron energy is 100 keV. The cluster is made of 30-nm silver spheres separated by 5-nm gaps.

4.4 Chiral molecule

In the previous sections we have dealt with a chiral cluster that breaks parity symmetry due to a particular geometrical arrangement of spherical particles. However, it is also possible to break mirror symmetry by combining non-orthogonal electric (polar vector) and magnetic (axial vector) dipoles in one point of the space. This is precisely how chiral molecules are characterized.[28] In particular, the polarizability tensor of these molecules contains electric ($\alpha_{\rm EE}$), magnetic ($\alpha_{\rm MM}$), and magneto-electric ($\alpha_{\rm ME} = -\alpha_{\rm EM}^T$, due to reciprocity[184]) components that are reunited in the matrix

$$\boldsymbol{\alpha} = \begin{bmatrix} \alpha_{\rm EE} & \alpha_{\rm EM} \\ \alpha_{\rm ME} & \alpha_{\rm MM} \end{bmatrix},$$

and whose specific expressions are given in Appendix B.

It can be demonstrated that, as in the optical case, electron dichroism arises from the off-diagonal elements. The energy-loss probability for a chiral molecule placed at the position $\mathbf{r}_0$ with respect to the origin of the electron vortex can be obtained from Eqs. (4.3) and (4.4), in which the Green tensor is now given by Eq. (C.11) (see Appendix C). We find

$$h(\mathbf{R},\mathbf{R}',\omega) = \frac{e^2}{\pi\hbar\omega^2}\int dz\, dz'\, e^{-{\rm i}q_z(z-z')}\,{\rm Im}\left\{\mathbf{T}^T(\mathbf{r}-\mathbf{r}_0,\omega)\cdot\boldsymbol{\alpha}\cdot\mathbf{T}(\mathbf{r}_0-\mathbf{r}',\omega)\right\},$$

where $\mathbf{T}(\mathbf{r}_0-\mathbf{r}',\omega)$ is a vector obtained by projecting the electric-electric induced Green tensor on the $\hat{\mathbf{z}}$ direction. Specifically,

$$\mathbf{T}(\mathbf{r}_0-\mathbf{r}',\omega) = \begin{bmatrix} \hat{\mathbf{x}}\cdot\mathcal{G}^0_{EE}(\mathbf{r}_0-\mathbf{r}',\omega)\cdot\hat{\mathbf{z}} \\ \hat{\mathbf{y}}\cdot\mathcal{G}^0_{EE}(\mathbf{r}_0-\mathbf{r}',\omega)\cdot\hat{\mathbf{z}} \\ \hat{\mathbf{z}}\cdot\mathcal{G}^0_{EE}(\mathbf{r}_0-\mathbf{r}',\omega)\cdot\hat{\mathbf{z}} \\ \hat{\mathbf{x}}\cdot\mathcal{G}^0_{ME}(\mathbf{r}_0-\mathbf{r}',\omega)\cdot\hat{\mathbf{z}} \\ \hat{\mathbf{y}}\cdot\mathcal{G}^0_{ME}(\mathbf{r}_0-\mathbf{r}',\omega)\cdot\hat{\mathbf{z}} \\ \hat{\mathbf{z}}\cdot\mathcal{G}^0_{ME}(\mathbf{r}_0-\mathbf{r}',\omega)\cdot\hat{\mathbf{z}} \end{bmatrix}.$$

Following an almost identical derivation as the one in the previous section, and considering the symmetries of the free-space Green functions, we obtain a formally identical expression as Eq. (4.7) for the loss probability:

$$\Gamma(\omega) = \frac{4e^2q_z^2}{\pi\hbar v^2\gamma^2}\sum_{f_\perp}{\rm Im}\{\mathbf{N}^+\cdot\boldsymbol{\alpha}\cdot\mathbf{N}\}, \qquad (4.16)$$

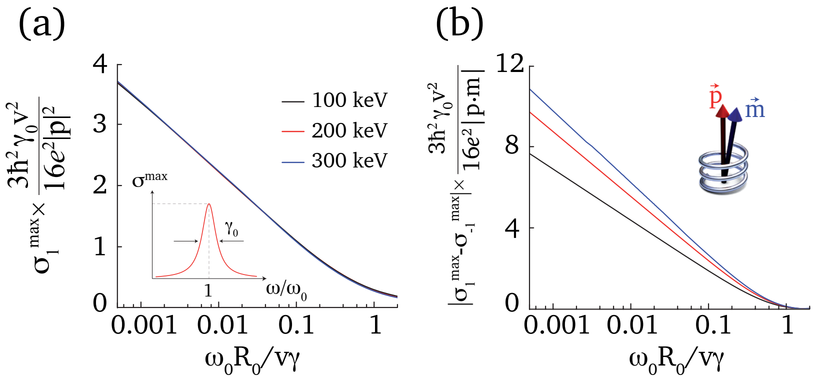

Figure 4.7: (a) Normalized maximum of the partial inelastic cross-section $\sigma_1$and (b) dichroism $|\sigma_1 - \sigma_{-1}|$ for a randomly oriented model point structure characterized by a chiral excitation of frequency ω_0, width γ_0, and associated electric and magnetic dipole moments **p** and **m** [see inset to (b)]. The cross-section and dichroism spectra follow a Lorentzian profile [see inset to (a)]. The origin of OAM is displaced a distance R_0 with respect to the structure. The vertical axes are normalized to yield universal curves that only depend on the electron energy (see legend) and $\omega_0 R_0/v\gamma$.

where the electromagnetic matrix element $\mathbf{N} = [\mathbf{N}_{EE},\ \mathbf{N}_{ME}]$ has both electric and crossed magnetic-electric components:

$$\mathbf{N}_{EE} = \int d^2\mathbf{R}\,\psi^*_{f\perp}(\mathbf{R})\,\psi_{i\perp}(\mathbf{R})\,\left[\frac{(\mathbf{R}-\mathbf{R}_0)}{|\mathbf{R}-\mathbf{R}_0|}K_1\left(\frac{q_z|\mathbf{R}-\mathbf{R}_0|}{\gamma}\right) + \hat{\mathbf{z}}\frac{\mathrm{i}}{\gamma}K_0\left(\frac{q_z|\mathbf{R}-\mathbf{R}_0|}{\gamma}\right)\right], \tag{4.17a}$$

$$\mathbf{N}_{ME} = \frac{\mathrm{v}}{c}\int d^2\mathbf{R}\,\psi^*_{f\perp}(\mathbf{R})\,\psi_{i\perp}(\mathbf{R})\,K_1\left(\frac{q_z|\mathbf{R}-\mathbf{R}_0|}{\gamma}\right)\hat{\mathbf{z}}\times\frac{(\mathbf{R}-\mathbf{R}_0)}{|\mathbf{R}-\mathbf{R}_0|}. \tag{4.17b}$$

Interestingly, the magnetic-electric crossed term is proportional to the ratio between the electron and light velocities, therefore suggesting that high-energy electrons are best suited to study chiral molecules.

In particular, for the plane-wave to vortex beam transition, the loss cross-section is formally equivalent to that obtained for the cluster of spheres,

$$\sigma_{m_f}(\omega) = \frac{8e^2q_z^2}{\hbar\mathrm{v}^2\gamma^2}\int_0^\infty P_f\,dP_f\,\mathrm{Im}\left\{\mathbf{M}^+\cdot\alpha\cdot\mathbf{M}\right\},$$

but here the polarizability corresponds to the chiral molecule and the components of vector $\mathbf{M} = [\mathbf{M}_{EE}, \mathbf{M}_{ME}]$ are

$$\begin{aligned}
\mathbf{M}_{EE} = & \left[g_1 \, K'_{m_f} \left(\frac{q_z R_0}{\gamma} \right) + g_2 \, I'_{m_f} \left(\frac{q_z R_0}{\gamma} \right) \right] \hat{R}_0 \\
& + \left[g_1 \, K_{m_f} \left(\frac{q_z R_0}{\gamma} \right) + g_2 \, I_{m_f} \left(\frac{q_z R_0}{\gamma} \right) \right] \mathrm{i} \left(\frac{-m_f \gamma}{R_0 q_z} \hat{\varphi}_0 + \frac{1}{\gamma} \hat{z}_0 \right), \\
\mathbf{M}_{ME} = & \frac{v}{c} \left[g_1 \, K_{m_f} \left(\frac{q_z R_0}{\gamma} \right) + g_2 \, I_{m_f} \left(\frac{q_z R_0}{\gamma} \right) \right] \mathrm{i} \frac{m_f \gamma}{R_0 q_z} \hat{R}_0 \\
& + \frac{v}{c} \left[g_1 \, K'_{m_f} \left(\frac{q_z R_0}{\gamma} \right) + g_2 \, I'_{m_f} \left(\frac{q_z R_0}{\gamma} \right) \right] \hat{\varphi}_0 .
\end{aligned}$$

Here, g_1 and g_2 are defined in Eqs. (4.12).

Model point structure

In Fig. 4.7 we study σ_1 (left panels) and the dichroism $|\sigma_1 - \sigma_{-1}|$ (right panels) as a function of energy loss for a model point structure. It is assumed to be randomly oriented and placed a distance R_0 apart from the origin of OAM. The model structure has a single chiral resonance of frequency ω_0, spectral width γ_0, and associated electric and magnetic dipole moments $\mathbf{p}$ and $\mathbf{m}$, respectively. The maxima of σ_1 and $|\sigma_1 - \sigma_{-1}|$ are normalized to yield the universal curves shown in Fig. 4.7(a,b), which only depend on electron energy and $\omega_0 R_0 / \mathrm{v}\gamma$. These results can be applied to molecules and metamolecules[184] by simply plugging their corresponding spectral parameters. It is common to have $|\mathbf{m}| \ll |\mathbf{p}|$, so that the cross-section is roughly proportional to $|\mathbf{p}|^2$, whereas the dichroism scales as $|\mathbf{m} \cdot \mathbf{p}|$. Interestingly, the dichroism diverges logarithmically with decreasing R_0, thus suggesting a possible approach towards ultrasensitive detection of chirality consisting in lowering R_0 by employing a highly demagnified OAM analyzer.

Specific biomolecule: α-helix

Results for the α-helix are presented in Fig. 4.8 using the parameters shown in Table 4.1 to model its resonances and taking $R_0 = 1\,\mathrm{nm}$. The polarizability of this common secondary structure of proteins in the 190-220 nm spectral region is dominated by three main UV resonances, each of them contributing with a Lorentizian term like in Eqs. (B.4).

The magnetic dipole associated with each resonance is considered to be parallel to the electric one, as only that component of $\mathbf{m}$ produces dichroism. The orientation of these dipoles relative to the molecule long axis are given in the polarization

Band	$\hbar\omega_0$ (eV)	$\hbar\gamma_0$ (eV)	Polarization	r_{eg} (nm)	r_0 (nm)
1	6.53	0.5	$\pi \rightarrow \pi^*$, $\perp$	0.048	0.12
2	5.96	0.4	$\pi \rightarrow \pi^*$, $\parallel$	0.022	-0.22
3	5.64	0.4	$n \rightarrow \pi^*$, $\parallel$	0.01	-0.82

Table 4.1: Absorption bands of the α-helix, as fitted from Johnson and Tinoco.[185, 186]

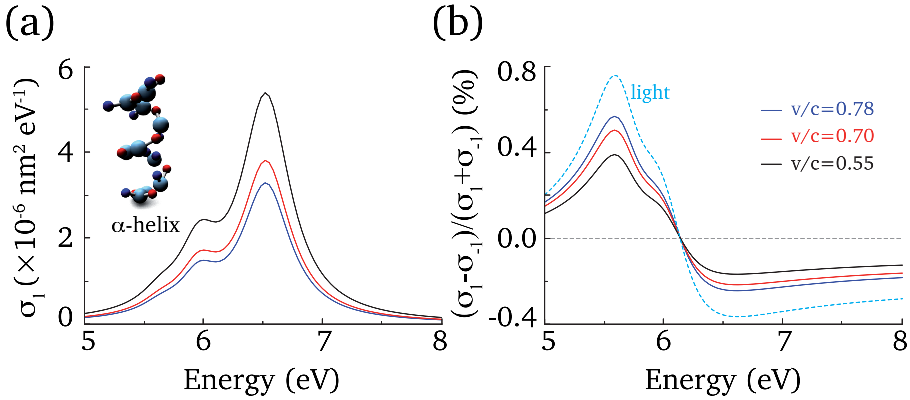

Figure 4.8: Partial inelastic cross-section (a) and normalized dichroism (b) for an α-helix, parametrized as described in Table 4.1. The optical dichroism with circularly polarized light is shown for reference. Different electron energies are represented with the same color code throughout the figure.

entry of the table. The results are obtained for random orientations of the molecule, over which the energy losses are averaged using a sufficiently large number of Euler angles.

The universal curves obtained for the model structure provide a reasonable description of the spectra related to each of the $\alpha-$helix resonances. Interestingly, the observed dichroism has a similar magnitude and profile as the optical dichroism that is obtained by replacing $\sigma_{\pm1}$ by the extinction cross-section of right (+1) and left (−1) circularly polarized light [see Fig. 4.8(b)]. In practice, electron dichroism could be measured in molecular ensembles, which we predict to produce loss intensities comparable with those measured for nanoparticle plasmons[68] when the electrons are passing ~ 1 nm apart from a few tens of molecules.

4.5 Conclusions

In this chapter, we have studied the feasibility of obtaining chiral interactions between vortex electron beams and chiral matter. In particular, we have discussed the case of plasmonic tetramers and biomolecules. We have demonstrated that, unlike light, electrons can engage in dichroic transfer of orbital angular momentum. Besides, since the interaction is mediated by the near-field, electrons can unveil chiral dark modes, which cannot be detected by optical means.

The first part of the chapter has been devoted to establishing a theoretical framework that describes the interaction between vortex electrons and chiral media. Then, we have focused on chiral plasmonic clusters, for which we have predicted large transfers of orbital angular momentum and a remarkably high degree of dichroism in the inelastic interaction. The dichroic spectrum changes sign when mirror imaging the sample, and it disappears in systems that have mirror symmetry with respect to a plane perpendicular to the beam direction. The analysis of the dichroism in the non-retarded limit has demonstrated that all of the modes have a non-negligible contribution to the chiral signal. We have also calculated the torque and force exerted by the electron on the cluster, thus opening a pathway towards a new spectroscopy technique that probes both intrinsic and extrinsic rotational degrees of freedom.

Afterwards, we have analyzed the losses and dichroism of focused electron beams. Due to the sub-nanometer spatial resolution of electron microscopes, this can become a useful tool to map different chiral modes in plasmonic structures, which are important elements of chiral metamaterials. Moreover, we have shown that the strength of the dichroism is strongly dependent on the degree of focusing of the electron beam, and it is maximized when the beam size is comparable to the extension of the probed chiral mode.

Finally, in the last section of this chapter, we have demonstrated that electron vortex beams can resolve the handedness of chiral biomolecules. We have also provided a tutorial description that includes universal curves for model point structures. Chiral electron energy-loss spectroscopy might be a fertile ground for applications in biological and pharmaceutical studies.

To the electron – may it never be of any use to anybody!

Toast at J. J. Thompson's Cavendish Laboratory

5

Electron energy-gain spectroscopy

Electron microscopes play an instrumental role in areas as diverse as cell biology and nanophotonics. Electron energy-loss spectroscopy has proved to be extremely useful for mapping plasmonic excitations with high spatial resolution, although the energy resolution is still poor compared with optical techniques. A strategy to overcome this problem consists in examining energy gains rather than losses experienced by the electron when the sample is subject to external laser irradiation. The so-called electron energy-gain spectroscopy should provide an unprecedented combination of both energy and space resolution.

5.1 Introduction

Nowadays, electron microscopes benefit from an impressive sub-angstrom spatial resolution.[76, 187, 188] Certainly, they have become vital tools for providing extremely detailed images of nanoscopic structures. Moreover, the analysis of energy losses experienced by the electrons upon interaction with the samples adds further details on the chemical composition, electronic structure, and of course, on the optical response of the latter.[189]

Recent experiments performed on a new generation of transmission electron microscopes that are equipped with electron monochromators[78] show an impressive energy resolution (< 0.1 eV). However, the zero-loss peak imposes a clear limit to this resolution, which is not still sufficient to characterize fine spectral features commonly encountered in nanostructures. An alternative method that combines the spatial resolution of electron beams and the energy resolution of optical probes has been suggested based on the analysis of energy gains experienced by the electrons.[190, 191] In this so-called electron energy-gain spectroscopy, electrons that have absorbed energy from an external light source appear on the negative side of the energy-loss spectrum, and the area under an energy gain peak reflects the response of the sample at the illuminating frequency, thus increasing the energy resolution, which is no longer limited by the width of the electron zero-loss peak.

In this context, a crucial advance towards the experimental realization of EEGS has been accomplished in recent years. The group of Prof. Ahmed Zewail was able to observe multiple energy gains and losses in pulsed electrons in coincidence with pulsed laser irradiation.[97, 99] In their pioneering experiment, they managed to obtain images of silver nanowires and carbon nanotubes by analyzing the part of the electron spectrum related to energy gains. The authors also reported time-resolved measurements obtained by modifying the arrival times and relative delay between electron and photon pulses. The multiple energy transfers between the electrons and the samples are now well understood[192–194] and, moreover, the electrons have been shown to undergo a complex evolution involving multiple energy exchanges on the sub-femtosecond time scale.[192]

In this chapter, we explore multiple energy losses and gains undergone by swift electrons interacting with resonant evanescent light fields. The first section is devoted to provide a theoretical framework that allows one to calculate the probability of multiphoton events. The final expressions will be thoroughly used in the remaining part of the chapter. In particular, the second section addresses the proposal of a new spectroscopy technique based upon varying the incoming light frequency and studying the subsequent energy jumps of the electron. We predict remarkably high gain probabilities in the range of a percentage when the electrons are passing near a resonant plasmonic structure under continuous-wave illumination conditions with moderate laser intensities. Additionally, we observe an intriguing fine structure in the dependence of the gain and loss probabilities on the light wavelength, which reveals a complex interplay between multiple plasmon-electron interactions. These results constitute a solid basis for the development of a new spectroscopy technique based upon the analysis of energy gains, capable of rendering information on the optical properties of the sampled resonant nanostructures. We illustrate this concept for noble-metal nanoshells. We conclude this chapter with the development of a simple model to describe EELS, EEGS, and CL in a unified quantum treatment that provides further intuition into the physical mechanisms underlying these spectroscopic techniques.

5.2 Outline of the theory

In this section, we provide theoretical insight about the energy gains and losses experienced by the electron.[192] We employ a semiclassical model in which the quantum mechanical evolution of the electron is solved including its interaction with the external laser field, which is treated classically. [1]

Electron-light interaction

We consider a swift electron moving in the $\hat{\mathbf{z}}$-direction at high velocities. We write the electron-light interaction Hamiltonian as the sum of two different terms, one proportional to the emission and the other to the absorption of one photon, as

$$H_I(z,t) = -\frac{e\hbar}{m_e\omega}\,\left[E_z(z,t) - E_z^*(z,t)\right]\,\frac{\partial}{\partial z}, \tag{5.1}$$

where we have approximated $\mathbf{E}\cdot\nabla \sim E_z\partial_z$. This is indeed a good estimation since the electron momentum along the trajectory is large compared to that associated with the transversal direction, due to the small customary apertures in TEMs (around few milliradians[195]). Therefore, one can then safely neglect the degrees of freedom related to momentum components perpendicular to the beam trajectory.

In the above equation, ω is the central light frequency, and the electric field parallel to the electron beam is described by a temporal Gaussian wave-packet

$$E_z(z,t) = \mathcal{E}_z(z)\,\exp\left[-\mathrm{i}\omega t - (t+\tau)^2/\Delta_p^2\right], \tag{5.2}$$

---

[1] The classical description of the electromagnetic field is well justified when the light pulse contains a large number of photons, as here considered.

where $\sim 2\Delta_p$ is the light pulse duration and τ is the delay between the arrivals of the photon and electron pulses at the position of the sample. The pulse is assumed to be spectrally narrow (*i.e.* $\omega >> \Delta\omega \sim \Delta_p^{-1}$), and the dispersion in the response of the sample over the pulse width can be overlooked.

Electron wave-function

The wave-function of the unperturbed incident electron, with momentum along the $\hat{\mathbf{z}}-$direction $\hbar k_0$, is written as $\psi_0(z,t) = \psi^G_{k_0}(z,t)$, where

$$\psi^G_k(z,t) = \aleph_k \exp\left[ikz - \mathrm{i}\varepsilon_k t - \left(t - z/\mathrm{v}_k\right)^2/\Delta_e^2\right] \tag{5.3}$$

is a Gaussian electron pulse characterized by the following parameters:

- temporal duration $\sim 2\Delta_e$,
- normalization constant $|\aleph_k|^2 = (\sqrt{\pi/2}\Delta_e \mathrm{v}_k)^{-1}$, which is introduced aiming for having only one electron per pulse,
- relativistic electron energy $\hbar\varepsilon_k = c\sqrt{\hbar^2k^2 + m_e^2c^2}$, and corresponding group velocity $\mathrm{v}_k = \partial\varepsilon_k/\partial k$ ($\mathrm{v}_k \sim 0.7c$ for the 200-keV electrons here studied).

The self-consistent electron wave-function resulting from the interaction is readily given by the Lippmann-Schwinger equation as[196, 197]

$$\psi(z,t) = \psi_0(z,t) + \int dz'dt'\; G(z-z',t-t')\, H_I(z',t')\, \psi(z',t'), \tag{5.4}$$

where

$$\mathrm{G}(z-z',t-t') \approx -\frac{\mathrm{i}}{2\pi\hbar}\int dk\; \exp\left[\mathrm{i}k|z-z'| - \mathrm{i}\varepsilon_k(t-t')\right], \tag{5.5}$$

is the one-dimensional electron Green function corresponding to propagation along $\hat{\mathbf{z}}$. We solve Eq. (5.4) by writing the wave-function as a sum over different perturbation orders as

$$\psi(z,t) = \sum_{N=0}^{\infty}(G\cdot H_I)^N\psi_0 \equiv \sum_{N=0}^{\infty}\psi_N(z,t), \tag{5.6}$$

where the dot expresses the convolution operator. The scattering order N represents the number of emission and absorption events sustained by the electron. Precisely, at an order of scattering N, the electron has gained or lost $|L| \leq N$ real photons. We now expand ψ_N in terms of Gaussian waves $\psi^G_{k_L}$ as

$$\psi_N(z,t) = \sum_{L=-N}^{N} \psi^G_{k_L}(z,t)\, F^N_L(z)\, e^{-N(t-z/\mathrm{v}_{k_L}+\tau)^2/\Delta_p^2}, \tag{5.7}$$

where the exponential factor arises from an $N-$order intensity decrease at the time of interaction and k_L is the electron wave-vector after exchanging L real photons. In the non-recoil approximation, $k_L = k_0 + L\omega/\mathrm{v}$. We find an explicit expression for the expansion coefficients $F^N_L(z)$ by induction, using Eqs. (5.1)-(5.7) to write

$$\begin{aligned}\psi_{N+1}(z,t) =& G \cdot H_I\, \psi_N = \qquad (5.8)\\ =& \frac{\mathrm{i}e}{m_e\omega} \sum_{L=-N}^{N} \aleph_{k_L} \int dz' \int dt' \left[\mathcal{E}_z(z')\, I_+ - \mathcal{E}^*_z(z')\, I_-\right]\\ &\times \left(\mathrm{i}k_L + \frac{\partial}{\partial z'}\right) F^N_L(z')\, e^{-(t'-z'/\mathrm{v}_{k_L})^2/\Delta_e^2}\, e^{-N(t'-z'/\mathrm{v}_{k_L}+\tau)^2/\Delta_p^2}\, e^{-(t'+\tau)^2/\Delta_p^2},\end{aligned}$$

where

$$I_\pm = \int \frac{dk}{2\pi}\, e^{\mathrm{i}k|z-z'|}\, e^{\mathrm{i}k_L z'}\, e^{-\mathrm{i}\varepsilon_k(t-t')}\, e^{-\mathrm{i}\varepsilon_{k_L} t'}\, e^{\mp \mathrm{i}\omega t'}.$$

Since the wavelength of a 200-keV electron is only $2\pi/k_0 \approx 2.5\,\mathrm{pm}$, the function $I_\pm$ oscillates fast with $z' > z$ compared to the remaining factors in the integrand of Eq. (5.8). For instance, light fields are nearly constant over distances of several nanometers. Therefore, the contribution of $I_\pm$ to Eq. (5.8) is non-negligible only for $z > z'$, which is the region at which the oscillations of wave-vectors k and k_L are relatively compensated. It is then possible to write

$$I_\pm \approx \exp[\mathrm{i}(k_{L\pm1} z - \varepsilon_{k_{L\pm1}} t \mp \mathrm{i}\omega z'/\mathrm{v})]\; \theta(z-z')\; \delta[z - z' - \mathrm{v}_{k_{L\pm1}}(t-t')].$$

Hence, one is able to easily perform the t' integral of Eq. (5.8) by employing the delta function, and to write ψ_{N+1} as in Eq. (5.7), substituting N by $N+1$. The resulting functions F^{N+1}_L are subject to the recursion relation

$$\begin{aligned}F^{N+1}_L(z) = \frac{e}{m_e \mathrm{v}\, \omega} \int_{-\infty}^{z} dz' \Bigg[&\mathcal{E}_z(z')\, e^{-\mathrm{i}\omega z'/\mathrm{v}} \left(\mathrm{i}\frac{\partial}{\partial z'} - k_L\right) F^N_{L-1}(z')\\ &-\mathcal{E}^*_z(z')\, e^{\mathrm{i}\omega z'/\mathrm{v}} \left(\mathrm{i}\frac{\partial}{\partial z'} - k_L\right) F^N_{L+1}(z')\Bigg],\end{aligned} \tag{5.9}$$

where the starting value is $F^0_0 = 1$ and we define $F^N_L = 0$ for $|L| > N$.

Probability of energy gains and losses

From the time-integral of the electron current ($\mathrm{Im}\{\psi^* \partial_z \psi\}$), one can readily calculate the probability (P_L) that the electron finishes up with momentum centered around $k_L = k_0 + L\omega/\mathrm{v}$, so that it has emitted ($L < 0$) or gained ($L > 0$) an amount of energy corresponding to $|L|$ photons. The time-integral is performed outside the interaction region, where $\mathscr{E}_z \simeq 0$ and the functions of Eq. (5.9) converge to constant values C_L^N. Then, one finds

$$P_L = \sum_{N=|L|}^{\infty} \sum_{N'=|L|}^{\infty} C_L^N \left(C_L^{N'}\right)^* \frac{\exp\left[-\frac{(N+N')\left(\tau/\Delta_p\right)^2}{1+[(N+N')/2]\left(\Delta_e/\Delta_p\right)^2}\right]}{\sqrt{1+\frac{N+N'}{2}\left(\Delta_e/\Delta_p\right)^2}}. \tag{5.10}$$

Remarkably, we notice that the multiphoton probabilities depend on the pulse durations and delay only through the ratios τ/Δ_p and Δ_e/Δ_p. Clearly, a delay in the arrival of photon and electron pulses is translated into a decrease in the effective interaction strength and therefore, it acts as an eraser of the multiphoton probabilities.

5.3 Energy-gain spectroscopy

In this section, a new spectroscopy technique based upon energy gains experienced by the electron is proposed. We focus on the light-frequency dependence of the multiphoton exchange probabilities and discuss the interaction with a plasmonic sample, as we intend to analyze the suitability of EEGS to yield information on its optical response.

Description of the proposed experimental scheme

We consider nanoshells consisting of a silica core ($\epsilon = 2$) coated with either 5 nm of gold or 4 nm of silver. The full diameter of the particle is 100 nm in all cases. The choice of metal thickness is made to feature a spectrally isolated dipole plasmon around 700-800 nm light wavelength. Upon illumination with the laser external field $\mathbf{E}^{ext}$, we approximate the induced electric field in that spectral region by its dominant dipolar component

$$\mathbf{E}(\mathbf{r},\omega) = [k^2\mathbf{p} + (\mathbf{p}\cdot\nabla)\nabla]\,\frac{e^{ikr}}{r}, \tag{5.11}$$

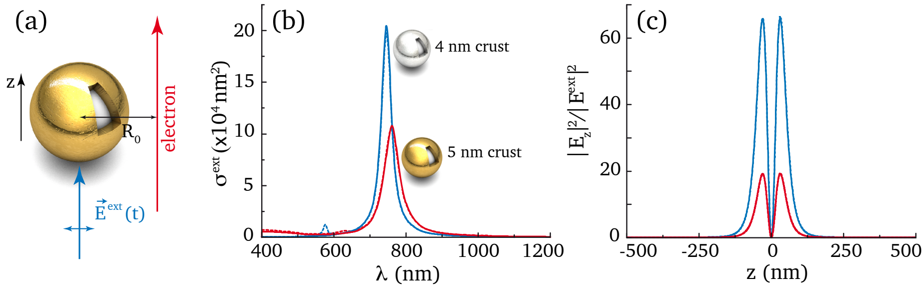

Figure 5.1: (a) Scheme of the system under consideration: a 200-keV electron passes 10-nm away from the surface of a 100-nm nanoshell composed of a silica core coated with a layer of either 5-nm gold (red curves) or 4-nm silver (blue curves). (b) Optical extinction cross-section of the nanoshells. (c) Induced electric field intensity along the $\hat{\mathbf{z}}$ direction as a function of distance along the electron trajectory upon irradiation with light of wavelength λ=762 nm for gold and 745 nm for silver. Solid curves: contribution of the dipole plasmon. Broken curves: full multipolar calculation (nearly indistinguishable from the dipolar contribution).

where $k = \omega/c$ is the light wave-vector and $\mathbf{p} = \alpha(\omega)\mathbf{E}^{ext}$ is the induced dipole moment. Here, we incorporate retardation effects in the polarizability $\alpha(\omega)$ by expressing it in terms of the dipolar Mie coefficient as $\alpha(\omega) = 3t_1^E/2k^3$, where t_1^E finds a closed-form analytical expression for spherical shells.[143, 198] We use a measured frequency-dependent dielectric function for silver and gold[42] to represent the response of the metallic coating of the nanoshells.

Figure 5.1(a) depicts a sketch of the system, for which we assume co-parallel electron and laser beams. Under this configuration, the electron is only sensitive to the induced field, as the incident field is normal to the electron velocity and losses/gains are mediated by the electric field along the beam direction. Similar results are obtained for other light incidence directions and polarization conditions, and although the particle-mediated light-electron coupling strength depends on these parameters, our qualitative conclusions remain unchanged. The coupling strength can be intuitively understood by examining the z-component of the electric field produced by the induced dipole. The extinction cross-section of the nanoshells,

$$\sigma^{\text{ext}}(\omega) = 4\pi k \text{Im}\{\alpha(\omega)\},$$

is displayed by solid curves in Fig. 5.1(b) and shows a prominent near-infrared plasmon that is isolated from other modes of the system (*cf.* solid and dashed curves, with the latter obtained with inclusion of all multipoles;[143] notice that both calculations are in excellent agreement, except for the $\sim$ 580 nm quadrupolar plasmon of silver, which is obviously absent from the dipolar results). We shall recall that only the component of the electric field along z contributes to the photon-electron coupling (*i.e.*, only the induced field contributes). Figure 5.1(c) shows the magnitude of the induced field for illumination at the peak plasmon frequency, which exhibits a clear enhancement with respect to the incident field. Silver nanoshells have larger on-resonance extinction and induced field, which translate into higher multiphoton probabilities, as will be shown hereafter.

Discussion of the multiphoton probabilities

The occupation probability of the electron states changes dramatically by varying the frequency of the incoming light. When the frequency approaches the dipole plasmon resonance of the particle, the near-field intensity is enhanced, and therefore, the interaction with the electron is stronger. We show in Fig. 5.2(a) that the electron is mostly in the elastic or zero-loss channel for low intensities. For higher intensities, this channel is increasingly depleted and shows a dip at the plasmon frequency. This depletion is accompanied by a complex dynamics that results in a sizable population of electron inelastic channels, as shown in Fig. 5.2(b), which oscillates with frequency as a result of interference between multiple plasmon loss and gain processes.

We must stress that the intensity of the external field needed to produce these effects is orders of magnitude lower than that disclosed in previous works,[97,192,193] thanks to the mediation of the particle plasmons, which act as optical amplifiers. In particular, Fig. 5.2(a) shows small but noticeable depletion of the zero-loss channel even for peak laser intensities as low as 10^8- 10^9 Wm^{-2}.

Incidentally, there is a small shift between near and far field resonance frequencies, as previously reported for light scattering from nanoparticles.[199,200] This is clear from Fig. 5.2, where the gray dotted line, representing the plasmon frequency as obtained from the extinction cross-section (far-field), is blue-shifted a few nanometers with respect to the maximum depletion of the elastic electron component. This is a manifestation of the fact that the coupling between photons and electrons is mediated by the near field, which is dominated by evanescent components.

The occupation probability depends on the ratio between the photon and the electron pulse durations (see Fig. 5.3). In the limit of continuous-wave illumination (*i.e.*, when the electron pulse is much shorter than the light pulse), the elastic signal is depleted at low intensities compared to the depletion for pulsed illumination, which can be intuitively understood from the stronger interaction associated with continuous plasmon excitation (*cf.* for example the higher depopulation of the elastic channel for continuous and pulsed illumination in Fig. 5.3). In comparison with gold, the silver nanoshell produces higher depletion of the elastic channel at lower intensities, com-

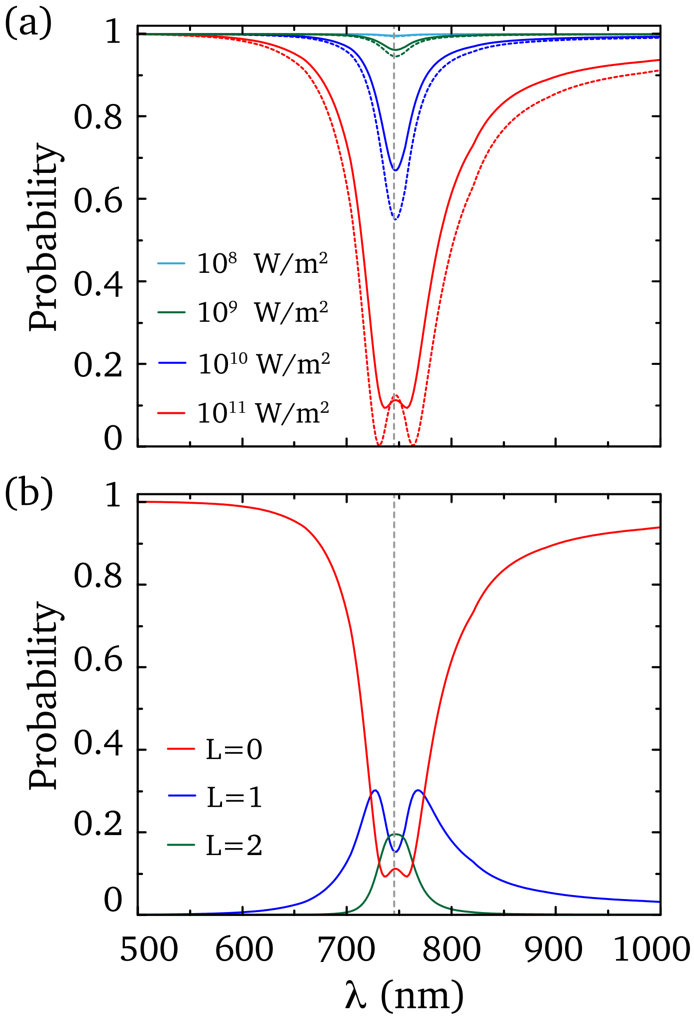

Figure 5.2: Occupation probability of different multiphoton exchange channels as a function of incoming light wavelength for the silver nanoshell considered in Fig. 5.1. (a) Depletion of the elastic channel (L=0) for different intensities under continuous (dashed curves) and pulsed (solid curves) light irradiation. (b) Probabilities of the $L = 0 - 2$ channels for a laser intensity of 10^{11} Wm^{-2}. The electron energy is 200 keV and its impact parameter relative to the particle surface is 10 nm. The electron and laser pulse durations in the solid curves of both panels are $\Delta_e = \Delta_p = 200$ fs. The gray dashed lines show the resonance plasmon wavelength.

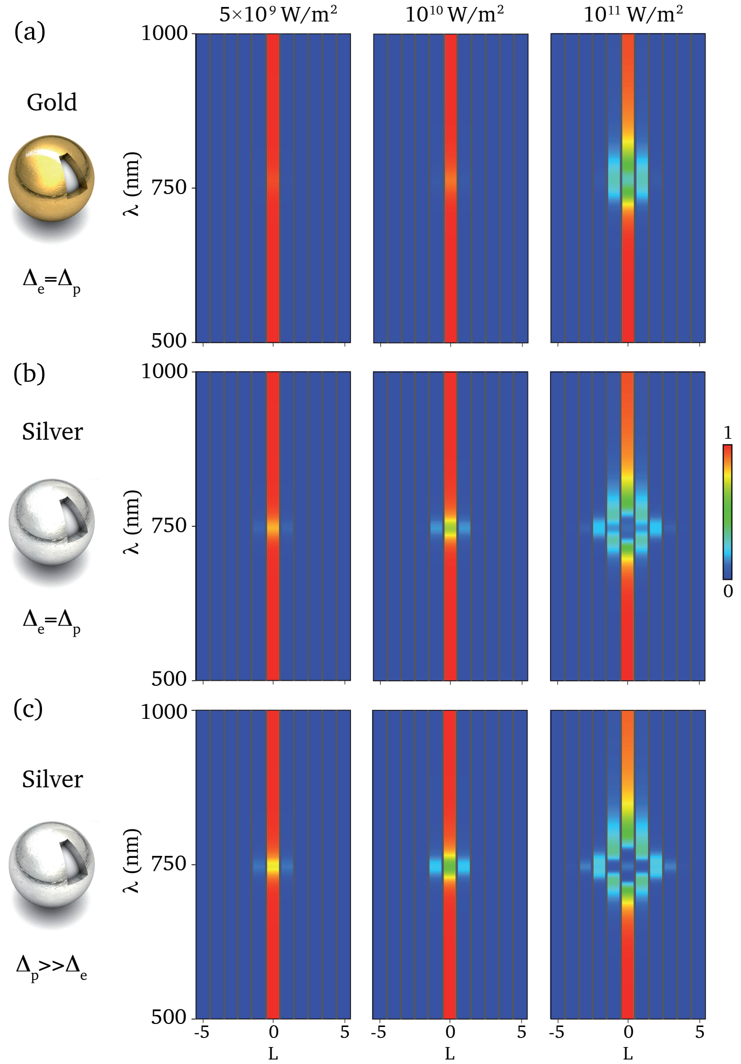

Figure 5.3: Probability of multiphoton emission (L<0) and absorption (L>0) as a function of incoming light wavelength for the net number of exchanged photons L. Each column corresponds to a different level of external light intensity (see upper labels). We present results for (a) a gold nanoshell with $\Delta_e = \Delta_p = 200$ fs, (b-c) a silver nanoshell with (b) $\Delta_e = \Delta_p = 200$ fs and (c) continuous wave illumination. The electron energy is 200 keV and its impact parameter relative to the particle surface is 10 nm.

patible with continuous-wave illumination, and below the damage threshold of the samples. Although quite small to be observable in the density plots, non-negligible multiphoton events appear for intensities as low as $\sim 10^9$ Wm^{-2}.

Comparison of EELS and EEGS spectra

In order to place the above EEGS probabilities in perspective, it is useful to compare them with those of more traditional electron spectroscopies, such as EELS. We show in Fig. 5.4 calculated EEGS and EELS spectra for the same silver nanoshell as in Fig. 5.1.

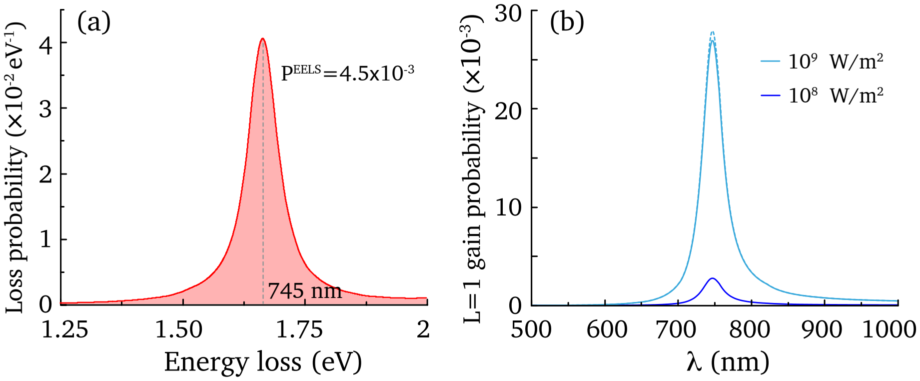

Figure 5.4: Electron energy loss (a) and gain (b) spectra for a 200-keV electron passing 10 nm away from a silver nanoshell. The integral of the EELS probability over the dipole plasmon peak yields $P^{\rm EELS} = 4.5 \times 10^{-3}$, which should be compared with the EEGS probability shown in (b) for different incoming light frequencies under continuous wave illumination. The full solution of Eq. (5.10) (solid curves) is in excellent agreement with the analytical expression of Eq. (5.12) (broken curves) in (b) (nearly indistinguishable).

The probability of exciting one plasmon in EELS is comparable to the probability of gaining or losing (due to stimulation) one photon in EEGS when the nanoshell is illuminated with intensities as low as 10^8 Wm^{-2}, below the damage threshold of the materials involved, thus indicating that this effect is measurable using continuous-wave illumination. Under such low laser-intensity irradiation, single-photon processes dominate the electron-light scattering. Therefore, EEGS probability can be calculated at first order in perturbation theory [or, equivalently, by computing the term F_1^1 taking

$z \to \infty$ in Eq. (5.9)], yielding

$$P_1(\omega) = \left(\frac{e}{\hbar\omega}\right)^2 \left| \int_{-\infty}^{\infty} dz\, e^{-i\frac{\omega}{v}z}\, E_z(\mathbf{R}_0, z, \omega) \right|^2 .$$

A closed-form expression can be derived for dipolar scatterers, which are characterized by the field described by Eq. (5.11). Then, the probability reduces to

$$P_1(\omega) = \left(\frac{2e\omega}{\hbar v^2 \gamma}\right)^2 |\alpha(\omega)|^2 \left[\left| \mathbf{E}^{ext} \cdot \hat{\mathbf{R}}_0 \right|^2 K_1^2\left(\frac{\omega R_0}{v\gamma}\right) + \frac{|\mathbf{E}_z^{ext}|^2}{\gamma^2} K_0^2\left(\frac{\omega R_0}{v\gamma}\right) \right], \quad (5.12)$$

where $\mathbf{R}_0$ is the impact parameter [see Fig. 5.1(a)], K_0 and K_1 are modified Bessel functions, and $\gamma = 1/\sqrt{1 - v^2/c^2}$ is the relativistic Lorentz contraction factor. Incidentally, Fig. 5.4(b) shows excellent agreement between the full numerical results of Eq. (5.10) and the analytical expression resulting from considering only single-photon absorption (*i.e.*, employing the equation above), with only small deviations at high intensities originating in nonlinear multiphoton inelastic scattering.

5.4 Unified analytical quantum model for EELS, EEGS, and CL

Finally, in this section, we formulate a simple quantum model that unifies the description of every electron-based spectroscopies (EELS, EEGS, and CL) and provides further insight into the mechanisms that underlie the energy and momentum exchanges between photons, plasmons, and fast electrons. For simplicity, we consider the sample to be a plasmon-supporting small particle.

We describe photons and plasmons in terms of their annihilation (creation) operators a_i and b_l ($a_i^\dagger$ and $b_l^\dagger$), where i and l label different modes of frequencies ω_i and $\tilde{\omega}_{pl}$, respectively. We consider degenerate plasmons and include their inelastic decay rate Γ_{pl} as an imaginary part in $\tilde{\omega}_{pl} = \omega_{pl} - i\Gamma_{pl}/2$, in the spirit of the quantum jump approximation.[201,202] Likewise, $c_k^\dagger$ (c_k) creates (annihilates) a fast electron of energy $\hbar\epsilon_k$ and momentum $\hbar k\hat{\mathbf{z}}$. We neglect the dynamics of the electron along directions perpendicular to $\hat{\mathbf{z}}$, which, as already stated, is a safe assumption for typical electron beams with small divergence angles. The Hamiltonian of this system is written as

$$H = H_0 + H_{int}, \quad (5.13)$$

where

$$H_0 = \hbar \sum_k \epsilon_k c_k^\dagger c_k + \hbar \sum_i \omega_i a_i^\dagger a_i + \hbar \sum_l \tilde{\omega}_{pl} b_l^\dagger b_l \tag{5.14}$$

is the non-interacting part, whereas the interaction Hamiltonian consists of just two components, $H_{int} = H_{ph-pl} + H_{e-pl}$, because electrons and photons do not directly couple in free space. The photon-plasmon coupling Hamiltonian

$$H_{ph-pl} = -\mathbf{p} \cdot \mathbf{E} \tag{5.15}$$

is expressed in terms of the particle dipole operator

$$\mathbf{p} = \sum_l \mathbf{d}_l \left(b_l^\dagger + b_l \right) = \sum_l d_l \hat{x}_l \left(b_l^\dagger + b_l \right) \tag{5.16}$$

and the quantized electromagnetic field

$$\mathbf{E} = \mathbf{E}^+ + \mathbf{E}^- = \mathrm{i} \sum_i \sqrt{\frac{2\pi\hbar\omega_i}{V}} \hat{\varepsilon}_i \left(a_i - a_i^\dagger \right), \tag{5.17}$$

where V is the mode quantization volume, $\hat{\varepsilon}_i$ is the polarization vector, and the particle is assumed to be at $\mathbf{r} = 0$. We adopt the rotating wave approximation, which allows us to write

$$H_{ph-pl} = -\mathrm{i} \sum_{i,l} g_{il} \left(b_l^\dagger a_i - b_l a_i^\dagger \right), \tag{5.18}$$

with real coupling coefficients

$$g_{il} = \sqrt{\frac{2\pi\hbar\omega_i}{V}} d_l \left(\hat{x}_l \cdot \hat{\varepsilon}_i \right). \tag{5.19}$$

The electron-plasmon interaction Hamiltonian is

$$H_{e-pl} = \sum_{k,k',l} \left(g_{k'kl} c_{k'}^\dagger c_k b_l^\dagger + g_{k'kl}^* c_k^\dagger c_{k'} b_l \right), \tag{5.20}$$

where $g_{kk'l}$ are complex coupling constants given by (see Appendix D)

$$g_{k'kl} = \frac{2e}{\gamma^2 L} d_l \hat{x}_l \cdot \left[-\gamma |k'-k| K_1 \left(\frac{|k'-k| R_0}{\gamma} \right) \hat{\mathbf{R}}_0 + \mathrm{i}(k'-k) K_0 \left(\frac{|k'-k| R_0}{\gamma} \right) \hat{\mathbf{z}} \right]. \tag{5.21}$$

In the above expression, L is the electron quantization length along the beam direction, and $\mathbf{R}_0$ is the impact parameter of the beam relative to the particle [see Fig. 5.1(a)].

The states of the system encompass the tensorial product of electron, photon, and plasmon states. In the initial state, the electron has energy ϵ_{k_0}, the light mode i of the illuminating laser has a population of $N_i >> 1$ photons, and no plasmons are excited:

$$|k_0 N_i 0_l\rangle = |k_0\rangle \otimes |N_i\rangle \otimes |0_l\rangle\,.$$

For low irradiation intensities, the interactions can be treated as perturbations and we solve the evolution up to second order. In this picture, higher order processes involving multiple plasmon excitation produce stimulated emission effects, which are discussed later in this section. At first order in perturbation theory [see Fig. 5.5(a)], two processes are possible: extinction of light by the nanoshell and electron energy loss. At second order, the processes that involve the creation of only one plasmon are CL and EEGS. For the system sketched in Fig. 5.1(a), the probabilities per unit of transferred energy for EELS, EEGS,and CL are

$$\Gamma^{EELS}(\omega) = \frac{4e^2\omega^2}{\pi\hbar^2 \mathrm{v}^4\gamma^2}\left[K_1^2\left(\frac{\omega R_0}{\mathrm{v}\gamma}\right) + \frac{1}{\gamma^2}K_0^2\left(\frac{\omega R_0}{\mathrm{v}\gamma}\right)\right]\mathrm{Im}\{\alpha(\omega)\}, \tag{5.22}$$

$$\Gamma^{EEGS}(\omega) = \frac{8\pi e^2\omega^2}{\hbar^3 \mathrm{v}^4 c\gamma^2}\, I_0\; K_1^2\left(\frac{\omega R_0}{\mathrm{v}\gamma}\right)|\alpha(\omega_i)|^2\delta(\omega-\omega_i), \tag{5.23}$$

$$\Gamma^{CL}(\omega) = \frac{8e^2\omega^5}{3\pi\hbar^2 c^3 \mathrm{v}^4\gamma^2}\left[K_1^2\left(\frac{\omega R_0}{\mathrm{v}\gamma}\right) + \frac{1}{\gamma^2}K_0^2\left(\frac{\omega R_0}{\mathrm{v}\gamma}\right)\right]|\alpha(\omega)|^2, \tag{5.24}$$

which agree with previous results obtained from dielectric theory.[68, 191] In particular, the energy integral of Γ^{EEGS} yields the already anticipated result for the gain probability of an electron upon interaction with a dipolar scatterer given by Eq. (5.12). In the above equations,

$$\alpha(\omega) = \frac{d^2}{\hbar}\frac{1}{\tilde{\omega}_{pl} - \omega}$$

is the particle polarizability, ω_i is the incoming light frequency, and $I_0 = (c/2\pi)|\mathbf{E}^{ext}|^2$ is the light intensity, which as expected, only appears in the photon-assisted process.

In the above, we have discussed rather elementary phenomena in a diagramatic fashion. This basic academic approach can nonetheless be applied to actual experiments, as we can regard the particle and its plasmons as an intermediate coupler

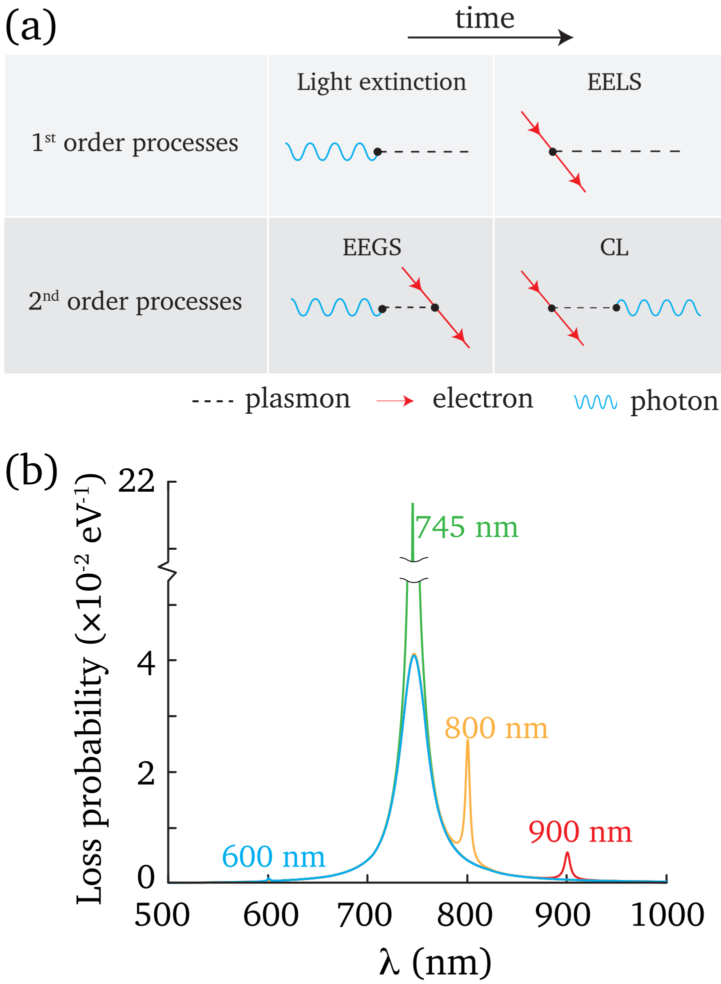

Figure 5.5: (a) Diagrams for all processes involving the creation of one plasmon, up to second order. (b) Electron energy-loss spectra for a 200-keV electron passing 10 nm away from a silver nanoshell, for different incoming light wavelengths under continuous-wave illumination. The light intensity is 10^8 Wm^{-2}.

between the incident photons and the electron, so that a factor proportional to the large number of incident photons N_i (*i.e.*, I_0) pops up in Eq. (5.23). Alternatively, we could have described the laser by a coherent photon state, which excites a coherent plasmon with multiple occupancy.

The inverse process of EEGS, stimulated photon emission into state i, mediated by particle plasmons, has exactly the same probability, but now multiplied by $N_i + 1$ instead of N_i. For large N_i, the stimulated EELS (SEELS) probability is approximately given by Eq. (5.23) (*i.e.*, $N_i + 1 \approx N_i$). Incidentally, EEGS, SEELS, and CL are intimately related to the Einstein coefficients for absorption, stimulated emission and spontaneous emission, respectively.[203] For the single plasmon mode under consideration, the absorption and stimulated emission coefficients are identical, and so are the EEGS and SEELS matrix elements in the limit of large photon numbers.

Figure 5.5(b) shows calculated energy-loss spectra for a silver nanoshell under the conditions of Fig. 5.1(a) based upon Eqs. (5.22)-(5.24), taking into account the SEELS contribution just discussed. The δ function in the latter is slightly broadened for clarity (the actual width of this peak will be essentially limited by both the laser width and the resolution of the energy analyser). Several photon energies around the plasmon peak have been considered, giving rise to substantial contributions comparable to the regular EELS intensity when the light is tuned to the plasmon energy.

5.5 Conclusions

In this chapter, we have studied the interaction of swift electrons with intense induced light fields in nanostructures. The first section has been devoted to reviewing a theoretical formalism in order to analyze multiphoton events experienced by the electron.

The following section has described a new spectroscopy technique, based on varying the external light frequency. In particular, we have shown that the interaction between electrons and illuminated plasmon-supporting nanostructures provides useful information on the sample, with great potential to combine unprecedented space-, energy-, and time-resolutions in a single spectral microscopy technique. Remarkably, the plasmonic enhancement of the induced field leads to large energy gain (and stimulated loss) probabilities using moderate levels of incident light intensity compatible with continuous wave illumination without damaging the samples. Although we have focused on nanoshells because of the tutorial character of the dipolar model, similar conclusions can be also drawn for metallic nanorods, whose plasmons can be tuned by changing their aspect ratio. Actually, the lowest-order dipolar mode of a rod is expected to also produce significant field enhancement that can yield even stronger EEGS signals under continuous-wave illumination conditions.

Finally, we have developed a simple quantum model in order to describe EELS, EEGS, and CL on an equal footing. This formalism provides further intuition into the physical mechanisms underlying these processes.

Electron energy-gain-based microscopy and spectroscopy provide a fertile ground for groundbreaking studies of both the sample's optical response and the temporal evolution of electron pulses interacting with it. Interestingly, EEGS resolution could be extended towards the atomic scale and it could also be employed to characterize biological molecules or even cells. Besides, it could be used to investigate nonlinear optical behaviors. Furthermore, ultrashort photon pulses might be employed to study the time evolution of plasmons. A decrease in the pulse duration of the electron would allow one to investigate the complex evolution that it sustains upon interaction with evanescent light fields. In particular, we envision new experiments that might reveal coherent interference between different electron wave-function components. For instance, interference might arise when illuminating the sample with two-color light, where the absorption of two photons of the fundamental frequency or only one photon corresponding to the second harmonic would result in the same energy gain. In fact, the interesting possibility of interfering losses stimulated by external illumination and inelastic losses has been recently discussed.[204]

In science, it is not speed that is the most important. It is the dedication, the commitment, the interest and the will to know something and to understand it — these are the things that come first.

Eugene Wigner

Conclusions

The interaction between light, matter, and electron beams gives rise to many fascinating phenomena, some of them still not well understood. In this context, the aim of this thesis is twofold: first, to provide theoretical insight about some fundamental issues; second, to propose or confirm experimental work that might lead to technological applications.

In a nutshell, the central results of this thesis are the following:

- **Description of the interaction between rotating particles and light.**

  In Chapter 2, we have derived a theoretical framework that explains how the rotation of a spinning metallic nanoparticle affects its optical response. We have first built a toy-model that is subsequently extended in order to deal with realistic systems. Due to the rotation, the body scatters light inelastically, constituting an example of rotational Doppler shift.

  Moreover, when the frequency of rotation is higher than that of the incoming light, the system becomes superradiant and generates stimulated emission. Although this concept is typically related to quantum physics and population inversion in atoms or molecules, we have demonstrated that a purely classical system also exhibits this behavior. In particular, the stimulated emission is due to a decrease in the rotation velocity of the spinning particle.

  Finally, we have studied the experimental feasibility of such system. According to our calculations, under proper light illumination, the particle acquires remarkable spinning velocities without melting, which opens the door to future experimental realizations.

- **Calculation of the dichroism displayed by synthetic plasmonic chiral nanostructures.**

  Chapter 3 is devoted to providing theoretical insight into experimental results on the dichroism produced by plasmonic chiral tetramers assembled by means of DNA origami. To this purpose, we employed a simple semi-analytical model based upon dipolar interaction between the particles as well as a fully numerical computation that considers all multipolar contributions. The agreement between calculated and experimental data is extremely satisfactory. We have also analyzed the role of plasmonic coupling between the gold spheres that conform the cluster, demonstrating that smaller particle sizes and larger separations lead to fainter CD signals.

  In this experimental collaboration, we have demonstrated that DNA origami assembling provides an avenue towards mass-production of chiral clusters with nanometer accuracy, and revealed that plasmonic field enhancement is critical for achieving strong dichroism.

- **Demonstration of the feasibility of chiral interactions between matter and vortex electron beams.**

  In Chapter 4, we have calculated the energy losses experienced by electron vortex beams when interacting with chiral structures. These beams carry orbital angular momentum and, in contrast to optical vortices, can engage in dichroic activity with chiral matter. In particular, we have estimated that the dichroism can reach very high values for silver chiral clusters, reaching up to 10% of the inelastic signal. Furthermore, we have also examined the chiral interaction between these vortex and biomolecules, which are described by non-orthogonal electric and magnetic dipoles.

  Due to the spatial resolution of electron beams, this chiral spectroscopy technique would provide unprecedented spatial information about chiral plasmonic modes. It would also be possible to observe chiral dark modes, which are not accessible by optical means. Although the realization of the proposed experiment is far from being trivial, this work paves the way towards a new electron spectroscopy with chiral sensitivity.

- **Proposal of a new spectroscopy technique based on photon-induced electron energy gains and losses.**

  In the last chapter of this thesis, we have provided a detailed theory that explains the energy gain and loss events sustained by electrons passing near illuminated nanostructures. In particular, we have calculated the probability of these multiphoton events at different light frequencies, and formulated specific predictions that we understand as the basis of a new spectroscopy with

> nanometer resolution. Energy gain features have been predicted to be observable under continuous wave illumination without damaging the sample. This technique holds great potential for investigating ultrafast screening dynamics and non-linear optical response at the nanometer scale.
>
> The so-called electron energy-gain spectroscopy should provide an unprecedented combination of energy and space resolution, combined with temporal control provided by the light pulse.

To conclude, we expect that this work contributes to further enrich the already exciting field of nanophotonics. Notwithstanding most of the work presented here covers theoretical results, we have also kept in mind experimental realizations together with our collaborators and, moreover, tried to provide new avenues towards the improvement of both light- and electron-based spectroscopies.

APPENDICES

A

Optical torques and forces acting on a small particle

The expressions for the torque and force are obtained from the conservation of linear and angular momentum, respectively, and completely stipulated by Maxwell's stress tensor. In this appendix, we derive analytical expressions for a small particle considered to behave as an electric dipole, placed in vacuum, and illuminated by a monochromatic field.

A.1 Torque

The torque is calculated by computing the flux of the angular-momentum pseudotensor across a spherical surface S of radius r that surrounds the object. The time-averaged torque is

$$\langle \mathbf{M} \rangle = -\int_S \langle \mathbf{T}(\mathbf{r}, t) \times \mathbf{r} \rangle \cdot \hat{\mathbf{r}} \, dS,$$

where $\langle \dots \rangle$ denotes time average, $\hat{\mathbf{r}} = \big(\cos\varphi \sin\theta, \sin\varphi \sin\theta, \cos\theta\big)$ is the vector normal to the surface, and Maxwell's stress tensor reads

$$\mathbf{T}(\mathbf{r},t) = \frac{1}{4\pi}\left[\mathbf{E}(\mathbf{r},t)\otimes\mathbf{E}(\mathbf{r},t) + \mathbf{H}(\mathbf{r},t)\otimes\mathbf{H}(\mathbf{r},t) - \frac{1}{2}\left(|\mathbf{E}(\mathbf{r},t)|^2 + |\mathbf{H}(\mathbf{r},t)|^2\right)\mathbb{1}\right].$$

The electric, $\mathbf{E}(\mathbf{r},t)$, and magnetic, $\mathbf{H}(\mathbf{r},t)$, fields entering the above equations are the total self-consistent ones, which include both the external as well as the scattered fields, and are assumed to be monochromatic (with frequency ω):

$$\mathbf{E}(\mathbf{r},t) = \mathbf{E}(\mathbf{r})\, e^{-\mathrm{i}\omega t} + \mathbf{E}^*(\mathbf{r})\, e^{\mathrm{i}\omega t}, \tag{A.1a}$$

$$\mathbf{H}(\mathbf{r},t) = \mathbf{H}(\mathbf{r})\, e^{-\mathrm{i}\omega t} + \mathbf{H}^*(\mathbf{r})\, e^{\mathrm{i}\omega t}. \tag{A.1b}$$

After performing the prescribed time average of Maxwell stress tensor, we find

$$\langle \mathbf{M} \rangle = -\frac{r^3}{2\pi}\int d\Omega\, \mathrm{Re}\left\{[\mathbf{E}^*(\mathbf{r})\times\hat{\mathbf{r}}][\mathbf{E}(\mathbf{r})\cdot\hat{\mathbf{r}}] + [\mathbf{H}^*(\mathbf{r})\times\hat{\mathbf{r}}][\mathbf{H}(\mathbf{r})\cdot\hat{\mathbf{r}}]\right\}.$$

From now on, we denote the external fields as $\{\mathbf{E}_e(\mathbf{r}), \mathbf{H}_e(\mathbf{r})\}$ and the scattered ones as $\{\mathbf{E}_s(\mathbf{r}), \mathbf{H}_s(\mathbf{r})\}$. Within the dipolar approximation, and for a particle placed at the origin, the external fields are

$$\mathbf{E}_e(\mathbf{r}) = \mathbf{E}_e + r(\hat{\mathbf{r}}\cdot\nabla)\,\mathbf{E}_e, \tag{A.2a}$$

$$\mathbf{H}_e(\mathbf{r}) = \mathbf{H}_e + r(\hat{\mathbf{r}}\cdot\nabla)\,\mathbf{H}_e. \tag{A.2b}$$

where $r = |\mathbf{r}|$, and $\{\mathbf{E}_e, \mathbf{H}_e\}$ are the fields at the particle's position (the origin). The second term yields a zero contribution to the torque. However, it has to be taken into account in the calculation of the force in the following section.

The scattered electric and magnetic fields produced by an electric dipole $\mathbf{p}$ placed at the origin are

$$\mathbf{E}_s(\mathbf{r}) = \frac{e^{ikr}}{r^3}\left\{[(kr)^2 + \mathrm{i}kr - 1]\,\mathbf{p} - [(kr)^2 + 3\mathrm{i}kr - 3]\,\hat{\mathbf{r}}\,(\hat{\mathbf{r}}\cdot\mathbf{p})\right\}, \tag{A.3a}$$

$$\mathbf{H}_s(\mathbf{r}) = \frac{e^{ikr}}{r^2}\mathrm{i}k\,(-\mathrm{i}k + 1)\,(\hat{\mathbf{r}}\times\mathbf{p}), \tag{A.3b}$$

where $k = \omega/c$. The resulting expression for the torque can be then expressed as a sum of three different components,

$$\langle \mathbf{M} \rangle = \langle \mathbf{M}_{e,e} \rangle + \langle \mathbf{M}_{e,s} \rangle + \langle \mathbf{M}_{s,s} \rangle,$$

where $\mathbf{M}_{e,e}$ and $\mathbf{M}_{s,s}$ involve only the external and scattered fields, respectively, and $\mathbf{M}_{e,s}$ arises from the interference between them. The first term results in a null contribution. The second term is

$$\begin{aligned}\langle \mathbf{M}_{e,s} \rangle &= -\frac{r^3}{2\pi}\int d\Omega\ \mathrm{Re}\left\{[\mathbf{E}_s^*(\mathbf{r})\times\hat{\mathbf{r}}][\mathbf{E}_e\cdot\hat{\mathbf{r}}]+[\mathbf{E}_e^*\times\hat{\mathbf{r}}][\mathbf{E}_s(\mathbf{r})\cdot\hat{\mathbf{r}}]\right\} = \\ &= -\frac{1}{2\pi}\mathrm{Re}\left\{\int d\Omega\,[(kr)^2-ikr-1]\,(\mathbf{p}^*\times\hat{\mathbf{r}})(\mathbf{E}_e\cdot\hat{\mathbf{r}})\right\}+ \\ &\quad -\frac{1}{\pi}\ \mathrm{Re}\left\{\int d\Omega\,(1-ikr)(\hat{\mathbf{r}}\cdot\mathbf{p})(\mathbf{E}_e^*\times\hat{\mathbf{r}})\right\}.\end{aligned}$$

Since the integration surface is arbitrary, we choose to evaluate the fields in the near zone ($kr \to 0$). The angular integrals yield

$$\begin{aligned}\int d\Omega\,(\mathbf{p}^*\times\hat{\mathbf{r}})(\mathbf{E}_e\cdot\hat{\mathbf{r}}) &= \frac{4\pi}{3}\,\mathbf{p}^*\times\mathbf{E}_e, \\ \int d\Omega\,(\mathbf{E}_e^*\times\hat{\mathbf{r}})(\mathbf{p}\cdot\hat{\mathbf{r}}) &= \frac{4\pi}{3}\,\mathbf{E}_e^*\times\mathbf{p},\end{aligned}$$

and, therefore, the torque arising from the interference between the external and the scattered fields is given by the cross product of the induced dipole and the external field at the position of the particle:

$$\langle \mathbf{M}_{e,s} \rangle = 2\,\mathrm{Re}\left\{\mathbf{p}^*\times\mathbf{E}_e\right\}. \tag{A.4}$$

The final term, which comprises the interference of the scattered field with itself, reads

$$\begin{aligned}\langle \mathbf{M}_{s,s} \rangle &= -\frac{r^3}{2\pi}\int d\Omega\,\mathrm{Re}\left\{[\mathbf{E}_s^*(\mathbf{r})\times\hat{\mathbf{r}}][\mathbf{E}_s(\mathbf{r})\cdot\hat{\mathbf{r}}]\right\} = \\ &= -\frac{1}{\pi r^3}\mathrm{Re}\left\{[(kr)^2-ikr-1]\,(1-ikr)\int d\Omega\,(\mathbf{p}^*\times\hat{\mathbf{r}})(\hat{\mathbf{r}}\cdot\mathbf{p})\right\}.\end{aligned}$$

Since

$$\int d\Omega\,(\mathbf{p}^*\times\hat{\mathbf{r}})(\hat{\mathbf{r}}\cdot\mathbf{p}) = \frac{4\pi}{3}\mathbf{p}^*\times\mathbf{p},$$

the radiative component of the torque yields

$$\langle \mathbf{M}_{s,s} \rangle = -\frac{4k^3}{3}\ \mathrm{Im}\left\{\mathbf{p}^*\times\mathbf{p}\right\}. \tag{A.5}$$

Finally, recasting the results of Eqs. (A.4) and (A.5), the optical torque acting on a dipolar particle is

$$\langle \mathbf{M} \rangle = 2\left[\mathrm{Re}\left\{\mathbf{p}\times\mathbf{E}_e^*\right\}+\frac{2k^3}{3}\ \mathrm{Im}\left\{\mathbf{p}\times\mathbf{p}^*\right\}\right].$$

A.2 Force

The force acting on a body is calculated by computing the flux of Maxwell's stress tensor across a spherical surface S of radius r that surrounds it. The time-averaged force is

$$\begin{aligned}\langle \mathbf{F} \rangle &= \int_S \langle \mathbf{T}(\mathbf{r},t) \rangle \cdot \, \mathbf{n}(\mathbf{r}) \, dS \\ &= \frac{r^2}{2\pi} \int d\Omega \, \mathrm{Re} \left\{ \mathbf{E}^*(\mathbf{r}) \, [\mathbf{E}(\mathbf{r}) \cdot \hat{\mathbf{r}}] + \mathbf{H}^*(\mathbf{r})[\mathbf{H}(\mathbf{r}) \cdot \hat{\mathbf{r}}] - \frac{1}{2} \left(|\mathbf{E}(\mathbf{r})|^2 + |\mathbf{H}(\mathbf{r})|^2 \right) \hat{\mathbf{r}} \right\}.\end{aligned}$$

As in the previous section, it is possible to separate different contributions to the force depending on their origin. The terms involving only external or induced fields result on a null force. Solely the term that includes the interference between the external and scattered fields gives rise to a non-zero force given by

$$\begin{aligned}\langle \mathbf{F}_{e,s} \rangle = \frac{r^2}{2\pi} \int d\Omega \, \mathrm{Re} \, \{ & \mathbf{E}_e^*(\mathbf{r}) \, [\mathbf{E}_s(\mathbf{r}) \cdot \hat{\mathbf{r}}] + \mathbf{E}_s^*(\mathbf{r}) \, [\mathbf{E}_e(\mathbf{r}) \cdot \hat{\mathbf{r}}] + \mathbf{H}_e^*(\mathbf{r}) \, [\mathbf{H}_s(\mathbf{r}) \cdot \hat{\mathbf{r}}] \\ & + \mathbf{H}_s^*(\mathbf{r}) \, [\mathbf{H}_e(\mathbf{r}) \cdot \hat{\mathbf{r}}] - \mathbf{E}_e^*(\mathbf{r}) \cdot \mathbf{E}_s(\mathbf{r}) \, \hat{\mathbf{r}} - \mathbf{H}_e^*(\mathbf{r}) \cdot \mathbf{H}_s(\mathbf{r}) \, \hat{\mathbf{r}} \}.\end{aligned}$$

Plugging Eqs. (A.2) into the above expression, the terms that produce a non-zero force are

$$\begin{aligned}\langle \mathbf{F}_{e,s} \rangle = & \frac{r^2}{2\pi} \int d\Omega \, \mathrm{Re} \{ \mathbf{H}_s^*(\mathbf{r}) \, (\mathbf{H}_e \cdot \hat{\mathbf{r}}) - \mathbf{H}_s^*(\mathbf{r}) \cdot \mathbf{H}_e \, \hat{\mathbf{r}} \} \\ & + \frac{r^3}{2\pi} \int d\Omega \, \mathrm{Re} \{ [\mathbf{E}_s(\mathbf{r}) \cdot \hat{\mathbf{r}}] \, (\hat{\mathbf{r}} \cdot \nabla) \, \mathbf{E}_e^* + \mathbf{E}_s^*(\mathbf{r}) \, (\hat{\mathbf{r}} \cdot \nabla) \, (\mathbf{E}_e \cdot \hat{\mathbf{r}}) - \mathbf{E}_s^*(\mathbf{r}) \cdot (\hat{\mathbf{r}} \cdot \nabla) \, \mathbf{E}_e \, \hat{\mathbf{r}} \}.\end{aligned}$$

We now follow the same steps as in the previous section. The calculation of the above integrals implies a more involved algebra than that of the previous section and, for the sake of brevity, only final results are shown. These are:

$$\begin{aligned}& \int d\Omega \, \{ \mathbf{H}_s^*(\mathbf{r}) \, (\mathbf{H}_e \cdot \hat{\mathbf{r}}) - \mathbf{H}_s^*(\mathbf{r}) \cdot \mathbf{H}_e \, \hat{\mathbf{r}} \} = -\mathrm{i} \frac{8\pi k}{3r^2} \, (\mathbf{H}_e \times \mathbf{p}^*), \\ & \int d\Omega \, \ [\mathbf{E}_s(\mathbf{r}) \cdot \hat{\mathbf{r}}] \, (\hat{\mathbf{r}} \cdot \nabla) \, \mathbf{E}_e^* = \frac{8\pi}{3r^3} (\mathbf{p} \cdot \nabla) \, \mathbf{E}_e^*, \\ & \int d\Omega \, \ \mathbf{E}_s^*(\mathbf{r}) \, (\hat{\mathbf{r}} \cdot \nabla) \, (\mathbf{E}_e \cdot \hat{\mathbf{r}}) = \frac{4\pi}{5r^3} \left[-\frac{2}{3} \mathbf{p}^* (\nabla \cdot \mathbf{E}_e) + (\mathbf{p}^* \cdot \nabla) \mathbf{E}_e + \sum_j p_j^* \nabla E_{e,j} \right], \\ & \int d\Omega \, \ \mathbf{E}_s^*(\mathbf{r}) \cdot (\hat{\mathbf{r}} \cdot \nabla) \, \mathbf{E}_e \, \hat{\mathbf{r}} = \frac{4\pi}{5r^3} \left[\mathbf{p}^* (\nabla \cdot \mathbf{E}_e) + (\mathbf{p}^* \cdot \nabla) \, \mathbf{E}_e - \frac{2}{3} \sum_j p_j^* \nabla E_{e,j} \right],\end{aligned}$$

where $j = \{x, y, z\}$ and the sums run over Cartesian components.

Gathering all the previous expressions, the optical force reads

$$\langle \mathbf{F} \rangle = \frac{2}{3}\,\mathrm{Re}\left\{2\,(\mathbf{p}\cdot\nabla)\,\mathbf{E}_e^* - \mathbf{p}^*(\nabla\cdot\mathbf{E}_e) + \sum_j p_j^*\nabla E_{e,j}\right\} - \frac{4k}{3}\mathrm{Im}\{\mathbf{p}^*\times\mathbf{H}_e\}.$$

Since $\mathbf{H}_e = -\frac{\mathrm{i}}{k}\nabla\times\mathbf{E}_e$, this reduces to

$$\langle \mathbf{F} \rangle = \frac{2}{3}\,\mathrm{Re}\left\{2\,(\mathbf{p}\cdot\nabla)\,\mathbf{E}_e^* + 2\,\mathbf{p}\times(\nabla\times\mathbf{E}_e^*) - \mathbf{p}(\nabla\cdot\mathbf{E}_e^*) + \sum_j p_j\nabla E_{e,j}^*\right\},$$

or, in index notation and using Einstein summation convention,

$$\langle F_i \rangle = \frac{2}{3}\,\mathrm{Re}\{2\,p_j\partial_j E_{e,i}^* + 2\,\varepsilon_{ijk}p_j\varepsilon_{klm}\partial_l E_{e,m}^* - p_i\partial_j E_{e,j}^* + p_j\partial_i E_{e,j}^*\},$$

where ε_{ijk} is the Levi-Civita tensor, which satisfies $\varepsilon_{ijk}\varepsilon_{klm} = \delta_{il}\delta_{jm} - \delta_{im}\delta_{jl}$. As a result,

$$\langle F_i \rangle = 2\,\mathrm{Re}\{p_j\partial_i E_{e,j}^*\} - \frac{2}{3}\,\mathrm{Re}\{p_i\partial_j E_{e,j}^*\}.$$

The integration volume is a source-free region. Then, $\nabla\cdot\mathbf{E}_e = 0$ and, finally, the optical force is

$$\langle \mathbf{F} \rangle = 2\,\mathrm{Re}\left\{\sum_j p_j\nabla E_j^*\right\}.$$

B

Polarizability tensor and light extinction cross-section of a chiral molecule

In this appendix, we derive expressions for the electric and magnetic polarizabilities of a chiral molecule. Besides, we obtain an equation for the light extinction cross-section by a molecule characterized by this polarizability tensor.

B.1 Polarizability tensor

We consider transitions between the ground $|g\rangle$ and excited $|e\rangle$ quantum states of the molecule, with resonant frequency $\omega_0 = \varepsilon_e - \varepsilon_g$, where ε_e and ε_g are the excited and ground state energies, respectively. The system Hamiltonian H consists of a free term and an interaction term

$$H_{\text{int}} = -\mathbf{p} \cdot \mathbf{E}(t) - \mathbf{m} \cdot \mathbf{H}(t),$$

where $\mathbf{E}(t)$ and $\mathbf{H}(t)$ correspond to the external classical electromagnetic field at the position of the molecule, which for simplicity we consider to be monochromatic,

$$\mathbf{E}(t) = \mathbf{E}\, e^{-\mathrm{i}\omega t} + \mathbf{E}^*\, e^{\mathrm{i}\omega t},$$
$$\mathbf{H}(t) = \mathbf{H}\, e^{-\mathrm{i}\omega t} + \mathbf{H}^*\, e^{\mathrm{i}\omega t}.$$

Our results can be trivially extended to polychromatic fields. The molecule wavefunction is a superposition of ground and excited states,

$$|\psi(t)\rangle = c_g(t)\, e^{-\mathrm{i}\varepsilon_g t}\, |g\rangle + c_e(t)\, e^{-\mathrm{i}\varepsilon_e t}\, |e\rangle\,.$$

Inserting this expresssion in Schrödinger's equation, $\mathrm{i}\hbar\partial_t\, |\psi(t)\rangle = H\, |\psi(t)\rangle$, the coefficients $c_{g,e}(t)$ are found to satisfy the expressions

$$\begin{aligned}
\dot{c}_g(t) =& \frac{\mathrm{i}}{\hbar} c_e(t)\left[\mathbf{p}_{ge}\cdot\mathbf{E}+\mathbf{m}_{ge}\cdot\mathbf{H}\right] e^{-\mathrm{i}(\omega+\omega_0)t} + \frac{\mathrm{i}}{\hbar} c_e(t)\left[\mathbf{p}_{ge}\cdot\mathbf{E}^*+\mathbf{m}_{ge}\cdot\mathbf{H}^*\right] e^{\mathrm{i}(\omega-\omega_0)t},\\
\dot{c}_e(t) =& \frac{\mathrm{i}}{\hbar} c_g(t)\left[\mathbf{p}_{eg}\cdot\mathbf{E}+\mathbf{m}_{eg}\cdot\mathbf{H}\right] e^{-\mathrm{i}(\omega-\omega_0)t} + \frac{\mathrm{i}}{\hbar} c_g(t)\left[\mathbf{p}_{eg}\cdot\mathbf{E}^*+\mathbf{m}_{eg}\cdot\mathbf{H}^*\right] e^{\mathrm{i}(\omega+\omega_0)t},
\end{aligned}$$

where

$$\begin{aligned}
\mathbf{p}_{eg} &= \langle e|\mathbf{p}|g\rangle = -e\,\langle e|\mathbf{r}|g\rangle\,,\\
\mathbf{m}_{eg} &= \langle e|\mathbf{m}|g\rangle = -\frac{e}{2m_e c}\,\langle e|\mathbf{L}|g\rangle = \frac{\mathrm{i}e\hbar}{2m_e c}\,\langle e|\mathbf{r}\times\nabla|g\rangle\,,
\end{aligned} \tag{B.1}$$

are the electric and magnetic transition matrix elements. The linear response polarizabilities are obtained from first-order perturbation theory (setting $c_g = 1$ and $c_e = 0$ in the right-hand side of the above equations). The amplitude of the excited state reduces to

$$c_e(t) = -\frac{1}{\hbar}\frac{\mathbf{p}_{eg}\cdot\mathbf{E}+\mathbf{m}_{eg}\cdot\mathbf{H}}{\omega-\omega_0+\mathrm{i}\gamma_0/2} e^{-\mathrm{i}(\omega-\omega_0)t} + \frac{1}{\hbar}\frac{\mathbf{p}_{eg}\cdot\mathbf{E}^*+\mathbf{m}_{eg}\cdot\mathbf{H}^*}{\omega+\omega_0-\mathrm{i}\gamma_0/2} e^{\mathrm{i}(\omega+\omega_0)t},$$

where γ_0 is an effective decay rate. The expected values of the electric and magnetic dipoles are then

$$\begin{aligned}
\langle\mathbf{p}\rangle &= -\frac{1}{\hbar}\frac{\mathbf{p}_{eg}\cdot\mathbf{E}\,\mathbf{p}_{ge}+\mathbf{m}_{eg}\cdot\mathbf{H}\,\mathbf{p}_{ge}}{\omega-\omega_0+\mathrm{i}\gamma_0/2}\, e^{-\mathrm{i}\omega t} + \frac{1}{\hbar}\frac{\mathbf{p}_{eg}\cdot\mathbf{E}^*\,\mathbf{p}_{ge}+\mathbf{m}_{eg}\cdot\mathbf{H}^*\,\mathbf{p}_{ge}}{\omega+\omega_0-\mathrm{i}\gamma_0/2}\, e^{\mathrm{i}\omega t} + c.c.,\\
\langle\mathbf{m}\rangle &= -\frac{1}{\hbar}\frac{\mathbf{p}_{eg}\cdot\mathbf{E}\,\mathbf{m}_{ge}+\mathbf{m}_{eg}\cdot\mathbf{H}\,\mathbf{m}_{ge}}{\omega-\omega_0+\mathrm{i}\gamma_0/2}\, e^{-\mathrm{i}\omega t} + \frac{1}{\hbar}\frac{\mathbf{p}_{eg}\cdot\mathbf{E}^*\,\mathbf{m}_{ge}+\mathbf{m}_{eg}\cdot\mathbf{H}^*\,\mathbf{m}_{ge}}{\omega+\omega_0-\mathrm{i}\gamma_0/2}\, e^{\mathrm{i}\omega t} + c.c.,
\end{aligned}$$

where $c.c.$ stands for complex conjugate.

We now define the polarizability components from the expression

$$\mathbf{p} = \left[\alpha_{EE}(\omega)\mathbf{E}+\alpha_{EM}(\omega)\mathbf{H}\right]\, e^{-\mathrm{i}\omega t} + c.c., \tag{B.2a}$$

$$\mathbf{m} = \left[\alpha_{ME}(\omega)\mathbf{E} + \alpha_{MM}(\omega)\mathbf{H}\right]\ e^{-\mathrm{i}\omega t} + c.c. \tag{B.2b}$$

Taking into account the hermiticity of **p** and **m**, we finally obtain the 6×6 generalized polarizability matrix

$$\mathbb{\alpha} = \begin{bmatrix} \alpha_{EE} & \alpha_{EM} \\ \alpha_{ME} & \alpha_{MM} \end{bmatrix}, \tag{B.3}$$

where

$$\alpha_{EE}(\omega) = \frac{1}{\hbar}\left[\frac{1}{\omega_0 - \omega - \mathrm{i}\gamma_0/2} + \frac{1}{\omega_0 + \omega + \mathrm{i}\gamma_0/2}\right]\mathbf{p}_{ge} \otimes \mathbf{p}_{eg}, \tag{B.4a}$$

$$\alpha_{MM}(\omega) = \frac{1}{\hbar}\left[\frac{1}{\omega_0 - \omega - \mathrm{i}\gamma_0/2} + \frac{1}{\omega_0 + \omega + \mathrm{i}\gamma_0/2}\right]\mathbf{m}_{ge} \otimes \mathbf{m}_{eg}, \tag{B.4b}$$

$$\alpha_{EM}(\omega) = \frac{1}{\hbar}\left[\frac{1}{\omega_0 - \omega - \mathrm{i}\gamma_0/2} - \frac{1}{\omega_0 + \omega + \mathrm{i}\gamma_0/2}\right]\mathbf{p}_{ge} \otimes \mathbf{m}_{eg}, \tag{B.4c}$$

$$\alpha_{ME}(\omega) = -\alpha_{EM}^{T}(\omega). \tag{B.4d}$$

Notice that the dichroic response originates in the crossed electric-magnetic terms α_{EM} and α_{ME}. Therefore, only non-orthogonal electric and magnetic dipoles produce chirality. It is thus convenient to express the dipole elements in terms of the strength of the electric dipole and the projection of the magnetic dipole over the electric one,[146]

$$\begin{aligned} |\mathbf{p}_{ge}| &= e r_{ge}, \\ (\mathbf{p}_{ge} \cdot \mathbf{m}_{eg})/|\mathbf{p}_{ge}| &= -\frac{\mathrm{i} e \omega_0 r_{eg} r_0}{2c}. \end{aligned}$$

B.2 Extinction cross-section

Extinction of light by a particle can occur in two different ways, either by absorption or by scattering. The rate at which a particle absorbs and scatters energy is computed from the flux of the time-averaged Poynting vector through a surface S that encloses the particle, and is given by[46]

$$W^{ext} = -\int_S \langle\, \mathbf{S}_{e,s} \,\rangle \cdot \hat{\mathbf{r}}\, dS,$$

where $\mathbf{S}_{e,s}$ arises from the interference between the external and the scattered fields and, for a monochromatic wave, reads

$$\langle\, \mathbf{S}_{e,s}\,\rangle = \frac{c}{2\pi}\mathrm{Re}\big\{\mathbf{E}_e(\mathbf{r}) \times \mathbf{H}_s^*(\mathbf{r}) + \mathbf{E}_s(\mathbf{r}) \times \mathbf{H}_e^*(\mathbf{r})\big\}.$$

For a plane wave, the extinction cross-section is simply $\sigma^{ext} = W^{ext}/I$, where the light intensity is $I = c|E_e|^2/2\pi$. As in Appendix A, we denote the external fields as $\{\mathbf{E}_e(\mathbf{r}), \mathbf{H}_e(\mathbf{r})\}$ and the scattered ones as $\{\mathbf{E}_s(\mathbf{r}), \mathbf{H}_s(\mathbf{r})\}$. The extinction cross-section is then

$$\begin{aligned}\sigma^{ext}(\omega) =& -\frac{1}{|\mathbf{E}_e|^2}\int_S \mathrm{Re}\big\{\mathbf{E}_e(\mathbf{r}) \times \mathbf{H}_s^*(\mathbf{r}) + \mathbf{E}_s(\mathbf{r}) \times \mathbf{H}_e^*(\mathbf{r})\big\} \cdot \hat{\mathbf{r}}\, dS \\ =& -\frac{1}{|\mathbf{E}_e|^2}\int_S \mathrm{Re}\big\{\mathbf{E}_e(\mathbf{r}) \cdot [\mathbf{H}_s^*(\mathbf{r}) \times \hat{\mathbf{r}}] + \mathbf{H}_e(\mathbf{r}) \cdot [\hat{\mathbf{r}} \times \mathbf{E}_s^*(\mathbf{r})]\big\}\, dS.\end{aligned}$$

Within the dipolar approximation, we can perform a Taylor expansion on the external fields as in Eq. (A.2). Therefore,

$$\begin{aligned}\sigma^{ext}(\omega) =& -\frac{r^2}{|\mathbf{E}_e|^2}\int d\Omega\, \mathrm{Re}\big\{\mathbf{E}_e \cdot [\mathbf{H}_s^*(\mathbf{r}) \times \hat{\mathbf{r}}] + \mathbf{H}_e \cdot [\hat{\mathbf{r}} \times \mathbf{E}_s^*(\mathbf{r})]\big\} \\ & -\frac{r^3}{|\mathbf{E}_e|^2}\int d\Omega\, \mathrm{Re}\big\{(\hat{\mathbf{r}}\cdot\nabla)\mathbf{E}_e \cdot [\mathbf{H}_s^*(\mathbf{r}) \times \hat{\mathbf{r}}] + (\hat{\mathbf{r}}\cdot\nabla)\mathbf{H}_e \cdot [\hat{\mathbf{r}} \times \mathbf{E}_s^*(\mathbf{r})]\big\},\end{aligned} \tag{B.5}$$

where the scattered fields generated by an electric and a magnetic dipole yield

$$\begin{aligned}\mathbf{E}_s(\mathbf{r}) =& \frac{e^{ikr}}{r^3}\big\{[(kr)^2 + ikr - 1]\,\mathbf{p} - [(kr)^2 + 3ikr - 3]\,\hat{\mathbf{r}}\,(\hat{\mathbf{r}}\cdot\mathbf{p})\big\} \\ & -\frac{e^{ikr}}{r^2}\, ik(1 - ikr)(\hat{\mathbf{r}} \times \mathbf{m}), \\ \mathbf{H}_s(\mathbf{r}) =& \frac{e^{ikr}}{r^3}\big\{[(kr)^2 + ikr - 1]\,\mathbf{m} - [(kr)^2 + 3ikr - 3]\,\hat{\mathbf{r}}\,(\hat{\mathbf{r}}\cdot\mathbf{m})\big\} \\ & +\frac{e^{ikr}}{r^2}\, ik(1 - ikr)(\hat{\mathbf{r}} \times \mathbf{p}),\end{aligned}$$

and $k = \omega/c$. Plugging the above expressions into Eq. (B.5), the resulting angular integrals are:

$$\int d\Omega\, \mathrm{Re}\{\mathbf{E}_e \cdot [\mathbf{H}_s^*(\mathbf{r}) \times \hat{\mathbf{r}}]\} = -\frac{8\pi k}{3r^2}\, \mathrm{Im}\{\mathbf{p} \cdot \mathbf{E}_e^*\},$$

$$\int d\Omega\, \mathrm{Re}\{\mathbf{H}_e \cdot [\hat{\mathbf{r}} \times \mathbf{E}_s^*(\mathbf{r})]\} = -\frac{8\pi k}{3r^2}\, \mathrm{Im}\{\mathbf{m} \cdot \mathbf{H}_e^*\},$$

$$\int d\Omega\, \mathrm{Re}\{(\hat{\mathbf{r}} \cdot \nabla)\, \mathbf{E}_e \cdot [\mathbf{H}_s^*(\mathbf{r}) \times \hat{\mathbf{r}}]\} = -\frac{4\pi k}{3r^2}\, \mathrm{Im}\{\mathbf{m} \cdot \mathbf{H}_e^*\},$$

$$\int d\Omega\, \mathrm{Re}\{(\hat{\mathbf{r}} \cdot \nabla)\, \mathbf{H}_e^* \cdot [\hat{\mathbf{r}} \times \mathbf{E}_s(\mathbf{r})]\} = -\frac{4\pi k}{3r^2}\, \mathrm{Im}\{\mathbf{p} \cdot \mathbf{E}_e^*\}.$$

Finally, gathering all the above terms, the extinction cross-section of the molecule reduces to

$$\sigma^{ext}(\omega) = \frac{4\pi k}{|\mathbf{E}_e|^2}\, \mathrm{Im}\left\{\mathbf{p} \cdot \mathbf{E}_e^* + \mathbf{m} \cdot \mathbf{H}_e^*\right\}.$$

C

Electromagnetic Green tensors of clusters and chiral molecules

We derive an expression for the Green tensor of a cluster consisting of small particles that can be described by their dipolar response. Moreover, we obtain the Green tensor of a medium that contains a chiral molecule, characterized by non-orthogonal electric and magnetic dipoles.

C.1 Electromagnetic Green tensor of a small-particle cluster

The electromagnetic Green tensor $\mathcal{G}$ describes the response of a structure to external sources. More precisely, we define it in frequency space ω through the relation

$$\mathbf{E}(\mathbf{r},\omega)=\frac{\mathrm{i}}{\omega}\int d^3\mathbf{r}'\,\mathcal{G}(\mathbf{r},\mathbf{r}',\omega)\cdot\mathbf{j}(\mathbf{r}',\omega) \tag{C.1}$$

between an external current density $\mathbf{j}(\mathbf{r},\omega)$ and the electric field that it generates. We intend to obtain a general expression for $\mathcal{G}$ in the presence of small particles placed at positions $\mathbf{r}_j$, in vacuum, and described through their common polarizability $\alpha(\omega)$.

First, we note that the current associated with an individual dipole $\mathbf{p}_j$ at position $\mathbf{r}_j$ is $-\mathrm{i}\omega\mathbf{p}_j\delta(\mathbf{r}-\mathbf{r}_j)$, so that according to Eq. (C.1) the electric field produced by that dipole reduces to

$$\mathcal{G}^0(\mathbf{r}-\mathbf{r}_j,\omega)\cdot\mathbf{p}_j, \tag{C.2}$$

where we have defined

$$\mathcal{G}^0(\mathbf{r},\omega)=\left(k^2\mathbb{1}+\nabla\otimes\nabla\right)\frac{e^{\mathrm{i}kr}}{r} \tag{C.3}$$

as the vacuum Green tensor. For a particle cluster, we can write the self-consistent dipole at particle j in response to an externally applied field $\mathbf{E}_j^{\mathrm{ext}}=\mathbf{E}^{\mathrm{ext}}(\mathbf{r}_j,\omega)$ as

$$\mathbf{p}_j=\alpha\left(\mathbf{E}_j^{\mathrm{ext}}+\sum_{j'\neq j}\mathcal{G}^0_{jj'}\cdot\mathbf{p}_{j'}\right), \tag{C.4}$$

where we have taken into account the field produced at $\mathbf{r}_j$ by dipoles other than j and

$$\mathcal{G}^0_{jj'}=\mathcal{G}^0(\mathbf{r}_j-\mathbf{r}_{j'},\omega).$$

In matrix notation, with matrix indices running over the three Cartesian directions for each and all of the particles j, Eq. (C.4) can be recast as

$$\mathbf{p}=\frac{\mathbf{1}}{\alpha^{-1}-\mathcal{G}^0}\cdot\mathbf{E}^{\mathrm{ext}}. \tag{C.5}$$

Now, considering the external field

$$\mathbf{E}_j^{\mathrm{ext}}=\frac{\mathrm{i}}{\omega}\int d^3\mathbf{r}\,\mathcal{G}^0(\mathbf{r}_j-\mathbf{r},\omega)\cdot\mathbf{j}(\mathbf{r},\omega) \tag{C.6}$$

produced by current $\mathbf{j}(\mathbf{r},\omega)$, calculating the self-consistently induced dipoles from Eq. (C.4), and summing the dipole fields given by Eq. (C.2), we finally obtain an expression identical to Eq. (C.1) with

$$\mathcal{G}(\mathbf{r},\mathbf{r}',\omega)=\sum_{jj'}\mathcal{G}^0(\mathbf{r}-\mathbf{r}_j,\omega)\cdot\left(\frac{\mathbf{1}}{\alpha^{-1}-\mathcal{G}^0}\right)_{jj'}\cdot\mathcal{G}^0(\mathbf{r}_{j'}-\mathbf{r}',\omega). \tag{C.7}$$

C.2 Green tensor of a chiral molecule

We now derive the electromagnetic Green tensor in the presence of a chiral particle (e.g., the molecule considered in Appendix B). Generalizing Eq. (C.1), we write the response of the particle to electric and magnetic external current densities, $\mathbf{j}_E$ and $\mathbf{j}_M$, as

$$\begin{aligned}\mathbf{E}(\mathbf{r},\omega) &= \frac{\mathrm{i}}{\omega}\int d^3\mathbf{r}'\,\mathcal{G}_{EE}(\mathbf{r},\mathbf{r}',\omega)\cdot\mathbf{j}_E(\mathbf{r}',\omega)+\frac{\mathrm{i}}{\omega}\int d^3\mathbf{r}'\,\mathcal{G}_{EM}(\mathbf{r},\mathbf{r}',\omega)\cdot\mathbf{j}_M(\mathbf{r}',\omega),\\ \mathbf{H}(\mathbf{r},\omega) &= \frac{\mathrm{i}}{\omega}\int d^3\mathbf{r}'\,\mathcal{G}_{ME}(\mathbf{r},\mathbf{r}',\omega)\cdot\mathbf{j}_E(\mathbf{r}',\omega)+\frac{\mathrm{i}}{\omega}\int d^3\mathbf{r}'\,\mathcal{G}_{MM}(\mathbf{r},\mathbf{r}',\omega)\cdot\mathbf{j}_M(\mathbf{r}',\omega).\end{aligned}$$

The currents associated with individual electric and magnetic dipoles, $\mathbf{p}$ and $\mathbf{m}$, placed at position $\mathbf{r}_0$ are

$$\begin{aligned}\mathbf{j}_E(\mathbf{r},\omega) &= -\mathrm{i}\,\omega\,\mathbf{p}\,\delta(\mathbf{r}-\mathbf{r}_0),\\ \mathbf{j}_M(\mathbf{r},\omega) &= -\mathrm{i}\,\omega\,\mathbf{m}\,\delta(\mathbf{r}-\mathbf{r}_0),\end{aligned}$$

so that the electric and magnetic fields produced by these dipoles reduce to

$$\mathbf{E}(\mathbf{r},\omega) = \mathcal{G}^0_{EE}(\mathbf{r}-\mathbf{r}_0,\omega)\cdot\mathbf{p}+\mathcal{G}^0_{EM}(\mathbf{r}-\mathbf{r}_0,\omega)\cdot\mathbf{m}, \tag{C.8a}$$

$$\mathbf{H}(\mathbf{r},\omega) = \mathcal{G}^0_{ME}(\mathbf{r}-\mathbf{r}_0,\omega)\cdot\mathbf{p}+\mathcal{G}^0_{MM}(\mathbf{r}-\mathbf{r}_0,\omega)\cdot\mathbf{m}, \tag{C.8b}$$

where

$$\begin{aligned}&\mathcal{G}^0_{EE}(\mathbf{r}-\mathbf{r}_0,\omega) = \mathcal{G}^0_{MM}(\mathbf{r}-\mathbf{r}_0,\omega) = \mathcal{G}^0(\mathbf{r}-\mathbf{r}_0,\omega),\\ &\mathcal{G}^0_{EM}(\mathbf{r}-\mathbf{r}_0,\omega) = -\mathcal{G}^0_{ME}(\mathbf{r}-\mathbf{r}_0,\omega) = -\frac{1}{ik}\nabla\times\mathcal{G}^0(\mathbf{r}-\mathbf{r}_0,\omega),\end{aligned} \tag{C.9}$$

and $\mathcal{G}^0(\mathbf{r},\mathbf{r}',\omega)$ is the vacuum Green tensor defined by Eq. (C.3).

We can now write the dipoles induced by an external field using the polarizability as defined by Eqs. (B.2), which can be combined with Eqs. (C.8) to write the induced electric and magnetic fields as

$$\begin{bmatrix}\mathbf{E}(\mathbf{r},\omega)\\ \mathbf{H}(\mathbf{r},\omega)\end{bmatrix} = \frac{\mathrm{i}}{\omega}\int d^3\mathbf{r}'\,\mathcal{G}(\mathbf{r},\mathbf{r}',\omega)\cdot\begin{bmatrix}\mathbf{j}_E(\mathbf{r}',\omega)\\ \mathbf{j}_M(\mathbf{r}',\omega)\end{bmatrix}. \tag{C.10}$$

Finally, the induced Green tensor is a 6 × 6 matrix,

$$\mathcal{G}(\mathbf{r},\mathbf{r}',\omega) = \tag{C.11}$$

$$= \begin{bmatrix} \mathcal{G}_{EE}(\mathbf{r},\mathbf{r}',\omega) & \mathcal{G}_{EM}(\mathbf{r},\mathbf{r}',\omega) \\ \mathcal{G}_{ME}(\mathbf{r},\mathbf{r}',\omega) & \mathcal{G}_{MM}(\mathbf{r},\mathbf{r}',\omega) \end{bmatrix}$$

$$= \begin{bmatrix} \mathcal{G}^0_{EE}(\mathbf{r}-\mathbf{r}_0,\omega) & \mathcal{G}^0_{EM}(\mathbf{r}-\mathbf{r}_0,\omega) \\ \mathcal{G}^0_{ME}(\mathbf{r}-\mathbf{r}_0,\omega) & \mathcal{G}^0_{MM}(\mathbf{r}-\mathbf{r}_0,\omega) \end{bmatrix} \cdot \alpha \cdot \begin{bmatrix} \mathcal{G}^0_{EE}(\mathbf{r}_0-\mathbf{r}',\omega) & \mathcal{G}^0_{EM}(\mathbf{r}_0-\mathbf{r}',\omega) \\ \mathcal{G}^0_{ME}(\mathbf{r}_0-\mathbf{r}',\omega) & \mathcal{G}^0_{MM}(\mathbf{r}_0-\mathbf{r}',\omega) \end{bmatrix}, \tag{C.12}$$

where α is the polarizability tensor defined by Eq. (B.3)

D

Derivation of EELS, EEGS, and CL probabilities

In this appendix, we provide a detailed calculations for the expressions appearing in last section of Chapter 5.

D.1 Electron-plasmon coupling

The electron-plasmon coupling constants are derived by using a model Hamiltonian consisting of a free part

$$H_0 = \hbar \sum_l \tilde{\omega}_{pl} b_l^\dagger b_l + \hbar \sum_k \epsilon_k \left|k\right\rangle \left\langle k\right| ,$$

where $|k\rangle$ represents an electron of momentum $\hbar k\hat{\mathbf{z}}$ and energy $\hbar\epsilon_k$, and an electron-plasmon interaction term

$$H_{e-pl} = -\mathbf{p} \cdot \mathbf{E}_c,$$

where $\mathbf{p} = \sum_l d_l(b_l^+ + b_l)\hat{x}_l$ is the particle dipole operator and $\mathbf{E}_c$ is the electron Coulomb field. Given that relativistic electron velocities are typically employed in electron microscopes (e.g., v $\approx 0.7c$ for 200 keV electrons), we include retardation corrections in what follows. In the electron rest frame (primed quantities), the Coulomb field reduces to

$$\mathbf{E}'_c(\mathbf{r}') = e\nabla' \frac{1}{r'}$$

at the particle position $\mathbf{r}'$. We now change to the lab frame through the customary transformation $\mathbf{R}' = -\mathbf{R}$, $z' = -\gamma z$, $\mathbf{E}_{\mathbf{R}} = \gamma \mathbf{E}_{\mathbf{R}'}$, and $E_z = E'_z$, which leads to

$$\mathbf{E}_c = -e\left(\gamma \nabla_R, \frac{1}{\gamma}\partial_z\right)\frac{1}{|(\mathbf{R}, \gamma z)|}.$$

In Fourier space, the Hamiltonian becomes

$$H_{e-pl} = -\sum_{k,k',l} d_l(b_l^+ + b_l)\hat{x}_l \cdot \langle k' \mid \mathbf{E}_c \mid k\rangle \left|k'\right\rangle \left\langle k\right|,$$

where

$$\langle k' \mid \mathbf{E}_c \mid k\rangle = \int d\mathbf{r} d\mathbf{r}' \langle k' \mid r'\rangle \langle r' \mid \mathbf{E}_c \mid r\rangle \langle r \mid k\rangle .$$

Using a suitable electron wave function[68] $\langle r \mid k\rangle = L^{-1/2}\varphi_\perp(\mathbf{R})e^{ikz}$, where L is the quantization length along $\hat{\mathbf{z}}$, approximating $|\varphi_\perp(\mathbf{R})|^2 \approx \delta(\mathbf{R}-\mathbf{R}_0)$ for a well focused electron, and considering the momentum representation of the Coulomb interaction

$$\frac{1}{r} = \frac{1}{\pi}\int dq_z\, K_0(|q_z|R)\, e^{iq_z z},$$

we find

$$\langle k' \mid \mathbf{E}_c \mid k\rangle = -\frac{2e}{\gamma^2 L}\left[-\gamma|q_z|K_1\left(\frac{|q_z|R_0}{\gamma}\right)\hat{R}_0 + iq_z K_0\left(\frac{|q_z|R_0}{\gamma}\right)\hat{z}\right]$$

with $q_z = k' - k$, and from here,

$$H_{e-pl} = \frac{2e}{\gamma^2 L}\sum_{k,k',l} d_l(b_l^+ + b_l)\hat{x}_l \cdot \left[-\gamma|q_z|K_1\left(\frac{|q_z|R_0}{\gamma}\right)\hat{R}_0 + iq_z K_0\left(\frac{|q_z|R_0}{\gamma}\right)\hat{z}\right]\left|k'\right\rangle\left\langle k\right| . \tag{D.1}$$

Finally, comparing Eqs. (5.20) and (D.1), and using the correspondence $c_{k'}^+\left|\phi\right\rangle \longleftrightarrow \left|k'\right\rangle$ and $\left\langle\phi\right| c_k \longleftrightarrow \left\langle k\right|$, where $\left\langle\phi\right|$ is the electron vacuum state, we readily obtain Eq. (5.21).

D.2 Derivation of EELS, EEGS, and CL probabilities

Starting from the Hamiltonian model of Eqs. (5.13)-(5.21), we provide here detailed derivations of the probabilities given by Eqs. (5.22)-(5.24).

D.2.1 First order processes

Light extinction

This process is mediated by H_{ph-pl} and the final state corresponds to one lost photon and one excited plasmon in mode l: $|k_0\,(N-1)_i\,1_l\rangle$. The transition rate from the initial state to all possible final states with an excited plasmon is given by

$$\begin{aligned}\Gamma^{ext} &= \frac{2\pi}{\hbar^2}\sum_l |\,\langle k_0(N-1)_i 1_l|\,H_{ph-pl}\,|k_0 N_i 0_l\rangle\,|^2\delta(\tilde{\omega}_{pl}-\omega_i)\\ &= \frac{2\pi}{\hbar^2}N\sum_l |g_{il}|^2\delta(\tilde{\omega}_{pl}-\omega_i)\\ &= \frac{4\pi^2 N\omega_i}{\hbar V}\sum_l |d_l(\hat{x}_l\cdot\varepsilon_i)|^2\delta(\tilde{\omega}_{pl}-\omega_i)\\ &= \frac{4d^2\pi N\omega_i}{\hbar V}\mathrm{Im}\left\{\frac{1}{\tilde{\omega}_{pl}-\omega_i}\right\},\end{aligned}$$

where we have assumed a spherically symmetric particle $[d_l = d$ and $\sum_l (\hat{\varepsilon}_i\cdot\hat{x}_l)^2 = 1]$. We have implicitly defined $\delta(\tilde{\omega}_{pl}-\omega_i) = (1/\pi)\mathrm{Im}\{\frac{1}{\tilde{\omega}_{pl}-\omega_i}\}$, and the imaginary part comes from $\tilde{\omega}_{pl}$ through the plasmon width Γ_{pl}. Now, computing the light intensity as $I_0 = (c/2\pi)\langle\mathbf{E}^-\mathbf{E}^+\rangle = c\hbar\omega_i N/V$,[203] we find the extinction cross-section

$$\sigma^{ext}(\omega) = \frac{\hbar\omega_i\Gamma^{ext}}{I_0} = \frac{4\pi\omega_i}{c}\mathrm{Im}\left\{\frac{d^2}{\hbar}\frac{1}{\tilde{\omega}_{pl}-\omega_i}\right\},$$

which corresponds to an effective polarizability given by

$$\alpha(\omega_i) = \frac{d^2}{\hbar}\frac{1}{\tilde{\omega}_{pl}-\omega_i}.$$

This expression is used in the following sections.

Electron energy loss

This process is mediated by H_{e-pl} and the final state corresponds to an electron that has lost energy $\epsilon_{k_0} - \epsilon_k > 0$ to excite the plasmon mode l: $|kN_i 1_l\rangle$. The probability of losing the energy of one plasmon is given by

$$\begin{aligned}
P^{EELS} &= \frac{2\pi}{\hbar^2} \frac{L}{\mathrm{v}} \sum_l |\langle kN_i 1_l| H_{e-pl} |k_0 N_i 0_l\rangle|^2 \delta(\epsilon_k - \epsilon_{k_0} + \tilde{\omega}_{pl}) \\
&= \frac{2\pi}{\hbar^2} \frac{L}{\mathrm{v}} \sum_l |g_{kk_0 l}|^2 \delta(\epsilon_k - \epsilon_{k_0} + \tilde{\omega}_{pl}) \\
&= \frac{8e^2 d^2}{\hbar^2 \mathrm{v} L \gamma^2} |k - k_0|^2 \left[K_1^2 \left(\frac{|k - k_0| R_0}{\gamma} \right) + \frac{1}{\gamma^2} K_0^2 \left(\frac{|k - k_0| R_0}{\gamma} \right) \right] \mathrm{Im} \left\{ \frac{1}{\epsilon_k - \epsilon_{k_0} + \tilde{\omega}_{pl}} \right\},
\end{aligned}$$

where the transition rate has been multiplied by the interaction time L/v and we again consider a spherical particle. From here, we find the EELS probability per unit of energy loss $\hbar\omega$ as

$$\Gamma^{EELS}(\omega) = \frac{1}{\hbar} \sum_k P^{EELS} \delta(\epsilon_k - \epsilon_{k_0} + \omega).$$

Finally, using the prescription $\sum_k \to (L/2\pi) \int dk$ and working in the non-recoil approximation [*i.e.*, $\epsilon_k - \epsilon_{k_0} \approx (k - k_0)\mathrm{v}$], we obtain Eq. (5.22) for the EELS probability.

D.2.2 Second order processes

Electron energy gain

This corresponds to the process [see Fig. 5.5(a)]

$$|k_0\, N_i\, 0_l\rangle \xrightarrow{H_{ph-pl}} |k_0\, (N-1)_i\, 1_l\rangle \xrightarrow{H_{e-pl}} |k\, (N-1)_i\, 0_l\rangle\,,$$

the probability of which is given by

$$\begin{aligned}
P^{EEGS} =& \frac{2\pi}{\hbar^4} \frac{L}{\mathrm{v}} \left| \sum_l \frac{\langle k(N-1)_i 0_l| H_{e-pl} |k_0 (N-1)_i 1_l\rangle \langle k_0 (N-1)_i 1_l| H_{ph-pl} |k_0 N_i 0_l\rangle}{\omega_i - \tilde{\omega}_{pl}} \right|^2 \\
& \times \delta(\epsilon_k - \epsilon_{k_0} - \omega_i).
\end{aligned}$$

Noticing that

$$\begin{aligned}
\langle k\,(N-1)_i\,0_l|\,H_{e-pl}\,|k_0\,(N-1)_i\,1_l\rangle &= g_{kk_0l},\\
\langle k_0\,(N-1)_i\,1_l|\,H_{ph-pl}\,|k_0\,N_i\,0_l\rangle &= -\mathrm{i}\sqrt{N}g_{il},
\end{aligned}$$

and taking into account the light incidence and polarization conditions [see Fig. 5.1(a)], we find

$$\begin{aligned}
P^{EEGS} &= \frac{2\pi NL}{\hbar^4 \mathrm{v}}\left|\frac{\sum_l g_{il}g_{kk_0l}}{\omega_i-\tilde{\omega}_{pl}}\right|^2 \delta(\epsilon_k-\epsilon_{k_0}-\omega_i)\\
&= \frac{16\pi^2 d^4 e^2}{\hbar^4 \mathrm{v} L c\gamma^2}\, I_0\ |k-k_0|^2 K_1^2\left(\frac{|k-k_0|R_0}{\gamma}\right)\frac{1}{|\omega_i-\tilde{\omega}_{pl}|^2}\delta(\epsilon_k-\epsilon_{k_0}-\omega_i)\\
&= \frac{16\pi^2 e^2}{\hbar^2 \mathrm{v} L c\gamma^2}\, I_0\ |k-k_0|^2 K_1^2\left(\frac{|k-k_0|R_0}{\gamma}\right)|\alpha(\omega_i)|^2\delta(\epsilon_k-\epsilon_{k_0}-\omega_i).
\end{aligned}$$

Finally, Eq. (5.23) directly follows from evaluating the EEGS probability per unit of transferred energy, $\Gamma^{EEGS}(\omega) = \hbar^{-1}\sum_k P^{EEGS}\delta(\epsilon_k-\epsilon_{k_0}-\omega)$.

Cathodoluminescence

The electron loses energy and excites a plasmon that afterwards radiates to all possible light modes. The corresponding CL process [see Fig. 5.5(a)]

$$|k_0\,N_i\,0_l\rangle \xrightarrow{H_{e-pl}} |k\,N_i\,1_l\rangle \xrightarrow{H_{ph-pl}} |k\,N_i\,1_j\,0_l\rangle$$

has probability

$$P^{CL} = \frac{2\pi}{\hbar^4}\frac{L}{\mathrm{v}}\sum_j\left|\sum_l \frac{\langle kN_i1_j0_l|\,H_{ph-pl}\,|kN_i1_l\rangle\,\langle kN_i1_l|\,H_{e-pl}\,|k_0N_i0_l\rangle}{\epsilon_{k_0}-\epsilon_k-\tilde{\omega}_{pl}}\right|^2\delta(\epsilon_k-\epsilon_{k_0}+\omega_j).$$

Proceeding as above, with:

$$\begin{aligned}
\langle k\,N_i\,1_j\,0_l|\,H_{ph-pl}\,|k\,N_i\,1_l\rangle &= \mathrm{i}g_{jl},\\
\langle k\,N_i\,1_l|\,H_{e-pl}\,|k_0\,N_i\,0_l\rangle &= g_{kk_0l},
\end{aligned}$$

we obtain

$$P^{CL} = \frac{2\pi L}{\hbar^4 \mathrm{v}}\sum_j\left|\frac{\sum_l g_{jl}g_{kk_0l}}{\epsilon_{k_0}-\epsilon_k-\tilde{\omega}_{pl}}\right|^2\delta(\epsilon_k-\epsilon_{k_0}+\omega_j).$$

The sum over all the possible radiated modes j involves summing over both polarizations σ_j and wave-vectors $\mathbf{k}_j = k_j(\sin\theta\cos\varphi, \sin\theta\sin\varphi, \cos\theta)$. Choosing the two independent linear polarization vectors as $\hat{\theta}$ and $\hat{\varphi}$ and taking $\hat{R}_0 = \hat{x}$, we find

$$\sum_{\sigma_j}\left|\sum_l g_{jl}g_{kk_0l}\right|^2 = \frac{8\pi d^4e^2\hbar\omega_j}{VL^2\gamma^2}|k-k_0|^2\left[K_1^2\left(\frac{|k-k_0|R_0}{\gamma}\right)(\sin^2\varphi+\cos^2\theta\cos^2\varphi)\right.$$
$$\left. + \frac{1}{\gamma^2}K_0^2\left(\frac{|k-k_0|R_0}{\gamma}\right)\sin^2\theta\right],$$

and from here, using the customary prescription $\sum_{\mathbf{k}_j} \longrightarrow (V/(2\pi)^3c^3)\int d\Omega\int \omega_j^2 d\omega_j$, we obtain

$$P^{CL} = \frac{16d^4e^2}{3\hbar^3\text{v}Lc^3\gamma^2}\left|\frac{k-k_0}{\epsilon_{k_0}-\epsilon_k-\tilde{\omega}_{pl}}\right|^2(\epsilon_{k_0}-\epsilon_k)^3$$
$$\times\left[K_1^2\left(\frac{|k-k_0|R_0}{\gamma}\right)+\frac{1}{\gamma^2}K_0^2\left(\frac{|k-k_0|R_0}{\gamma}\right)\right].$$

Finally, Eq. (5.24) is directly given by substituting this expression in the spectrally resolved CL probability, $\Gamma^{CL}(\omega) = \hbar^{-1}\sum_k P^{CL}\delta(\epsilon_k-\epsilon_{k_0}+\omega)$.

List of publications and contributions to conferences

The research performed during the development of this thesis has led to the following publications and contributions to international conferences:

Articles on which the thesis is based

1. **Dichroism in the interaction between vortex electron beams, plasmons, and molecules**.
   Ana Asenjo-Garcia and F. Javier García de Abajo.
   Physical Review Letters, **113**, 066102 (2014).
2. **Plasmon electron energy gain spectroscopy**.
   Ana Asenjo-Garcia and F. Javier García de Abajo.
   New Journal of Physics **15**, 103021 (2013).
3. **Three-dimensional plasmonic chiral tetramers assembled by DNA Origami**.
   Xibo Shen, Ana Asenjo-Garcia, Qing Liu, Qiao Jiang, F. Javier García de Abajo, Na Liu, and Baoquan Ding.
   Nano Letters **13**, 2128 (2013).
4. **Stimulated light emission and inelastic scattering by a classical linear system of rotating particles**.
   Ana Asenjo-Garcia, Alejandro Manjavacas, and F. Javier García de Abajo.
   Physical Review Letters **106**, 213601 (2011).

Articles related to the thesis

1. **Hot-electron dynamics in plasmon-supporting nanoparticles**.
   Ana Asenjo-Garcia and F. Javier García de Abajo.
   In preparation.
2. **3D plasmonic chiral colloids**.
   Xibo Shen, Pengfei Zhan, Anton Kuzyk, Qing Liu, Ana Asenjo-Garcia, Hui Zhang, F. Javier García de Abajo, Alexander Govorov, Baoquan Ding, and Na Liu.
   Nanoscale **6**, 2077 (2014).
3. **Alternating plasmonic nanoparticle heterochains made by polymerase chain reaction and their optical properties**.
   Yuan Zhao, Liguang Xu, Luis M. Liz-Marzán, Hua Kuang, Wei Ma, Ana Asenjo-Garcia, F. Javier García de Abajo, Nicholas A. Kotov, Libing Wang, and Chuanlai Xu.
   The Journal of Physical Chemistry Letters **4**, 641 (2013).

4. **Magnetic polarization in the optical absorption of metallic nanoparticles**.
   Ana Asenjo-Garcia, Alejandro Manjavacas, V. Myroshnychenko, and F. Javier García de Abajo.
   Optics Express **20**, 28142 (2012).

5. **Multiphoton absorption and emission by interaction of swift electrons with evanescent light fields**.
   F. Javier García de Abajo, Ana Asenjo-Garcia, and Mathieu Kociak.
   Nano Letters **10**, 1859 (2010).

Contributions to international conferences

- *Chirality in the interaction between plasmons, light, and vortex electron beams*.
  Ana Asenjo-Garcia, and F. Javier García de Abajo.
  SPIE Optics+Photonics, San Diego, United States. August 25-29, 2013. Oral contribution.

- *Chirality in the interaction between plasmons, light, and vortex electron beams*.
  Ana Asenjo-Garcia, and F. Javier García de Abajo.
  PIERS, Stockholm, Sweden. August 12-15, 2013. Oral contribution.

- *Electron-beam interaction with plasmon fields: A new enhanced electron spectral microscopy*.
  Ana Asenjo-Garcia, and F. Javier García de Abajo.
  PIERS, Stockholm, Sweden. August 12-15, 2013. Oral contribution.

- *Electron-beam interaction with plasmon evanescent fields: A new enhanced electron spectral microscopy*.
  Ana Asenjo-Garcia, and F. Javier García de Abajo.
  NFO, San Sebastian, Spain. September 3-7, 2012. Oral contribution.

- *Importance of magnetic polarization in the absorption of metallic nanoparticles*.
  Ana Asenjo-Garcia, A. Manjavacas, V. Myroshnychenko, and F. Javier García de Abajo.
  SPIE Optics+Photonics, San Diego, United States. August 21-25, 2011. Oral contribution.

- *Exotic properties of spinning particles metamaterials*.
  Ana Asenjo-Garcia, A. Manjavacas, and F. Javier García de Abajo.
  SPIE Optics+Photonics, San Diego, United States. August 21-25, 2011. **Invited talk**.

- *Dominant effect of magnetic polarization in the absorption of common metallic nanoparticles*.
  Ana Asenjo-Garcia, A. Manjavacas, V. Myroshnychenko, and F. Javier García de Abajo.
  ICNP, Shanghai, China. May 22-26, 2011. Oral contribution.
- *Dynamics of rotating nanoparticles under external illumination*.
  Ana Asenjo-Garcia, A. Manjavacas, and F. Javier García de Abajo.
  SPIE Optics+Photonics, San Diego, United States. August 1-5, 2010. Oral contribution.

Additionally, the work performed during the thesis has led to 12 poster contributions presented by the author.

Bibliography

[1] C. Baudelaire, *Les fleurs du mal (Les correspondances)*, Poulet-Malassis, Paris (1857). (see p. 13)

[2] J. C. Maxwell, *Treatise on Electricity and Magnetism*, Dover, New York (1891). (see p. 14)

[3] J. D. Jackson, *Classical Electrodynamics*, Wiley, New York (1999). (see pp. 15, 36, and 43)

[4] J. Schwinger, L. L. Deraad, K. A. Milton, and W-Y. Tsai, *Classical Electrodynamics*, Perseus Books, Massachusetts (1998). (see p. 16)

[5] A. Ashkin, *Acceleration and trapping of particles by radiation pressure*, Phys. Rev. Lett. **24**, 156–159 (1970). (see pp. 16 and 34)

[6] A. Ashkin and J. M. Dziedzic, *Optical trapping and manipulation of viruses and bacteria*, Science **235**, 1517–1520 (1987). (see p. 16)

[7] J. R. Moffitt, Y. R. Chemla, S. B. Smith, and C. Bustamante, *Recent advances in optical tweezers*, Annu. Rev. Biochem. **77**, 205–228 (2008). (see p. 16)

[8] J. Liphardt, S. Dumont, S. B. Smith, I. Tinoco Jr., and C. Bustamante, *Equilibrium information from nonequilibrium measurements in an experimental test of Jarzynski's equality*, Science **296**, 1832–1835 (2002). (see p. 16)

[9] E. Roldan, I. A. Martinez, J. M. R. Parrondo, and D. Petrov, *Universal features in the energetics of symmetry breaking*, Nat. Phys., doi:10.1038/nphys2940. (see p. 16)

[10] J. P. Torres and L. Torner, *Twisted photons*, Wiley-VCH, Weinheim (2011). (see p. 16)

[11] J. H. Poynting, *The wave motion of a revolving shaft, and a suggestion as to the angular momentum in a beam of circularly polarised light*, Proc. R. Soc. A **82**, 560–7 (1909). (see p. 16)

[12] R. A. Beth, *Mechanical detection and measurement of the angular momentum of light*, Phys. Rev. **50**, 115–125 (1936). (see pp. 16 and 34)

[13] B. A. Garetz, *Angular Doppler effect*, J. Opt. Soc. Am. Lett. **71**, 609–611 (1981). (see pp. 16, 34, and 40)

[14] M. P. J. Lavery, F. C. Speirits, S. M. Barnett, and M. J. Padgett, *Detection of a spinning object using light's orbital angular momentum*, Science **341**, 537–540 (2013). (see p. 16)

[15] E. Serabyn, D. Mawet, and R. Burruss, *An image of an exoplanet separated by two diffraction beamwidths from a star*, Nature **464**, 1018–1020 (2010). (see p. 16)

[16] A. Mair, A. Vaziri, G. Weihs, and A. Zeilinger, *Entanglement of the orbital angular momentum states of photons*, Nature **412**, 313–316 (2001). (see p. 16)

[17] G. Molina-Terriza, J. P. Torres, and L. Torner, *Management of the angular momentum of light: Preparation of photons in multidimensional vector states of angular momentum*, Phys. Rev. Lett. **88**, 013601 (2002). (see p. 16)

[18] R. Fickler, R. Lapwkiewicz, W. N. Plick, M. Krenn, C. Schaeff, S. Ramelow, and A. Zeilinger, *Quantum entanglement of high angular momenta*, Science **338**, 640–643 (2012). (see p. 16)

[19] G. H. Wagniere, *On chirality and the universal asymmetry*, Wiley VCH, Zurich (2007). (see p. 16)

[20] T. D. Lee and C. N. Yang, *Question of parity conservation in weak interactions*, Phys. Rev. **104**, 254–258 (1956). (see p. 16)

[21] C. S. Wu, E. Ambler, R. W. Howard, D. D. Hoppes, and R. P. Hudson, *Experimental test of parity conservation in beta decay*, Phys. Rev. **105**, 1413–1415 (1957). (see p. 16)

[22] Y. Saitoh and H. Hyuga, *Homochirality: Symmetry breaking in systems driven far from equilibrium*, Rev. Mod. Phys. **85**, 603 (2013). (see p. 17)

[23] F. J. D. Arago, *Note on a remarkable phenomenon experienced by light rays on their passage through certain transparent materials, and on other new optical phenomena*, Mem. Sci. Math. Inst. **12**, 93–134 (1811). (see p. 17)

[24] J. B. Biot, *Note on a new type of oscillation that molecules of light experience when traversing certain crystals*, Mem. Sci. Math. Inst. **12**, 1–372 (1812). (see p. 17)

[25] J. S. Toll, *Causality and the dispersion relation: logical foundations*, Phys. Rev. **104**, 1760–1770 (1956). (see p. 17)

[26] C. Cohen-Tannoudji, J. Dupont-Roc, and G. Grynberg, *Photons and Atoms - Introduction to Quantum Electrodynamics*, Wiley-Interscience, New York (1997). (see p. 17)

[27] L. Rosenfeld, *Quantum mechanical theory of the optical activity of liquids and gasses*, Z. Phys. **52**, 161–174 (1928). (see p. 18)

[28] N. Berova, K. Nakanishi, and R. W. Woody, *Circular dichroism: Principles and applications*, VCH, New York (1994). (see pp. 18, 58, and 86)

[29] L. D. Barron, *Molecular Ligth Scattering and Optical Activity*, Wiley-VCH, Weinheim (2004). (see pp. 18, 19, and 76)

[30] D. B. Amabilino, *Chirality at the Nanoscale*, Wiley-VCH, Weinheim (2009). (see pp. 18, 19, and 76)

[31] S. M. Barnett, R. P. Cameron, and A. M. Yao, *Duplex symmetry and its relation to the conservation of optical helicity*, Phys. Rev. A **86**, 013845 (2012). (see p. 19)

[32] Z. Fan and A. O. Govorov, *Plasmonic circular dichroism of chiral metal nanoparticle assemblies*, Nano Lett. **10**, 2580–2587 (2010). (see pp. 19 and 60)

[33] A. Kuzyk, R. Schreiber, Z. Fan, G. Pardatscher, E.-M. Roller, A. Högele, F. C. Simmel, A. O. Govorov, and T. Liedl, *DNA-based self-assembly of chiral plasmonic nanostructures with tailored optical response*, Nature **483**, 311–314 (2012). (see pp. 19, 52, 61, and 71)

[34] L. Landau, *On the theory of a Fermi liquid*, Sov. Phys. JETP **8**, 70–74 (1957). (see p. 19)

[35] P. Coleman, *Introduction to many-body physics*, Cambridge University Press, Cambridge (2012). (see p. 19)

[36] G. F. Giuliani and G. Vignale, *Quantum theory of the electron liquid*, Cambridge University Press, Cambridge (2005). (see p. 19)

[37] D. Pines and P. Nozières, *The Theory of Quantum Liquids*, W. A. Benjamin, Inc., New York (1966). (see p. 19)

[38] L. Marton, J. A. Simpson, H. A. Fowler, and N. Swanson, *Plural scattering of 20-keV electrons in aluminum*, Phys. Rev. **126**, 182–192 (1962). (see p. 20)

[39] R. H. Ritchie, *Plasma losses by fast electrons in thin films*, Phys. Rev. **106**, 874–881 (1957). (see p. 20)

[40] C. J. Powell and J. B. Swan, *Origin of the characteristic electron energy losses in aluminum*, Phys. Rev. **115**, 869–875 (1959). (see pp. 20 and 25)

[41] L. Novotny and B. Hecht, *Principles of Nano-Optics*, Cambridge University Press, New York (2006). (see pp. 21 and 43)

[42] P. B. Johnson and R. W. Christy, *Optical constants of the noble metals*, Phys. Rev. B **6**, 4370–4379 (1972). (see pp. 21, 22, 28, 47, 58, 71, and 97)

[43] S. A. Maier, *Plasmonics: Fundamentals and Applications*, Springer, New York (2007). (see p. 23)

[44] H. Raether, *Surface Plasmons on Smooth and Rough Surfaces and on Gratings*, Springer Tracks in Modern Physics. Springer-Verlag, Berlin (1988). (see p. 23)

[45] G. Mie, *Beiträge zur optik trüber medien, speziell kolloidaler metallösungen*, Ann. Phys. (Leipzig) **25**, 377–445 (1908). (see pp. 23 and 57)

[46] C. F. Bohren and D. R. Huffman, *Absorption and Scattering of Light by Small Particles*, Wiley-Interscience, New York (1983). (see pp. 23 and 123)

[47] H. C. van de Hulst, *Light Scattering by Small Particles*, Dover, New York (1981). (see pp. 23, 43, and 57)

[48] V. Myroshnychenko, J. Rodríguez-Fernández, I. Pastoriza-Santos, A. M. Funston, C. Novo, P. Mulvaney, L. M. Liz-Marzán, and F. J. García de Abajo, *Modelling the optical response of gold nanoparticles*, Chem. Soc. Rev. **37**, 1792–1805 (2008). (see pp. 24 and 43)

[49] A. Asenjo-Garcia, A. Manjavacas, V. Myroshnychenko, and F. J. García de Abajo, *Magnetic polarization in the optical absorption of metallic nanoparticles*, Opt. Express **20**, 28142–28152 (2012). (see p. 24)

[50] S. Abadalejo, R. Gomez-Medina, L. S. Froufe-Perez, H. Marinchio, R. Carminati, J. F. Torrado, G. Armelles, A. Garcia-Martin, and J. J. Saenz, *Radiative corrections to the polarizability tensor of an electrically small anisotropic dielectric particle*, Opt. Express **18**, 3556 (2010). (see p. 25)

[51] D. E. Chang, A. S. Sörensen, P. R. Hemmer, and M. D. Lukin, *Quantum optics with surface plasmons*, Phys. Rev. Lett. **97**, 053002 (2006). (see p. 25)

[52] D. E. Chang, A. S. Sörensen, E. A. Demler, and M. D. Lukin, *A single-photon transistor using nanoscale surface plasmons*, Nat. Phys. **3**, 807–812 (2007). (see p. 25)

[53] J. S. Fakonas, H. Lee, Y. A. Kelaita, and H. Atwater, *Two-plasmon quantum interference*, Nat. Photon. **8**, 317–320 (2014). (see p. 25)

[54] R. W. Heeres, L. P. Kouwenhoven, and V. Zwiller, *Quantum interference in plasmonic circuits*, Nat. Nanotech. **8**, 719–722 (2013). (see p. 25)

[55] K. R. Catchpole and A. Polman, *Plasmonic solar cells*, Opt. Express **16**, 21793–21800 (2008). (see p. 25)

[56] H. A. Atwater and A. Polman, *Plasmonics for improved photovoltaic devices*, Nat. Mater. **9**, 205–213 (2010). (see p. 25)

[57] F. J. García-Vidal and J. B. Pendry, *Collective theory for surface enhanced Raman scattering*, Phys. Rev. Lett. **77**, 1163–1166 (1996). (see p. 25)

[58] H. Xu, E. J. Bjerneld, M. Käll, and L. Börjesson, *Spectroscopy of single hemoglobin molecules by surface enhanced Raman scattering*, Phys. Rev. Lett. **83**, 4357–4360 (1999). (see p. 25)

[59] J. N. Anker, W. P. Hall, O. Lyandres, N. C. Shah, J. Zhao, and R. P. Van Duyne, *Biosensing with plasmonic nanosensors*, Nat. Mater. **7**(6), 442–453 (2008). (see p. 25)

[60] D. P. O'Neal, L. R. Hirsch, N. J. Halas, J. D. Payne, and J. L. West, *Photo-thermal tumor ablation in mice using near infrared-absorbing nanoparticles*, Cancer Lett. **209**, 171–176 (2004). (see p. 25)

[61] C. Loo, A. Lowery, N. J. Halas, J. L. West, and R. Drezek, *Inmunotargeted nanoshells for integrated cancer imaging and therapy*, Nano Lett. **5**, 709–711 (2005). (see p. 25)

[62] A. M. Gobin, M. H. Lee, N. J. Halas, W. D. James, R. A. Drezek, and J. L. West, *Near-infrared resonant nanoshells for combined optical imaging and photothermal cancer therapy*, Nano Lett. **7**, 1929–1934 (2007). (see p. 25)

[63] E. Rutherford, *The scattering of alpha and beta rays by matter and the structure of the atom*, Philos. Mag. **6**, 21 (1911). (see p. 25)

[64] C. Shull, *Early development of neutron scattering*, Rev. Mod. Phys. **67**, 753–757 (1995). (see p. 25)

[65] R. B. Pettit, J. Silcox, and R. Vincent, *Measurement of surface-plasmon dispersion in oxidized aluminum films*, Phys. Rev. B **11**, 3116–3123 (1975). (see p. 25)

[66] P. E. Batson, *Damping of bulk plasmons in small aluminum spheres*, Solid State Commun. **34**, 477–480 (1980). (see p. 25)

[67] J. Nelayah, M. Kociak, O. Stéphan, F. J. García de Abajo, M. Tencé, L. Henrard, D. Taverna, I. Pastoriza-Santos, L. M. Liz-Marzán, and C. Colliex, *Mapping*

surface plasmons on a single metallic nanoparticle, Nat. Phys. **3**, 348–353 (2007). (see pp. 25 and 84)

[68] F. J. García de Abajo, *Optical excitations in electron microscopy*, Rev. Mod. Phys. **82**, 209–275 (2010). (see pp. 25, 27, 47, 69, 80, 84, 89, 104, and 132)

[69] M. Kociak, O. Stephan, A. Gloter, L. F. Zagonel, L. H. G. Tizei, M. Tence, K. March, J. D. Blazit, Z. Mahfoud, A. Losquin, S. Meuret, and C. Colliex, *Seeing and measuring in colours: Electron microscopy and spectroscopies applied to nano-optics*, C. R. Physique **15**, 158–175 (2014). (see p. 26)

[70] F. J. García de Abajo and A. Howie, *Relativistic electron energy loss and electron-induced photon emission in inhomogeneous dielectrics*, Phys. Rev. Lett. **80**, 5180–5183 (1998). (see p. 28)

[71] F. J. García de Abajo, *Relativistic description of valence energy losses in the interaction of fast electrons with clusters of dielectrics: Multiple-scattering approach*, Phys. Rev. B **60**, 6103–6112 (1999). (see p. 28)

[72] M. W. Chu, V. Myroshnychenko, C. H. Chen, J. P. Deng, C. Y. Mou, and F. J. García de Abajo, *Probing bright and dark surface-plasmon modes in individual and coupled noble metal nanoparticles using an electron beam*, Nano Lett. **9**, 399–404 (2009). (see p. 28)

[73] A. L. Koh, K. Bao, I. Khan, W. E. Smith, G. Kothleitner, P. Nordlander, S. A. Maier, and D. W. McComb, *Electron energy-loss spectroscopy (EELS) of surface plasmons in single silver nanoparticles and dimers: Influence of beam damage and mapping of dark modes*, ACS Nano **3**, 3015–3022 (2009). (see p. 28)

[74] U. Hohenester and A. Trügler, *MNPBEM - a Matlab toolbox for the simulation of plasmonic nanoparticles*, Comput. Phys. Commun. **183**, 370 (2012). (see p. 28)

[75] F.-P. Schmidt, H. Ditlbacher, U. Hohenester, A. Hohenau, F. Hofer, and J. R. Krenn, *Dark plasmonic breathing modes in silver nanodisks*, Nano Lett. **11**, 5780–5783 (2012). (see p. 28)

[76] P. D. Nellist and S. J. Pennycook, *Subangstrom resolution by under focused incoherent transmission electron microscopy*, Phys. Rev. Lett. **81**, 4156–4159 (1998). (see pp. 28 and 92)

[77] M. Born and E. Wolf, *Principles of Optics: Electromagnetic Theory of Propagation, Interference and Diffraction of Light*, Cambridge University Press, Cambridge (1999). (see p. 28)

[78] David Rossouw and Gianluigi A. Botton, *Plasmonic response of bent silver nanowires for nanophotonic subwavelength waveguiding*, Phys. Rev. Lett. **110**, 066801 (2013). (see pp. 28 and 92)

[79] P. E. Batson, *Simultaneous STEM imaging and electron-energy-loss spectroscopy with atomic-column sensitivity*, Nature **366**, 727–728 (1993). (see p. 28)

[80] N. D. Browning, M. F. Chisholm, and S. J. Pennycook, *Atomic-resolution chemical analysis using a scanning transmission electron microscope*, Nature **366**, 143–146 (1993). (see p. 28)

[81] M. Bosman, V. J. Keast, J. L. Garcia-Munoz, A. J. D' Alfonso, S. D. Findlay, and L. J. Allen, *Two-dimensional mapping of chemical information at atomic resolution*, Phys. Rev. Lett. **99**, 086102 (2007). (see p. 28)

[82] P. A. Cherenkov, *The visible glow of pure liquids under the action of γ-rays*, Dokl. Akad. Nauk SSSR **2**, 451–454 (1934). (see p. 30)

[83] V. L. Ginzburg and I. M. Frank, *Radiation of a uniformly moving electron due to its transition from one medium to another*, Zh. Eksp. Theor. Fiz. [Sov. Phys. JETP] **16**, 15–28 (1946). (see p. 30)

[84] P. Goldsmith and J. V. Jelley, *Optical transition radiation from protons entering metal surfaces*, Philos. Mag. **4**, 836–844 (1959). (see p. 30)

[85] A. P. Potylitsyn, *Transition radiation and diffraction radiation. Similarities and differences*, Nucl. Instrum. Methods Phys. Res. B **145**, 169–179 (1998). (see p. 30)

[86] S. J. Smith and E. M. Purcell, *Visible light from localized surface charges moving across a grating*, Phys. Rev. **92**, 1069 (1953). (see p. 30)

[87] W. W. Salisbury, *Generation of light from free electrons*, J. Opt. Soc. Am. **60**, 1279–1284 (1970). (see p. 30)

[88] D. Heitmann, *Radiative decay of surface plasmons excited by fast electrons on periodically modulated silver plasmons*, J. Phys. C **10**, 397–405 (1977). (see p. 30)

[89] M. V. Bashevoy, F. Jonsson, A. V. Krasavin, N. I. Zheludev, Y. Chen, and M. I. Stockman, *Generation of traveling surface plasmon waves by free-electron impact*, Nano Lett. **6**, 1113–1115 (2006). (see p. 30)

[90] J. T. van Wijngaarden, E. Verhagen, A. Polman, C. E. Ross, H. J. Lezec, and H. A. Atwater, *Direct imaging of propagation and damping of near-resonance surface plasmon polaritons using cathodoluminescence spectroscopy*, Appl. Phys. Lett. **88**, 221111 (2006). (see p. 30)

[91] N. Yamamoto, K. Araya, and F. J. García de Abajo, *Photon emission from silver particles induced by a high-energy electron beam*, Phys. Rev. B **64**, 205419 (2001). (see p. 30)

[92] E. J. R. Vesseur, R. de Waele, M. Kuttge, and A. Polman, *Direct observation of plasmonic modes in Au nanowires using high-resolution cathodoluminescence spectroscopy*, Nano Lett. **7**, 2843–2846 (2007). (see p. 30)

[93] C. E. Hofmann, E. J. R. Vesseur, L. A. Sweatlock, H. J. Lezec, F. J. García de Abajo, A. Polman, and H. A. Atwater, *Plasmon modes of annular nanoresonators imaged by spectrally resolved cathodoluminescence*, Nano Lett. **7**, 3612–3617 (2007). (see p. 30)

[94] H. Boersch, J. Geiger, and W. Stickel, *Interaction of 25-kev electrons with lattice vibrations in lif. experimental evidence for surface modes of lattice vibration*, Phys. Rev. Lett. **17**, 379–381 (1966). (see p. 30)

[95] R. Egoavil, N. Gauquelin, G. T. Martinez, S. Van Aert, G. Van Tendeloo, and J. Verbeeck, *Atomic resolution mapping of phonon excitations in STEM-EELS experiments*, arXiv:1403.1849v1. (2014). (see p. 30)

[96] J. Schilling and H. Raether, *Energy gain of fast electrons interacting with surface plasmons*, J. Phys. Condens. Matter **6**, L358–L360 (1973). (see p. 30)

[97] B. Barwick, D. J. Flannigan, and A. H. Zewail, *Photon induced near-field electron microscopy*, Nature **462**, 902–906 (2009). (see pp. 32, 92, and 98)

[98] A. Yurtsever, J. S. Baskin, and A. H. Zewail, *Entangled nanoparticles: Discovery by visualization in 4D electron microscopy*, Nano Lett. **12**, 5027–5032 (2012). (see p. 32)

[99] A. Yurtsever, R. M. van der Veen, and A. H. Zewail, *Subparticle ultrafast spectrum imaging in 4D electron microscopy*, Science **335**, 59–64 (2012). (see pp. 32 and 92)

[100] D. G. Grier, *A revolution in optical manipulation*, Nature **424**, 810–816 (2003). (see p. 34)

[101] S. Groeblacher, J. B. Hertzberg, M. R. Vanner, G. D. Cole, S. Gigan, K. C. Schwab, and M. Aspelmeyer, *Demonstration of an ultracold micro-optomechanical oscillator in a cryogenic cavity*, Nat. Phys. **5**, 485–488 (2009). (see p. 34)

[102] P. J. Allen, *A radiation torque experiment*, AJP **34**, 1185–1192 (1966). (see pp. 34 and 48)

[103] M. E. J. Friese, T. A. Nieminen, N. R. Heckenberg, and H. Rubinsztein-Dunlop, *Optical alignment and spinning of laser-trapped microscopic particles*, Nature **394**, 348–350 (1998). (see p. 34)

[104] M. Liu, T. Zentgraf, Y. Liu, G. Bartal, and X. Zhang, *Light-driven nanoscale plasmonic motors*, Nat. Nanotech. **5**, 570–573 (2010). (see p. 34)

[105] B. E. Kane, *Levitated spinning graphene flakes in an electric quadrupole ion trap*, Phys. Rev. B **82**, 115441 (2010). (see p. 34)

[106] K. T. Gahagan and G. A. Swartzlander, *Trapping of low-index microparticles in an optical vortex*, J. Opt. Soc. Am. B **15**, 524–534 (1998). (see p. 34)

[107] P. Galajda and P. Ormos, *Complex micromachines produced and driven by light*, Appl. Phys. Lett. **78**, 249–251 (2001). (see p. 34)

[108] L. Tong, V. D. Miljković, and Mikael Käll, *Alignment, rotation, and spinning of single plasmonic nanoparticles and nanowires using polarization dependent optical forces*, Nano Lett. **10**, 268–273 (2010). (see p. 34)

[109] Y. Arita, M. Mazilu, and K. Dholakia, *Laser-induced rotation and cooling of a trapped microgyroscope in vacuum*, Nat. Commun. **4**, 2374 (2012). (see p. 34)

[110] I. Bialynicki-Birula and Z. Bialynicka-Birula, *Rotational frequency shift*, Phys. Rev. Lett. **78**, 2539–2542 (1997). (see pp. 34 and 41)

[111] J. Courtial, D. A. Robertson, K. Dholakia, L. Allen, and M. J. Padgett, *Rotational frequency shift of a light beam*, Phys. Rev. Lett. **81**, 4828–4830 (1998). (see p. 34)

[112] J. Courtial, K. Dholakia, D. A. Robertson, L. Allen, and M. J. Padgett, *Measurement of the rotational frequency shift imparted to a rotating light beam possessing orbital angular momentum*, Phys. Rev. Lett. **80**, 3217–3219 (1998). (see p. 34)

[113] M. Michalski, W. Hüttner, and H. Schimming, *Experimental demonstration of the rotational frequency shift in a molecular system*, Phys. Rev. Lett. **95**, 203005 (2005). (see pp. 34 and 41)

[114] A. Ashkin and J. M. Dziedzic, *Optical levitation in high vacuum*, Appl. Phys. Lett. **28**, 333–335 (1976). (see p. 34)

[115] L. D. Landau and E. M. Lifshitz, *The classical theory of fields*, Pergamon Press, Oxford (1981). (see p. 36)

[116] F. S. Chute, *The reaction torque on an axial multipole radiator*, IEEE Trans. Antennas Propag. **15**, 585–587 (1967). (see p. 37)

[117] G. W. Ford and W. H. Weber, *Electromagnetic interactions of molecules with metal surfaces*, Phys. Rep. **113**, 195–287 (1984). (see p. 43)

[118] Y. B. Zel'dovich, *Generation of waves by a rotating body*, Sov. Phys. JETP **35**, 1085 (1971). (see p. 44)

[119] J. D. Bekenstein and M. Schiffer, *The many faces of superradiance*, Phys. Rev. D **58**, 064014 (1998). (see p. 44)

[120] A. A. Starobinskii, *Amplification of waves during reflection from a rotating black hole*, Sov. Phys. JETP **37**, 28–32 (1973). (see p. 44)

[121] S. W. Hawking, *Particle creation by black holes*, Commun. math. Phys. **43**, 199–220 (1974). (see p. 44)

[122] A. Manjavacas and F. J. García de Abajo, *Vacuum friction in rotating particles*, Phys. Rev. Lett. **105**, 113601 (2010). (see pp. 44, 46, and 47)

[123] A. Manjavacas and F. J. García de Abajo, *Thermal and vacuum friction acting on rotating particles*, Phys. Rev. A **82**, 063827 (2010). (see p. 44)

[124] J. Lipfert, J. W. J. Kerssemakers, T. Jager, and N. H. Dekker, *Magnetic torque tweezers: measuring torsional stiffness in DNA and rec A-DNA filaments*, Nat. Methods **7**, 977–980 (2010). (see p. 45)

[125] T. Ito, H. Ando, T. Suzuki, T. Ogura, K. Hotta, Y. Imamura, Y. Yamaguchi, and H. Handa, *Identification of a primary target of thalidomide teratogenicity*, Science **327**, 1345–1350 (2010). (see p. 52)

[126] C. Noguez and I. L. Garzon, *Optically active metal nanoparticles*, Chem. Soc. Rev. **38**, 757—771 (2009). (see p. 52)

[127] Y. Xia, Y. Zhou, and Z. Tang, *Chiral inorganic nanoparticles: origin, optical properties and bioapplications*, Nanoscale **3**, 1374–1382 (2011). (see p. 52)

[128] E. Hendry, T. Carpi, J. Johnston, M. Popland, R. V. Mikhaylovskiy, A. J. Lapthorn, S. M. Kelly, L. D. Barron, N. Gadegaard, and M. Kadodwala, *Ultrasensitive detection and characterization of biomolecules using superchiral fields*, Nat. Nanotech. **5**, 783–787 (2010). (see p. 52)

[129] J. K. Gansel, M. Thiel, M. S. Rill, M. Decker, K. Bade, V. Saile, G. von Freymann, S. Linden, and M. Wegener, *Gold helix photonic metamaterial as broadband circular polarizer*, Science **325**, 1513–1515 (2009). (see pp. 52 and 71)

[130] A. V. Rogacheva, V. A. Fedotov, A. S. Schwanecke, and N. I. Zheludev, *Giant gyrotropy due to electromagnetic-field coupling in a bilayered chiral structure*, Phys. Rev. Lett. **97**, 177401 (2006). (see p. 52)

[131] N. Liu, H. Liu, S. N. Zhu, and H. Giessen, *Stereometamaterials*, Nat. Photon. **3**, 157–162 (2009). (see p. 52)

[132] M. Hentschel, M. Schaeferling, T. Weiss, N. Liu, and H. Giessen, *Three-dimensional chiral plasmonic oligomers*, Nano Lett. **12**, 2542–2547 (2012). (see pp. 52 and 60)

[133] A. Guerrero-Martinez, B. Auguie, J. L. Alonso Gomez, Z. Dzolic, S. Gomez Grana, M. Zinic, M. M. Cid, and L. M. Liz-Marzán, *Intense optical activity from three-dimensional chiral ordering of plasmonic nanoantennas*, Angew. Chem. **50**, 5499 (2011). (see p. 52)

[134] C.-L. Chen, P. Zhang, and N. L. Rosi, *A new peptide-based method for the design and synthesis of nanoparticle superstructures: Construction of highly ordered gold nanoparticle double helices*, J. Am. Chem. Soc. **130**, 1355–13577 (2008). (see p. 52)

[135] J. Sharma, R. Chhabra, A. Cheng, J. Brownell, Y. Liu, and H. Yan, *Control of self-assembly of DNA tubules through integration of gold nanoparticles*, Science **323**, 112–116 (2009). (see p. 52)

[136] A. J. Mastroianni, S. A. Claridge, and A. P. Alivisatos, *Pyramidal and chiral groupings of gold nanocrystals assembled using DNA scaffolds*, J. Am. Chem. Soc. **131**, 8455 (2009). (see p. 52)

[137] N. C. Seeman, *DNA in a material world*, Nature **421**, 427 (2003). (see p. 52)

[138] P. W. K. Rothemund, *Folding DNA to create nanoscale shapes and patterns*, Nature **440**, 297–302 (2006). (see p. 52)

[139] M. S. Douglas, H. Dietz, T. Liedl, B. Hogberg, F. Graf, and W. M. Shih, *Self-assembly of DNA into nanoscale three-dimensional shapes*, Nature **459**, 414–418 (2009). (see p. 52)

[140] D. Han, S. Pal, J. Nangreave, Z. Deng, Y. Liu, and H. Yan, *DNA origami with complex curvatures in three-dimensional space*, Science **332**, 342–346 (2011). (see p. 52)

[141] A. V. Pinheiro, D. Han, W. M. Shih, and H. Yan, *Challenges and opportunities for structural DNA nanotechnology*, Nat. Nano. **6**, 763–772 (2011). (see p. 52)

[142] F. J. García de Abajo, *Interaction of radiation and fast electrons with clusters of dielectrics: A multiple scattering approach*, Phys. Rev. Lett. **82**, 2776–2779 (1999). (see p. 58)

[143] F. J. García de Abajo, *Multiple scattering of radiation in clusters of dielectrics*, Phys. Rev. B **60**, 6086–6102 (1999). (see pp. 58, 71, and 97)

[144] S. A. Maier, P. G. Kik, and H. A. Atwater, *Optical pulse propagation in metal nanoparticle chain waveguides*, Phys. Rev. B **67**, 205402 (2003). (see p. 58)

[145] W. H. Weber and G. W. Ford, *Propagation of optical excitations by dipolar interactions in metal nanoparticle chains*, Phys. Rev. B **70**, 125429 (2004). (see p. 58)

[146] A. O. Govorov, Z. Fan, P. Hernandez, J. M. Slocik, and R. R. Naik, *Theory of circular dichroism of nanomaterials comprising chiral molecules and nanocrystals: Plasmon enhancement, dipole interactions, and dielectric effects*, Nano Lett. **10**, 1374–1384 (2010). (see pp. 60, 61, and 123)

[147] Z. Fan and A. O. Govorov, *Chiral nanocrystals: Plasmonic spectra and circular dichroism*, Nano Lett. **12**, 3283–3289 (2012). (see pp. 60 and 62)

[148] I. Lieberman, G. Shemer, T. Fried, E. M. Kosower, and G. Markovich, *Plasmon-resonance-enhanced absorption and circular dichroism*, Angew. Chem. Int. Ed. **47**, 4855–4857 (2008). (see p. 61)

[149] J. M. Slocik, A. O. Govorov, and R. R. Naik, *Plasmonic circular dichroism of peptide-functionalized gold nanoparticles*, Nano Lett. **11**, 701—705 (2011). (see p. 61)

[150] X. Shen, P. Zhan, A. Kuzyk, Q. Liu, A. Asenjo-Garcia, H. Zhang, F. J. García de Abajo, A. Govorov, B. Ding, and N. Liu, *3D plasmonic chiral colloids*, Nanoscale **6**, 2077–2081 (2014). (see p. 64)

[151] R. Schreiber, N. Luong, Z. Fan, A. Kuzyk, P. Nickels, D. M. Smith, B. Yurke, W. Kuang, A. O. Govorov, and T. Liedl, *Chiral plasmonic material with switchable circular dichroism*, Nat. Comm. **4**, 2948 (2013). (see p. 64)

[152] A. Kuzyk, R. Schreiber, H. Zhang, A. Govorov, T. Liedl, and N. Liu, *3D reconfigurable plasmonic metamolecules in the visible range*, Nat. Mat., in press (2014). (see p. 64)

[153] Y. Zhao, L. Xu, L. M. Liz-Marzán, H. Kuang, W. Ma, A. Asenjo-Garcia, F. J. García de Abajo, N. A. Kotov, L. Wang, and C. Xu, *Alternating plasmonic nanoparticle heterochains made by polymerase chain reaction and their optical properties*, J. Phys. Chem. Lett. **4**, 641–647 (2013). (see p. 64)

[154] R. Iinuma, Y. Ke, R. Jungmann, T. Schlichthaerle, J. B. Woehrstein, and P. Yin, *Polyhedra self-assembled from DNA tripods and characterized with 3D DNA-PAINT*, Science **344**, 65–69 (2014). (see p. 64)

[155] L. Carroll and J. Tenniel (illustrator), *Through the Looking-Glass, and What Alice Found There*, Macmillan, London (1871). (see p. 67)

[156] K. Y. Bliokh, Y. P. Bliokh, S. Savel'ev, and F. Nori, *Semiclassical dynamics of electron wave packet states with phase vortices*, Phys. Rev. Lett. **99**, 190404 (2007). (see p. 68)

[157] M. Uchida and A. Tonomura, *Generation of electron beams carrying orbital angular momentum*, Nature **464**, 737–739 (2010). (see p. 68)

[158] J. Verbeeck, H. Tian, and P. Schattschneider, *Production and application of electron vortex beams*, Nature **467**, 301–304 (2010). (see p. 68)

[159] B. J. McMorran, A. Agrawal, I. M. Anderson, A. A. Herzing, H. J. Lezec, J. J. McClelland, and J. Unguris, *Electron vortex beams with high quanta of orbital angular momentum*, Science **331**, 192 (2011). (see p. 68)

[160] K. Saitoh, Y. Hasegawa, K. Hirakawa, N. Tanaka, and M. Uchida, *Measuring the orbital angular momentum of electron vortex beams using a forked grating*, Phys. Rev. Lett. **111**, 074801 (2013). (see pp. 68 and 73)

[161] T. T. Wu and C. N. Yang, *Dirac monopoles without strings: monopole harmonics*, Nucl. Phys. B **107**, 365–380 (1976). (see p. 68)

[162] A. Béché, R. Van Boxem, G. Van Tendeloo, and J. Verbeeck, *Magnetic monopole field exposed by electrons*, Nat. Phys. **10**, 26–29 (2014). (see p. 68)

[163] S. Lloyd, M. Babiker, and J. Yuan, *Quantized orbital angular momentum transfer and magnetic dichroism in the interaction of electron vortices with matter*, Phys. Rev. Lett. **108**, 074802 (2012). (see p. 68)

[164] P. Schattschneider, S. Löffler, M. Stöger-Pollach, and J. Verbeeck, *Is magnetic chiral dichroism feasible with electron vortices?*, Ultramicroscopy **136**, 81–85 (2014). (see p. 68)

[165] J. Rusz and S. Bhowmick, *Boundaries for efficient use of electron vortex beams to measure magnetic properties*, Phys. Rev. Lett. **111**, 105504 (2013). (see p. 68)

[166] Z. Mohammadi, C. P. Van Vlack, S. Hughes, J. Bornemann, and R. Gordon, *Vortex electron energy loss spectroscopy for near-field mapping of magnetic plasmons*, Opt. Express **20**, 15024–15034 (2012). (see p. 68)

[167] C. Greenshields, R. L. Stamps, and S. Franke-Arnold, *Vacuum Faraday effect for electrons*, New J. Phys. **14**, 103040 (2012). (see p. 68)

[168] K. Y. Bliokh, P. Schattschneider, J. Verbeeck, and F. Nori, *Electron vortex beams in a magnetic field: a new twist on Landau levels and Aharonov-Bohm states*, PRX **2**, 041011 (2012). (see p. 68)

[169] G. Guzzinati, P. Schattschneider, K. Y. Bliokh, F. Nori, and J. Verbeeck, *Observation of the Larmor and Gouy rotations with electron vortex beams*, Phys. Rev. Lett. **110**, 093601 (2013). (see p. 68)

[170] J. Verbeeck, H. Tian, and G. Van Tendeloo, *How to manipulate nanoparticles with an electron beam?*, Adv. Mater. **25**, 1114–1117 (2013). (see p. 68)

[171] S. M. Lloyd, M. Babiker, and J. Yuan, *Mechanical properties of electron vortices*, Phys. Rev. A **88**, 031802 (2013). (see p. 68)

[172] D. L. Andrews, L. C. Dávila Romero, and M. Babiker, *On optical vortex interactions with chiral matter*, Opt. Commun. **237**, 133–139 (2004). (see p. 68)

[173] M. M. Coles and D. L. Andrews, *Chirality and angular momentum in optical radiation*, Phys. Rev. A **85**, 063810 (2012). (see p. 68)

[174] S. Lloyd, M. Babiker, and J. Yuan, *Interaction of electron vortices and optical vortices with matter and processes of orbital angular momentum exchange*, Phys. Rev. A **86**, 023816 (2012). (see p. 68)

[175] F. Araoka, T. Verbiest, and K. Clays, *Interactions of twisted light with chiral molecules: An experimental investigation*, Phys. Rev. A **71**, 055401 (2005). (see p. 68)

[176] W. Löffer, D. J. Broer, and J. P. Woerdman, *Circular dichroism of cholesteric polymers and the orbital angular momentum of light*, Phys. Rev. A **83**, 065801 (2011). (see p. 68)

[177] T. Yahn, J. S. Pierce, T. R. Harvey, and B. J. McMorran, *Addition, subtraction, and analysis of orbital angular momentum in electron vortex beams*, Microscopy and Microanalysis **19**, 1166–1167 (2013). (see p. 73)

[178] G. Guzzinati, L. Clark, A. Béché, and J. Verbeeck, *Measuring the orbital angular momentum of electron beams*, Phys. Rev. A **89**, 025803 (2014). (see p. 73)

[179] L. Clark, A. Béché, G. Guzzinati, and J. Verbeeck, *Quantitative measurement of orbital angular momentum in electron microscopy*, arXiv:1403.4398. (see p. 73)

[180] C. W. Bunn, *Chemical Christalography*, Oxford University Press, New York (1945). (see p. 76)

[181] R. Williams, *Optical rotatory effect in the nematic liquid phase of p-azoxyanisole*, Phys. Rev. Lett. **21**, 342–344 (1968). (see p. 76)

[182] E. Plum, X.-X. Liu, V. A. Fedotov, Y. Chen, D. P. Tsai, and N. I. Zheludev, *Metamaterials: optical activity without chirality*, Phys. Rev. Lett. **102**, 113902 (2009). (see p. 76)

[183] D. Rossouw, M. Couillard, J. Vickery, E. Kumacheva, and G. A. Botton, *Multipolar plasmonic resonances in silver nanowire antennas imaged with a subnanometer electron probe*, Nano Lett. **11**, 1499–1504 (2011). (see p. 84)

[184] I. Sersic, C. Tuambilangana, T. Kampfrath, and A. F. Koenderink, *Magnetoelectric point scattering theory for metamaterial scatterers*, Phys. Rev. B **83**, 245102 (2011). (see pp. 86 and 88)

[185] W. C. Johnson and I. Tinoco, *Circular dichroism of polypeptide solutions in the vacuum ultraviolet*, J. Am. Chem. Soc. **94**, 4389–4390 (1972). (see p. 89)

[186] W. W. Woody, *Circular dichroism and the conformational analysis of biomolecules*, Plenum, New York (1996). (see p. 89)

[187] P. D. Nellist, M. F. Chisholm, N. Dellby, O. L. Krivanek, M. F. Murfitt, Z. S. Szilagyi, A. R. Lupini, A. Borisevich, W. H. Sides Jr., and S. J. Pennycook, *Direct sub-angstrom imaging of a crystal lattice*, Science **305**, 1741 (2004). (see p. 92)

[188] W. Zhou, J. Lee, J. Nanda, S. T. Pantelides, S. J. Pennycook, and J. C. Idrobo, *Atomically localized plasmon enhancement in monolayer graphene*, Nat. Nanotech. **7**, 161–165 (2012). (see p. 92)

[189] R. F. Egerton, *Limits to the spatial, energy and momentum resolution of electron energy-loss spectroscopy*, Ultramicroscopy **107**, 575–586 (2007). (see p. 92)

[190] A. Howie, *Electrons and photons: exploiting the connection*, Inst. Phys. Conf. Ser. **161**, 311–314 (1999). (see p. 92)

[191] F. J. García de Abajo and M. Kociak, *Electron energy-gain spectroscopy*, New J. Phys. **10**, 073035 (2008). (see pp. 92 and 104)

[192] F. J. García de Abajo, A. Asenjo Garcia, and M. Kociak, *Multiphoton absorption and emission by interaction of swift electrons with evanescent light fields*, Nano Lett. **10**, 1859–1863 (2010). (see pp. 92, 93, and 98)

[193] S. T. Park, M. Lin, and A. H. Zewail, *Photon-induced near-field electron microscopy (PINEM): theoretical and experimental*, New J. Phys. **12**, 123028 (2010). (see pp. 92 and 98)

[194] A. Howie, *Photon interactions for electron microscopy applications*, Eur. Phys. J. Appl. Phys. **54**, 33502 (2011). (see p. 92)

[195] E. Ruska, *The development of the electron microscope and of electron microscopy*, Rev. Mod. Phys. **59**, 627–638 (1987). (see p. 93)

[196] B. A. Lippmann and J. Schwinger, *Variational principles for scattering processes. I*, Phys. Rev. **79**, 469–480 (1950). (see p. 94)

[197] J. J. Sakurai, *Modern Quantum Mechanics*, Addison-Wesley, (1994). (see p. 94)

[198] M. Quinten, *Optical properties of nanoparticle systems*, Wiley-VCH, Weinheim (2011). (see p. 97)

[199] B. J. Messinger, K. U. von Raben, R. K. Chang, and P. W. Barber, *Local fields at the surface of noble-metal microspheres*, Phys. Rev. B **24**, 649–657 (1981). (see p. 98)

[200] J. Zuloaga and P. Nordlander, *On the energy shift between near-field and far-field peak intensities in localized plasmon systems*, Nano Lett. **11**, 1280–1283 (2011). (see p. 98)

[201] P. Meystre and M. Sargent, *Elements of Quantum Optics*, Springer-Verlag, Berlin (2007). (see p. 102)

[202] J. Dalibard, Y. Castin, and K. Molmer, *Wave-function approach to dissipative processes in quantum optics*, Phys. Rev. Lett. **68**, 580–583 (1992). (see p. 102)

[203] R. Loudon, *The Quantum Theory of Light*, Oxford University Press, Oxford (2000). (see pp. 106 and 133)

[204] N. Talebi, W. Sigle, R. Vogelgesang, and P. van Aken, *Numerical simulations of interference effects in photon-assisted electron energy-loss spectroscopy*, New J. Phys. **15**, 053013 (2013). (see p. 107)

DOCTORAL THESIS IN PHYSICS
ICFO BARCELONA 2014

ICFO · THE INSTITUTE OF PHOTONIC SCIENCES
AV. CARL FRIEDRICH GAUSS, 3 · CASTELLDEFELS · BARCELONA
&
UCM · UNIVERSIDAD COMPLUTENSE DE MADRID
AV. COMPLUTENSE, S/N · CIUDAD UNIVERSITARIA · MADRID

ICFO
The Institute
of Photonic
Sciences